

Electronic Thesis and Dissertation Repository

8-22-2013 12:00 AM

Diffusionless Transition in Tricosane and Reversible Inhibition of Calcium Oxalate Monohydrate: Two Studies of Crystal Growth

Shailesh S. Nene, *The University of Western Ontario*

Supervisor: Prof. Jeffrey L. Hutter, *The University of Western Ontario*

A thesis submitted in partial fulfillment of the requirements for the Doctor of Philosophy degree in Physics

© Shailesh S. Nene 2013

Follow this and additional works at: <https://ir.lib.uwo.ca/etd>

 Part of the [Condensed Matter Physics Commons](#)

Recommended Citation

Nene, Shailesh S., "Diffusionless Transition in Tricosane and Reversible Inhibition of Calcium Oxalate Monohydrate: Two Studies of Crystal Growth" (2013). *Electronic Thesis and Dissertation Repository*. 1520.

<https://ir.lib.uwo.ca/etd/1520>

This Dissertation/Thesis is brought to you for free and open access by Scholarship@Western. It has been accepted for inclusion in Electronic Thesis and Dissertation Repository by an authorized administrator of Scholarship@Western. For more information, please contact wlsadmin@uwo.ca.

Diffusionless Transition in Tricosane and Reversible Inhibition of Calcium Oxalate Monohydrate: Two Studies of Crystal Growth

by
Shailesh Nene

Graduate Program in Physics

A thesis submitted in partial fulfillment
of the requirements for the degree of
Doctor of Philosophy

The School of Graduate and Postdoctoral Studies
The University of Western Ontario
London, Ontario, Canada

© Shailesh Nene 2013

Abstract

The process of crystal growth has been intensively studied, for both its academic interest and industrial importance. I report here two studies of crystal growth.

The normal alkanes are interesting, both in terms of their intrinsic properties and because many biological materials contain hydrocarbon domains. The normal alkanes often exhibit complicated phase behaviour, with phase diagrams containing multiple solid phases. We report here a curious pattern of twinned domains seen in one phase of tricosane ($C_{23}H_{48}$), which we have studied by X-ray diffraction, as well as by optical and atomic force microscopy. This pattern is seen in the rotator R_V phase, a monoclinic arrangement of tricosane molecules without orientational order. Transitions between this polymorph and the orthorhombic phase lying at higher temperatures preserve features at the molecular level, and thus represent a diffusionless, martensitic-like transformation.

Calcium oxalate monohydrate (COM) is the primary constituent of most kidney stones. Certain proteins, such as osteopontin (OPN), inhibit stone formation. The inhibition of crystallization due to adsorbed impurities is usually explained in terms of a model proposed in 1958 by Cabrera and Vermilyea, which hypothesizes that impurities adsorb to growth faces and pin growth steps, thus impeding their progress via the Gibbs-Thomson effect. To determine the role of OPN in the biomineralization of kidney stones, crystal growth on the {010} face of COM was examined in real time by atomic force microscopy in the presence of a synthetic peptide. We observed clear changes in the morphology of the growth-step structure and a decrease in step velocity upon addition of inhibitors, suggesting adsorption on the {010} growth hillocks. Experiments in which inhibitors were replaced in the growth cell by a supersaturated solution showed that COM hillocks are able to fully recover to their pre-inhibited state. Our results suggest that recovery occurs through incorporation of the peptide into the growing crystal, rather than by, e.g., desorption from the growth face. This work provides new insights into the mechanism by which crystal growth is inhibited, with important implications for the design of therapeutic agents for kidney stone disease and other forms of pathological calcification.

Keywords

diffusionless phase transition, crystallization, atomic force microscopy, calcium oxalate monohydrate, osteopontin, growth inhibition, reversible inhibition, kinetic inhibitor, kidney stones

Acknowledgments

Firstly, I would like to thank my supervisors, Dr. Jeffrey Hutter and Dr. Graeme Hunter, for their helpful guidance and expertise. For the triscoane project, I appreciate support and help for the XRD studies from Dr. Roberta Flemming from earth science department and Eric Karhu for letting me use one of his image for my thesis. For the calcium oxalate monohydrate project, I appreciate the support and assistance of my collaborators in Schulich School of Medicine and Dentistry, specifically Dr. Harvey Goldberg, Dr. Bernd Grohe for teaching me how to make growth solution, Yinyin Liao for teaching me the techniques needed to make the inhibitor solution.

I would like to thank to all my friends at Western who have supported me thought the course of this project.

Once again, I would like to extend my heartfelt gratitude to Dr. Hutter, who has helped from day one at this university. He guide me over the all stages of this project, including teaching me how to use the AFM, editing my writing, going over my presentations, and assisting in the data analysis. He has been a remarkable supervisor.

Finally I want to thank my family, specially my wife Nisha for every wonderful day she spends with me and makes it perfect!

Co-Authorship Statement.

Chapters 3 and 4 contain material from two published journal articles, while Chapter 5 is yet to be submitted:

S. Nene, E. Karhu, R. L. Flemming, and J. L. Hutter, "A diffusionless transition in a normal alkane," *Journal of Crystal Growth* **311** (23–24), 4770–4777 (2009).

Shailesh S. Nene, Graeme K. Hunter, Harvey A. Goldberg, and Jeffrey L. Hutter, "Reversible Inhibition of Calcium Oxalate Monohydrate Growth by an Osteopontin Phosphopeptide," *Langmuir* **29** (21), 6287–6295 (2013).

Shailesh S. Nene, Graeme Kenneth Hunter, Harvey A. Goldberg, and Jeffrey Lee Hutter, "Regrowth of calcium oxalate etch-pit on {100} faces," (in preparation).

Chapter 3 arose from an observation by Karhu during his MSc work, but not pursued at that time. Nene took over the project and prepared all the samples for this study. Nene, assisted by Hutter, performed optical and atomic force microscopy experiments. Nene, assisted by Flemming and Hutter, performed X-ray diffraction (XRD) experiments. Flemming and Hutter gave instruction and helped on data analysis for XRD experiments. Nene wrote the first draft, and Flemming and Hutter contributed to editing.

The work in Chapters 4 and 5 was initiated by Nene, and assisted by the Hunter & Goldberg lab. Nene prepared all samples for this study. Nene, assisted by Hutter, performed the optical and atomic force microscopy experiments, along with data analysis for this study. Nene wrote the first drafts of the manuscripts and Goldberg, Hunter, and Hutter contributed to editing.

CONTENTS

Abstract	ii
Acknowledgments	iii
Co-Authorship Statement	iv
List of Figures	viii
List of Tables	xi
List of Appendices.....	xii
List of Abbreviations.....	xiii
Chapter 1: Physics of Crystal Growth	1
1.1 Phase equilibrium	1
1.2 Ionic solutions	3
1.3 Nucleation	5
1.4 Growth of the crystal	7
1.5 Diffusionless Transitions.....	10
1.6 Theories for additives of crystal growth.....	11
1.7 Bibliography for Chapter 1.....	14
Chapter 2: Background	16
2.1 Alkanes	16
2.1.1 Basic concepts	16
2.1.2 Previous work.....	16
2.1.3 Study plan for solid-solid phase transitions in alkanes.....	19
2.2 Calcium oxalate	20
2.2.1 Biominerals.....	20

2.2.2 Calcium oxalate crystal structures	20
2.2.3 Previous work	22
2.2.4 Study plan for calcium oxalate crystallization	24
2.3 Atomic force microscopy	25
2.4 Bibliography for Chapter 2.....	26
Chapter 3: Diffusionless Transition in Tricosane	33
3.1 Introduction	33
3.2 Background	34
3.3 Experimental	35
3.4 Results & Discussion.....	37
3.4.1 Phase behavior	37
3.4.2 Domain Structure.....	40
3.4.3 Crystal Structure of the Monoclinic R _v Phase	44
3.4.4 Phase Transition Dynamics	46
3.4.5 Conceptual Model for the Twinned Phase	50
3.5 Conclusion.....	52
3.6 Bibliography for Chapter 3.....	58
Chapter 4: Reversible Inhibition of Calcium Oxalate Monohydrate Growth by an Osteopontin Phosphopeptide	61
4.1 Introduction	61
4.2 Materials and Methods	66
4.3 Results	71
4.4 Discussion	77
4.5 Conclusions	79
4.6 Bibliography for Chapter 4.....	80
Chapter 5: Regrowth of calcium oxalate etch-pit on {100} faces	84

5.1 Background	84
5.2 Method.....	86
5.2.1 Sample Preparation.....	86
5.2.2 Image Analysis	86
5.3 Measurements.....	89
5.4 Discussion	92
5.5 Summary	93
5.6 Bibliography for Chapter 5.....	94
Chaper 6: Conclusion	97
Appendix A: Twinning pattern in C_{25}	99
Appendix B: Detailed calculations for the conceptual model for crystal twinning	100
Curriculum Vitae.....	104

List of Figures

Figure 1.1 Phase coexistence curves for a pure material.....	1
Figure 1.2 (a) Gibbs free energy for a two phase system; at temperature T_c a phase transition occurs. (b) Entropy of the system as a function of temperature	2
Figure 1.3 Phase transition of a system as function of temperature.....	3
Figure 1.4 Critical radius in the nucleation process.	6
Figure 1.5 A schematic of a crystal growth surface.	7
Figure 1.6 Schematic for the advance of square spiral growth.	9
Figure 1.7 The growth of a crystal due to step advancement.	10
Figure 1.8 Example of lattice deformation due to (a) a shear strain with a uniaxial dilatation, (b) simple shear, and (c) a combination of uniaxial dilation and shear	11
Figure 1.9 Plots of the expected dependence of step speeds on concentration resulting from two models of impurity interaction: step pinning (left); incorporation (right).	12
Figure 1.10 Effect of impurity atoms adsorbed to growth surfaces on step advance.....	13
Figure 2.1 Phase diagram for binary system of C_{23} - C_{25} proposed by F. Rajabalee's group	18
Figure 2.2 Typical growth habit of a calcium oxalate monohydrate crystal with faces and crystallographic directions indicated.....	22
Figure 2.3 A schematic of the parts of an atomic force microscope	26
Figure 3.1 Optical micrograph of a pattern of stripes in C_{23} at a temperature of 315.6 K.	34
Figure 3.2 X-ray diffraction patterns for the five polymorphs of tricosane observed, with principal peaks labeled according to their Miller indices.	38
Figure 3.3 AFM study of the twinning pattern observed for C_{23} in the RV phase at 41 °C.	42
Figure 3.4 2D X-ray diffraction result in twinned phase (a) Peaks observed on area detector.	43
Figure 3.5 Sequence of optical microscopy images of a single region of a tricosane sample as the temperature is varied.	48

Figure 3.6 AFM tapping mode images during transition from R_V – R_I phase..	49
Figure 3.7 Illustration showing a cross-section of a twinned region perpendicular to the ridges..	51
Figure 3.8 Principal Bragg peaks observed for the O_i orthorhombic phase at 34 °C	53
Figure 3.9 Principal Bragg peaks observed for the orthorhombic phase at 38 °C	54
Figure 3.10 Principal Bragg peaks observed for the monoclinic rotator phase at 41 °C	55
Figure 3.11 Principal Bragg peaks observed for the orthorhombic rotator phase at 43 °C.....	56
Figure 3.12 Principal Bragg peaks observed for the hexagonal rotator phase at 46 °C.....	57
Figure 4.1 Cabrera and Vermilyea’s step-pinning model.	62
Figure 4.2 Schematic of a typical COM crystal	65
Figure 4.3 Step speed as a function of time during a typical experiment.	69
Figure 4.4 Series of AFM images acquired 50.2 s apart of a growth hillock on a (010) COM surface showing the advance of growth steps.....	70
Figure 4.5 Step speeds on (010) COM faces as a function of supersaturation. Extrapolation to zero step speed suggests a saturation limit of approximately 0.15 mM.	71
Figure 4.6 Series of AFM images showing the effect of the addition of 0.1 $\mu\text{g/mL}$ pOPAR on COM... 72	72
Figure 4.7 Step speed in the $\langle 021 \rangle$ direction as a function of time demonstrating the inhibition of growth steps by a concentration of 0.075 $\mu\text{g/mL}$ pOPAR for COM	73
Figure 4.8 Speed of COM steps in the $\langle 021 \rangle$ directions as a function of supersaturation in the presence of varying levels of pOPAR.	74
Figure 4.9 Series of AFM images acquired during growth/inhibition/recovery cycling of COM.....	76
Figure 4.10 Step velocity as a function of time during growth-inhibition-recovery cycling of COM....	77
Figure 5.1 AFM deflection image ($2\ \mu\text{m} \times 2\ \mu\text{m}$) of etch pits on a COM (100) surface.....	85
Figure 5.2 Sequence of AFM deflection images ($2\ \mu\text{m} \times 2\ \mu\text{m}$) showing etch-pit regrowth of a (100) COM surface in the presence of 0.235 mM CaOx.	87
Figure 5.3 Steps in measuring dimensions of etch pits.	88
Figure 5.4 Change in pit area as function of time for etch-pit regrowth in the presence of 10 $\mu\text{g/ml}$ of pOPAR at 0.235 mM CaOx concentration.....	89

Figure 5.5 Etch-pit filling schematic with (a) indicating the apparent growth Δx and (b) showing a cross-sectional view of a re-growing pit. 90

Figure 5.6 Etch pit regrowth rate as a function of time for growth in the presence of 10 $\mu\text{g/mL}$ of pOPAR at a growth concentration of 0.235mM of CaOx. 91

Figure A.1 Optical microcopy images showing the twinning pattern observed in n-pentacosane. 99

Figure B.1 Illustration showing a cross-section of a twinned region perpendicular to the ridges. 100

Figure B.2 Illustration showing formation of the single domain of twinned region in C23. 101

List of Tables

Table I Different phase sequences for tricosane proposed in the literature.	17
Table II Phase behavior of tricosane. The precision of our observed transition temperature is approximately ± 0.2 K.	35
Table III Principal Bragg peaks observed for the Oi orthorhombic phase at 34 °C.	53
Table IV Principal Bragg peaks observed for the Odc1 orthorhombic phase at 38 °C.	54
Table V Principal Bragg peaks observed for the monoclinic rotator phase at 41 °C.	55
Table VI Principal Bragg peaks observed for the orthorhombic rotator phase at 43 °C.	56
Table VII Principal Bragg peaks observed for the hexagonal rotator phase at 46 °C.	57
Table VIII Lattice parameters and properties for the five polymorphs of tricosane studied in this work (estimated standard deviations are indicated in parentheses).....	53
Table IX Pit filling rate for all the additives in this work	91

List of Appendices

Appendix A: Twinning pattern in C_{25}	99
Appendix B: Detailed calculations for the conceptual model for crystal twinning.....	100

List of Abbreviations

AFM	atomic force microscope
C ₂₃ H ₄₆	C23, tricosane
CaOx	calcium oxalate
COD	calcium oxalate dihydrate
COM	calcium oxalate monohydrate
C-V model	Cabrera–Vermilyea model
HA	hydroxyapatite
KDP	potassium dihydrogen phosphate
MD	molecular dynamics
OPN	osteopontin
OPN 220-235	peptide of OPN containing residues 220–235
P0	OPN 220–235 with no phosphate
P1	OPN 220–235 with one phosphate
P3	OPN 220–235 with three phosphates
poly-ASP	polyaspartate
pOPAR	peptide of OPN containing residues 65–80
R_i	Rotator- <i>i</i> phase
SEM	scanning electron microscopy

Chapter 1: Physics of Crystal Growth

1.1 Phase equilibrium

A material is said to be in a well-defined phase if all of its physical properties are spatially homogenous. Well-known phases are the solid, liquid and vapor states of matter. A material may exist in more than one phase at the same time. An ice-water system is a familiar example of a two-phase system in which both phases coexist at a single temperature and pressure, each with its own molar volume (ice is less dense than water) and entropy (water vapor is less ordered than ice).

If the phase coexistence temperature is known as a function of pressure, one can construct a phase diagram to illustrate the conditions at which thermodynamically different phases can occur in equilibrium. Fig. 1.1 shows a typical phase diagram, in which the phase coexistence curves (dashed lines) show the regions where the two phases coexist¹. The coexistence curves thus bound regions in which only a single phase can exist in equilibrium.

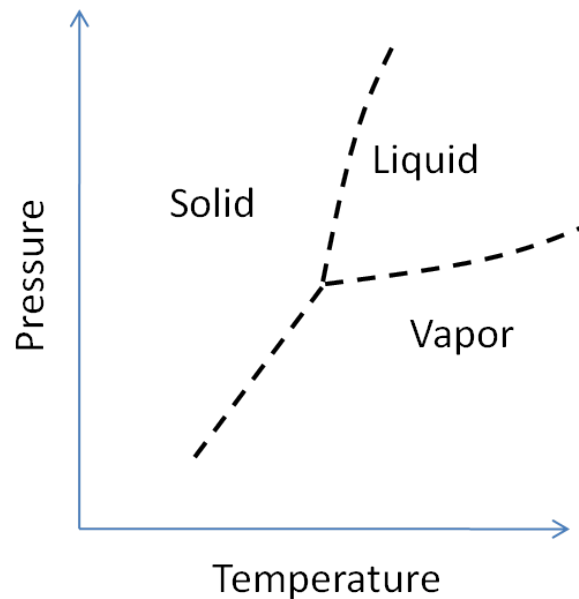


Figure 1.1 Phase coexistence curves for a pure material.

A phase can exist for a wide range of temperature and composition. The relative stability of a phase at constant temperature and pressure is determined by Gibbs free energy $G = U + pV - TS = H - TS$. Here, H is enthalpy, which depends on internal energy U , p is the ambient pressure, V is the volume of the system, T is absolute temperature and S is the entropy, which is measured in units of energy per degree Kelvin².

A typical plot of Gibbs free energy as function of temperature, illustrated schematically in Fig. 1.2a for two phases at a constant pressure, shows a single temperature at which the phases coexist: where the two curves cross. At all other temperatures, the phase with the lowest free energy is observed in equilibrium.

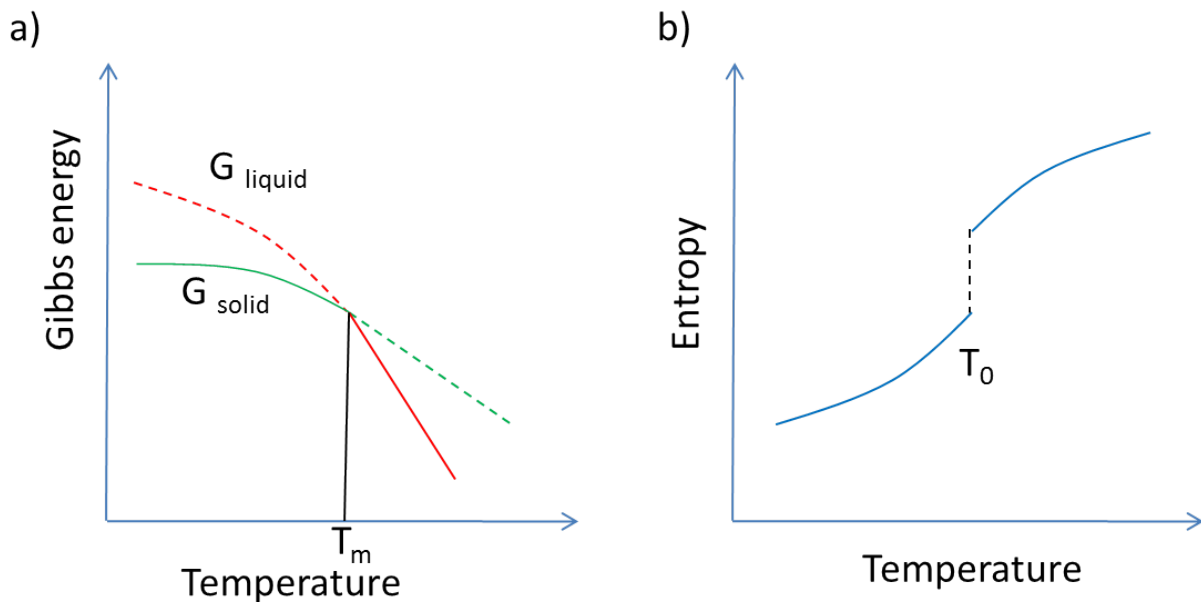


Figure 1.2 (a) Gibbs free energy for a two phase system; at temperature T_c a phase transition occurs. (b) Entropy of the system as a function of temperature.

Because the entropy of the equilibrium phase can be shown to be $S = -(\partial G/\partial T)_P$, a plot of entropy as a function of temperature (Fig. 1.2b) shows a discontinuous change in S at the phase coexistence temperature². Since the Gibbs free energies of the two phases are equal at this temperature, a

discontinuity in S requires a discontinuity in H : $\Delta H = T\Delta S$. Therefore, heat must be released or absorbed by the system when the phase boundary is crossed. This is known as the latent heat of transition.

Fig. 1.3 shows the typical behavior of a system when heat is added. In this example, when a heated solid reaches its melting temperature T_m , it begins to transform into a liquid. However, the two phases remain in equilibrium, and therefore at a constant temperature, until the entire solid is melted. The heat that must be supplied to the system, ΔH_m , is known as the latent heat of melting.

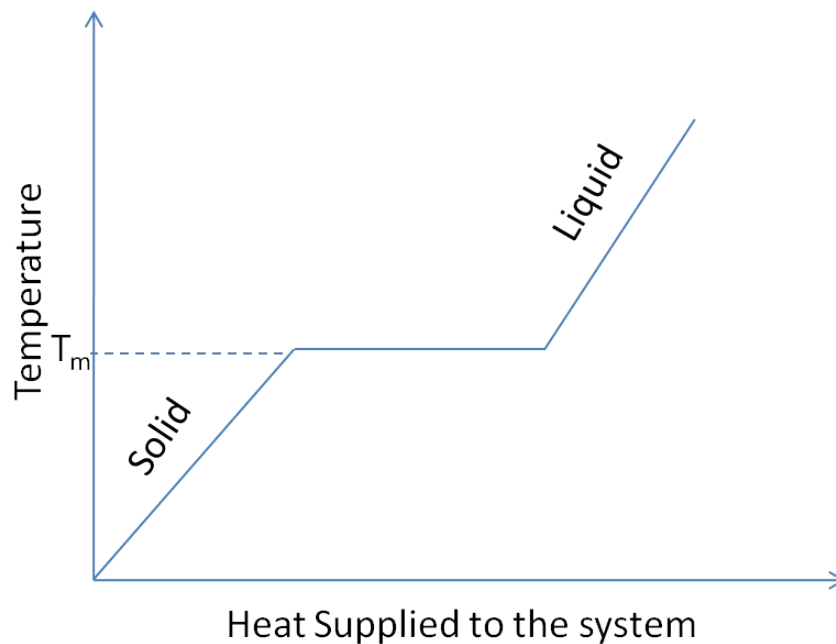


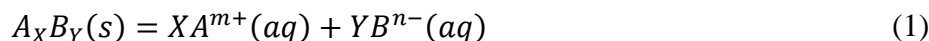
Figure 1.3 Phase transition of a system as function of temperature.

1.2 Ionic solutions

Some materials, when dissolved in water or another solvent, will dissociate into ions and are therefore able to transport an electric current. These solutions are commonly known as electrolytes. The degree to which dissociation occurs is again governed by the Gibbs free energy. Typically, there is a maximum concentration of solute that can be dissolved, above which the solvated material coexists with undissolved solid. A solution containing the maximum equilibrium concentration of solute is referred to

as saturated; one that contains more solute material than can be dissolved under normal circumstances is referred to as supersaturated.

Consider the dissolution reaction



in which the ionic solid $A_X B_Y$ dissolves into its component ions in water. The degree to which the compound dissociates is characterized by the solubility product constant K_{sp} ³. Substances with a smaller solubility product will have lower solubility. The saturation concentrations are determined by K_{sp} through the relation

$$K_{sp} = [A^{m+}]^X [B^{n-}]^Y \quad (2)$$

where $[A^{m+}]$ and $[B^{n-}]$ are the concentrations of the ions, each raised to a power equal to its coefficient X and Y , respectively, in the balanced equation 1.

In an ionic solution, ions are randomly distributed. However, although the solution is electrically neutral, Coulomb attraction results in an increased concentration of ions with opposite charge near each ion. The resulting damping in the net electric field due to mobile charge carriers is known as electric field screening. Because of this interaction in the solution, it is not possible to consider every ion separately for all the equilibrium conditions. To consider the effect of interactions between ions in a concentrated electrolytic solution, we replace the concentration of each species in Eq. 2 with an effective value, known as its activity. The activity is proportional to the molar concentration of the ionic species in solution as described by

$$a_i = \gamma_i c_i \quad (3)$$

where γ_i is the activity coefficient of ion i and c_i is the molar concentration ion species i .

The activity coefficient of a particular ion in a solution can be estimated by

$$\log \gamma = -A z_i^2 I^{1/2} \quad (4)$$

where I is the ionic strength and A is the Debye-Hückel constant⁴ (for aqueous solution at 25 °C $A = 0.51 \text{ mol}^{-1/2} \text{ dm}^{3/2}$). Ionic strength is a measure of the concentration of ions in solution and is defined as

$$I = \frac{1}{2} \sum c_i z_i^2 \quad (5)$$

where z_i is the charge number of ion species i , and the sum is taken over all ions present in the solution. In practice it is not possible to measure the activity coefficient of a particular ion in solution because the solution must contain both positively and negatively charged ions. The mean activity coefficient is introduced using the equation

$$\log \gamma = -A |z_+ z_-| I^{1/2} \quad (6)$$

where z_+ and z_- are the number of ions produced by the electrolyte. This is the Debye-Huckel limiting law, which works well for a dilute solution of the electrolyte.

1.3 Nucleation

When a molten material is cooled below its melting point, or a solution brought above its saturation limit, the formation of a solid phase is thermodynamically favoured. In most cases, creation of a solid takes place through a process known as nucleation. Nucleation is classified into two types: homogenous and heterogeneous. Homogeneous nucleation is the formation of a nucleus without preferential nucleation sites. The case in which nuclei are formed at sites such as a substrate, the surface of the container, or impurity particles is referred to as heterogeneous nucleation.

In order for a nucleus to form from a supersaturated solution, it must overcome a certain energy barrier known as the activation energy or free energy of formation ΔG . The formation of a nucleus of the new phase in the homogenous existing phase produces an interface between the phases. The resulting free energy change can be considered to have two parts: the energy ΔG_S required for formation of a new surface and the volume free energy change ΔG_V associated with the phase transition. Thus,

$$\Delta G = \Delta G_S + \Delta G_V. \quad (7)$$

As an approximation, consider a spherical nucleus of radius r . In this case, Eq. 7 can be written as

$$\Delta G = 4\pi r^2 \sigma + \frac{4\pi}{3} r^3 \Delta G_V \quad (8)$$

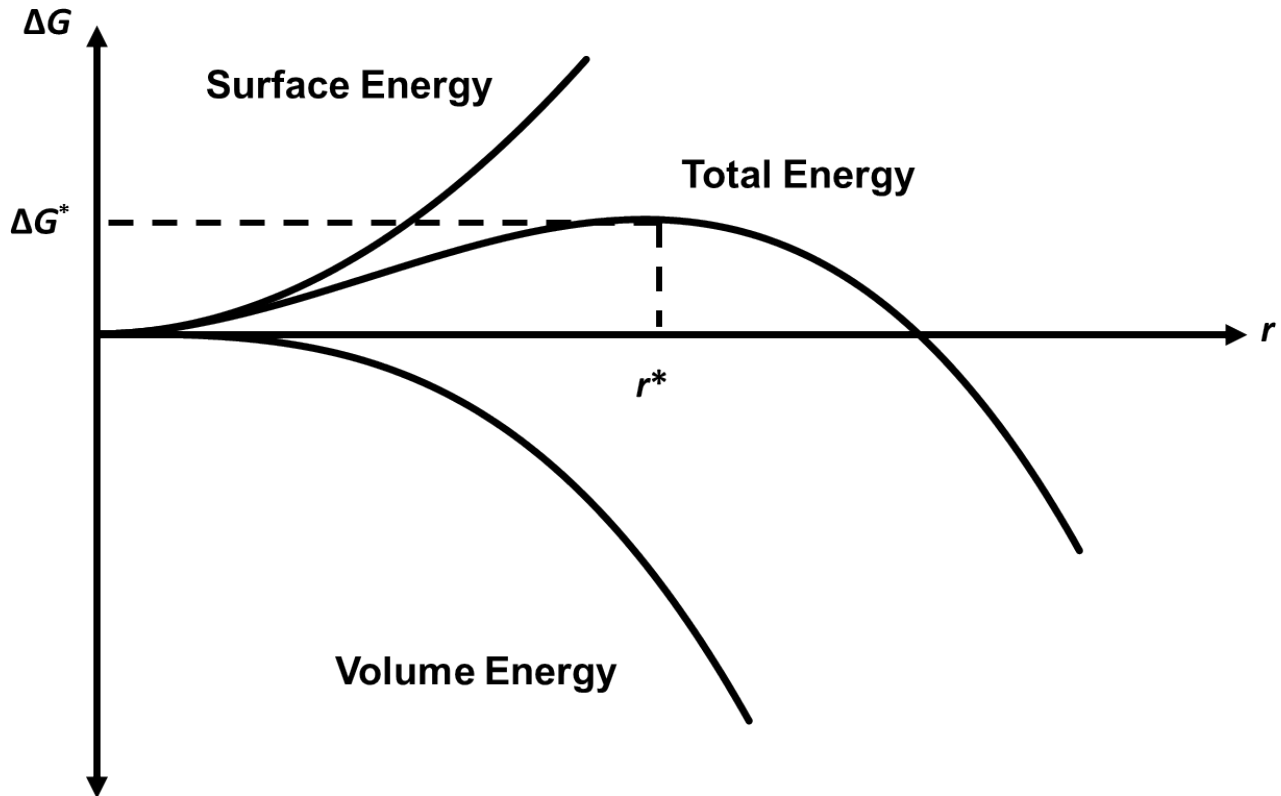


Figure 1.4 Critical radius in the nucleation process.

Here, $\Delta G_V < 0$ is the free energy change of the transformation per unit volume and σ is the interfacial tension. For small values of r , the surface term dominates and the total free energy remains positive. As r increases, ΔG_V becomes increasingly important, so that the free energy eventually decreases. As shown in Fig. 1.4, this results in a critical radius r^* , where the free energy is a maximum. Thus, continued growth is only favored for $r > r^*$. The value as critical radius r^* can be found by minimizing the free energy with respect to r :

$$\left. \frac{d\Delta G}{dr} \right|_{r=r^*} = 8\pi r^* \sigma + 4\pi r^{*2} \Delta G_V = 0. \quad (9)$$

Solving for r^* gives,

$$r^* = \frac{-2\sigma}{\Delta G_V}. \quad (10)$$

Particles smaller than r^* will dissociate in a supersaturated solution, while those larger will grow. Now if we assume that solution depletion due to nuclei formation can be neglected and the macroscopic surface free energy can be used to describe very small embryos as well, we can use the expression for r^* to calculate ΔG^* , the energy barrier to formation of critical nucleus, as

$$\Delta G^* = \frac{16\pi\sigma^3}{3(\Delta G_V)^2}. \quad (11)$$

1.4 Growth of the crystal

A crystal is a solid material in which atoms, ions or molecules are arranged in a periodic three-dimensional pattern. The spatial arrangement can be described in terms of fundamental building blocks called unit cells, which reflect the fundamental symmetry of the crystal. A faceted crystal is one in which the crystal is terminated by a set of low-index planes. In this case, growth generally proceeds by the addition of individual units, termed “adatoms,” to the surface. The shape of the crystal surface plays a vital role in its growth. Fig. 1.5 defines elements of interest on a crystal face.

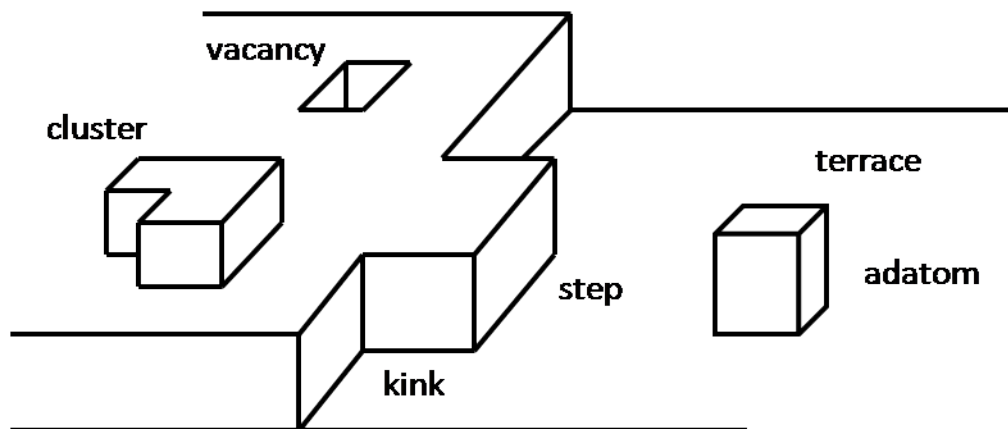


Figure 1.5 A schematic of a crystal growth surface (adapted from Ref. [2]).

In a supersaturated ionic solution, adatoms consist of ions. When an adatom adsorbs to the crystal surface, it is weakly bound and is free to diffuse on the surface. If the adatom reaches a step before desorbing from the surface, it is more strongly bound, and is less likely to desorb. An adatom bound to a step may diffuse along the step until it reaches a kink site, at which point it is considered to be part of the crystal.

A perfectly flat crystal will not have kink sites, so the adatom can only be weakly bound to the surface. For growth to proceed on crystals with flat surfaces, steps must be present. The two main sources of steps are surface (two-dimensional) nucleation and spiral growth around a screw dislocation. Dislocations are regions where the atoms are out of position in the crystal structure. A screw dislocation is a line defect in the crystal. Consider Fig. 1.6, which shows the advance of a square growth spiral resulting from a screw dislocation¹. Here, we begin with a square lattice with a screw dislocation perpendicular to the surface. A straight step originates from the dislocation, providing a preferred site for adatoms to bond. In a supersaturated state, adatoms will diffuse to the step, making it advance. If we assume a growth spiral with a square shape, this will create a new step at a 90° angle to the first. The new portion cannot advance until its length is greater than some critical length l^* . This results in a square spiral of steps with spacing $4l^*$ that terminates at the screw dislocation. Thus the growth spirals grows by motion of the steps across its surface.

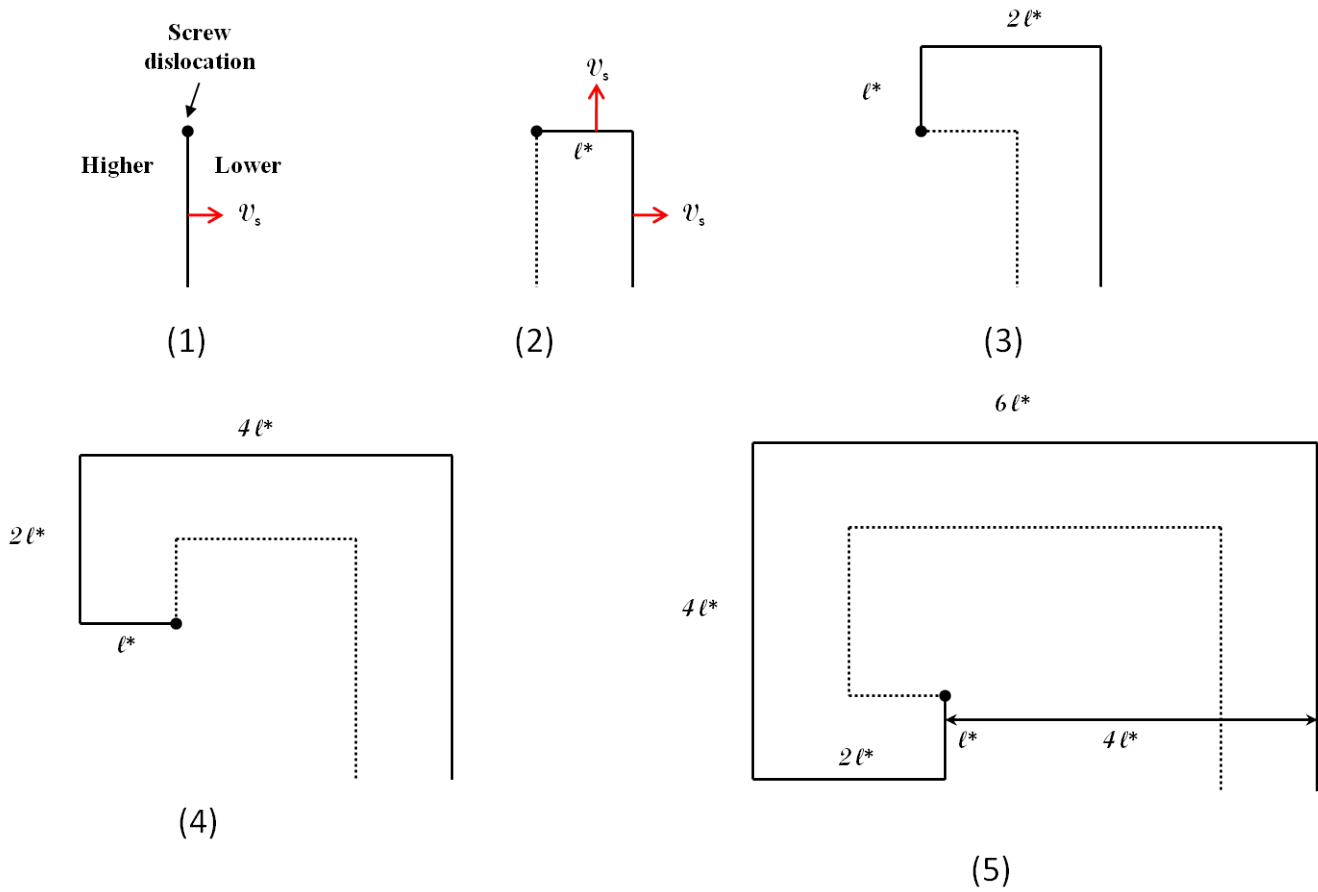


Figure 1.6 Schematic for the advance of square spiral growth.

If steps with height a and spacing d propagate velocity v_s , along a surface, the growth rate normal to the surface is

$$R = v_s \frac{a}{d} = v_s \frac{a}{4l^*}. \quad (12)$$

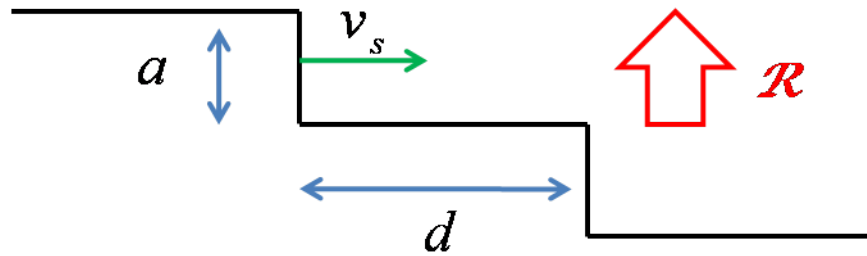


Figure 1.7 The growth of a crystal due to step advancement.

1.5 Diffusionless Transitions

In a phase transition, a solid, liquid or gaseous material undergoes a transition in which its physical properties change. For example, water turns into a vapour at its boiling point, changing its phase from liquid to gas. Typically, phase transitions result in long-range rearrangement and/or transport of the atoms/molecules.

Diffusionless transitions are a type of phase transition that occurs by *local* rearrangement of atoms. In these transitions, structural changes take place by the coordinated movement of atoms relative to their neighbors. The atoms' movements are small, typically less than interatomic distances, and the atoms preserve their relative positions with their neighboring atoms. Such an ordered movement of large numbers of atoms is referred to as a martensitic⁵ or military transformation. The most popular examples of this type of transition are Martensite transformations in steel. The name *Martensite* is after the German scientist Martens. Martensitic phase transitions have also been seen in shape memory alloys⁶. This type of alloy can be bent or stretched and will hold its deformed shape until heated above the transition temperature. Applying heat will cause it to return to its original shape. Shape memory alloys have applications in industries including medical (use of shape memory alloy wire in the robotic muscles) and aerospace (the shape memory wire is used to manipulate a flexible wing surface).

Spontaneous shear strain is an important characteristic of a martensite transition⁷. In these transitions there is definite orientational relationship between the parent and new martensite crystal structure. The shear strain is a homogenous distortion such that the displacement of each point is in same direction, with the magnitude of displacement proportional to the distance from a fixed plane of reference, which

is the invariant-plane which has not been affected by strain. Fig.1.8 (a) shows the case of shear strain with uniaxial dilatation, whereas Fig. 1.8 (b) shows a case of a simple shear along plane.

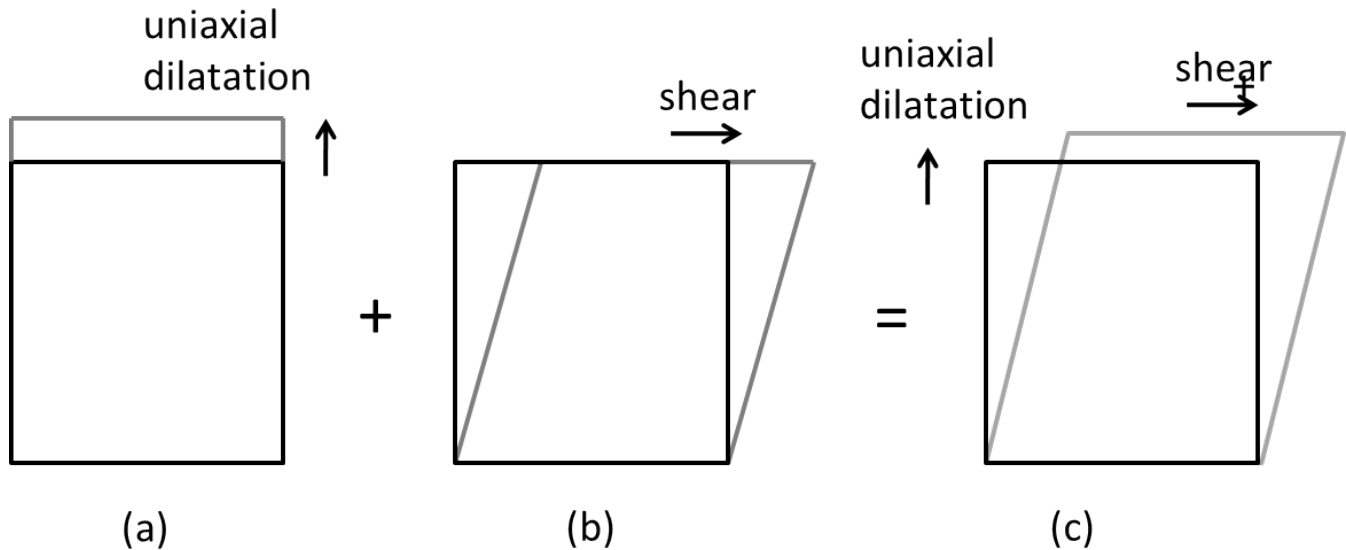


Figure 1.8 Example of lattice deformation due to (a) a shear strain with a uniaxial dilatation, (b) simple shear, and (c) a combination of uniaxial dilatation and shear

1.6 Theories for additives of crystal growth

Crystallization occurs at the surface, so anything that changes the constitution of the surface can have a significant effect on growth kinetics⁸. In equilibrium, the shape of a crystal is the one which minimizes the total surface free energy of the crystal⁹. The low energy faces are the slowest growing faces and thus become the largest. It is possible to modify the morphology of crystals if we introduce ions or molecules that change the shapes of growth hillocks by interacting with step edges. In the case of calcium oxalate (CaOx), previous studies^{9,10,11} suggest that some molecules, such as polyaspartic acid, osteopontin (OPN) and citrate, have an effect on growth morphologies and crystal surfaces.

Mechanisms by which ions or molecules may modify or inhibit growth hillocks are step pinning, kink blocking and incorporation¹². All of these mechanisms show a distinctive dependence of step speed on

supersaturation and impurity concentration. Fig. 1.9 shows the expected dependence of step speeds on the concentration resulting from two models of impurity interaction.

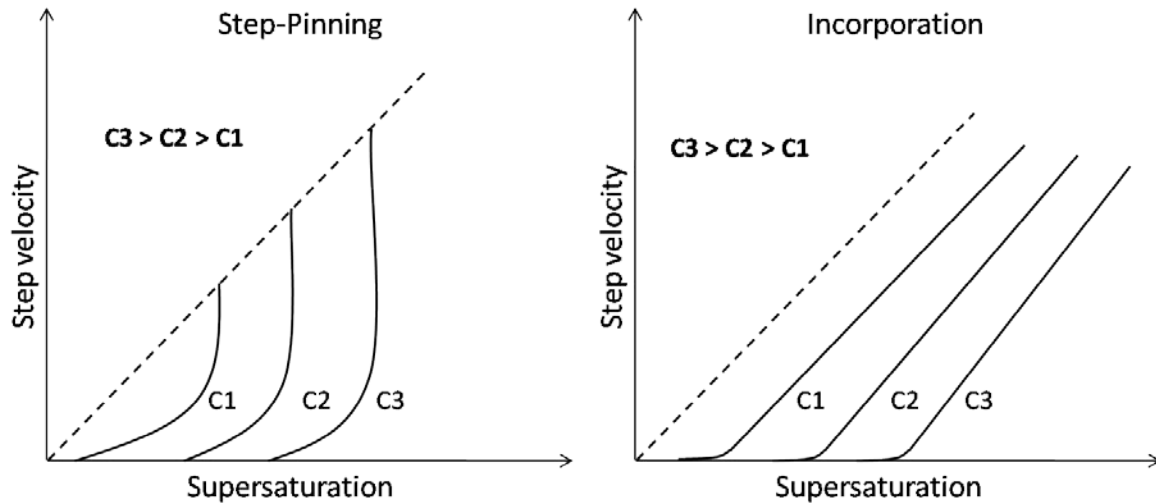


Figure 1.9 Plots of the expected dependence of step speeds on concentration resulting from two models of impurity interaction: step pinning (left); incorporation (right).

Step pinning: certain impurity atoms cannot be incorporated into the bulk crystal, but are strongly adsorbed to the growth face. When a growth step meets these impurities, the only way for it to move forward is to grow around these blocked sites¹³, which forces it to curve, as shown schematically in Fig. 1.10. According to the Gibbs-Thomson equation¹, a curved step has a lower effective supersaturation, and will therefore advance at a lower rate. Fig. 1.10b illustrates the case where the spacing λ of impurity atoms on the surface is less than twice the critical radius r^* , so that an advancing step would be forced to have a radius of curvature smaller than r^* , arresting growth altogether.^{14,15}

Step pinning is primarily reliant on impurity-step interactions. Since impurities might bind more strongly to some faces than to others, ions or molecules that block a step in one direction may have no effect on steps in other directions. This causes a significant change in hillock and crystal shape.

Incorporation: Incorporation takes place when ions or molecules are included or captured by growing steps to become part of a growing crystal. The impurities will alter the growth hillocks and cause

defects in the crystal structure. As a result, it takes less energy to break the crystal structure down so it melts at a lower temperature¹⁶. Consequently, this leads to an increase in solubility and lower effective supersaturation of the growth solution.

The impurity molecules or ions increase the entropy of the solid, which decreases its solubility; thus incorporation does not always lead to an inhibition in growth rates—at sufficiently low concentration, growth can be promoted¹⁷.

Figure 1.10 Effect of impurity atoms adsorbed to growth surfaces on step advance. A growth front is moving with velocity V_0 across a surface containing impurities indicated by red dots. (a) Case where the spacing λ of impurity atoms on the surface is greater than twice the critical radius r^* , so that an advancing step would move through the impurities. (b) Case where spacing λ of impurity atoms on the surface is less than twice the critical radius r^* , so that an advancing step would be forced to have a radius of curvature smaller than r^* , arresting growth altogether.

1.7 Bibliography for Chapter 1

- 1 I. Markov, *Crystal Growth for Beginners: Fundamentals of Nucleation, Crystal Growth, and Epitaxy* (World Scientific, 2004).
- 2 Y. Saito, *Statistical Physics of Crystal Growth* (World Scientific, 1996).
- 3 J. E. Brady and G. E. Humiston, *General chemistry principles and structure*, 3rd ed. (Wiley, 1983).
- 4 P. Debye and E. Hückel, "The theory of electrolytes. I. Lowering of freezing point and related phenomena," *Physikalische Zeitschrift* **24**, 185-206 (1923).
- 5 D.A. Porter and K.E. Easterling, *Phase Transformations in Metals and Alloys* (Chapman & Hall, 1992).
- 6 K. Otsuka and C. M. Wayman, *Shape Memory Materials* (Cambridge University Press, 1998).
- 7 H. Bhadeshia, "<http://www.msm.cam.ac.uk/phase-trans/2002/martensite.html>".
- 8 W. J. Zachowicz, *Physical Chemical Studies of the Kinetics and Energetics of the Nucleation and Growth of Calcium-containing Biominerals*, Ph.D. thesis (State University of New York at Buffalo, 2005).
- 9 J. J. De Yoreo and P. G. Vekilov, "Principles of crystal nucleation and growth," *Biomineralization* **54**, 57-93 (2003).
- 10 J. A. Wesson, E. M. Worcester, J. H. Wiessner, N. S. Mandel, and J. G. Kleinman, "Control of calcium oxalate crystal structure and cell adherence by urinary macromolecules," *Kidney International* **53** (4), 952-957 (1998).
- 11 J. O'Young, *Molecular dynamics and frap analysis of protein-crystal interactions*, Ph.D. thesis (Schulich School of Medicine & Dentistry, The University of Western Ontario, 2008).
- 12 P. M. Dove, J. J. De Yoreo, and K. J. Davis, "Inhibition of CaCO₃ by small molecules: the magnesium example," in *Solid-Fluid Interfaces to Nanostructural Engineering* (Kluwer/Plenum Academic Press, New York, 2005).
- 13 N. Cabrera and D. A. Vermilyea, "The growth of crystals from solution" in *Growth and Perfection of Crystals*, edited by R. H. Doremus, B. W. Roberts, D. Turnbull (Wiley, New York, 1958), pp. 393-410.

- 14 S. Y. Potapenko, "Moving of step through impurity fence," *Journal of Crystal Growth* **133** (1-2), 147-154 (1993).
- 15 S. Y. Potapenko, "Threshold for step percolation through impurity fence," *Journal of Crystal Growth* **133** (1-2), 141-146 (1993).
- 16 K. J. Davis, P. M. Dove, and J. J. De Yoreo, "The role of Mg^{2+} as an impurity in calcite growth," *Science* **290** (5494), 1134-1137 (2000).
- 17 J. M. Astilleros, C. M. Pina, L. Fernandez-Diaz, and A. Putnis, "Molecular-scale surface processes during the growth of calcite in the presence of manganese," *Geochimica Et Cosmochimica Acta* **66** (18), 3177-3189 (2002).

Chapter 2: Background

2.1 Alkanes

2.1.1 Basic concepts

Alkanes are chemical compounds consisting only of carbon and hydrogen linked by single bonds. Alkanes have the general chemical formula (C_nH_{2n+2}), with the number n of carbon atoms used to define the size of the alkane. A series of linked carbon atoms is called a carbon backbone. Alkanes can be linear, in which the carbon atoms are joined in a single snake-like configuration, branched (general chemical formula C_nH_{2n+2} , $n > 3$), in which the carbon backbone splits off in one or more directions, or cyclic (general formula C_nH_{2n} , $n > 2$) in which the carbon backbone forms a loop¹. Linear alkanes are referred to as normal alkanes (n-alkanes).

Important commercial sources of normal alkanes are natural gas (primarily methane and ethane) and oil (a mixture of liquid alkanes and other hydrocarbons). Alkanes are important in the petroleum industry, where short hydrocarbon chains comprise the bulk of fuel products, and longer chains are often undesirable due to their ability to precipitate from solution to form a weak crystalline network that greatly increases fuel viscosity^{2,3}.

2.1.2 Previous work

Alkanes have peculiar phase behavior. Most n-alkanes crystallize with an orthorhombic structure at low temperatures⁴, but pass through a sequence of other solid phases prior to melting as their temperature is increased^{4,5}. Many of these higher temperature phases are known as rotator phases. The rotator phases are characterized by a loss of rotational order about their long axis (i.e., along the hydrocarbon chain), while maintaining a crystalline long-range positional order. This behavior has been the subject of several studies⁶ and is thought to play an important role in the crystallization kinetics of these materials.

The material of interest in this work is tricosane ($C_{23}H_{48}$, hereafter referred to as C_{23}). Previous studies of the phase behavior of tricosane (and other n-alkanes of similar length) have focused on the intriguing solid-solid structural transitions these materials exhibit, which have been known since at least the 1930s⁷. A number of different authors have proposed slightly different sequences, but the general

scheme is that C₂₃ crystallizes into an orthorhombic crystalline structure at temperatures below 38 °C and exhibits a variety of solid structures at higher temperatures up to its melting point of 47 °C, as shown in Table I.

Table I Different phase sequences for tricosane proposed in the literature.

Sirota et al. ⁸ (1993)	$O_{dci} \xrightarrow{38^{\circ}C} R_V \xrightarrow{41.3^{\circ}C} R_I \xrightarrow{44.7^{\circ}C} R_{II} \xrightarrow{47.4^{\circ}C} Liquid$
Nouar et al. ⁹ (1998)	$O_i(\beta_o) \xrightarrow{38.5^{\circ}C} O_{dci}(\beta_o') \xrightarrow{40.3^{\circ}C} R_I \xrightarrow{45.7^{\circ}C} R_{II} \xrightarrow{47.5^{\circ}C} Liquid$
Robles et al. ¹⁰ (1998)	$O_i \xrightarrow{37.7^{\circ}C} O_{dci} \xrightarrow{39.6^{\circ}C} R_V \xrightarrow{42^{\circ}C} R_I \xrightarrow{45.1^{\circ}C} R_{II} \xrightarrow{47.5^{\circ}C} Liquid$

Here phases are identified as orthorhombic (O), rotator (R), and liquid (L). Two orthorhombic crystalline phases, O_i (space group Pcam) and O_{dci} (space group Pnam) have been identified at lower temperatures, while three rotator phases — R_V (monoclinic), R_I (orthorhombic), and R_{II} (hexagonal) — are seen prior to melting¹⁰.

The phase behavior of similar n-alkanes, such as n-eicosane (C₂₁)⁸ and n-pentacosane (C₂₅)¹¹, as well as binary alloys, such as C₂₃/C₂₅¹², have also been studied. In the case of C₂₃/C₂₅, it is reported that very low concentrations of C₂₅ in C₂₃ can have a large qualitative effect on the sequence of phases observed. Fig. 2.1 shows the phase diagram proposed by F. Rajabalee's group¹³ for the binary system of C₂₃-C₂₅. This implies that one of the reasons for the conflicting phase diagram schemes that have been proposed in the literature is differing levels of purity. Understanding of the thermodynamic properties of systems containing polycyclic aromatics and long-chain n-alkanes is important in several petroleum industrial applications, thus binary systems of n-alkane have been widely studied for their thermal and structural behavior.

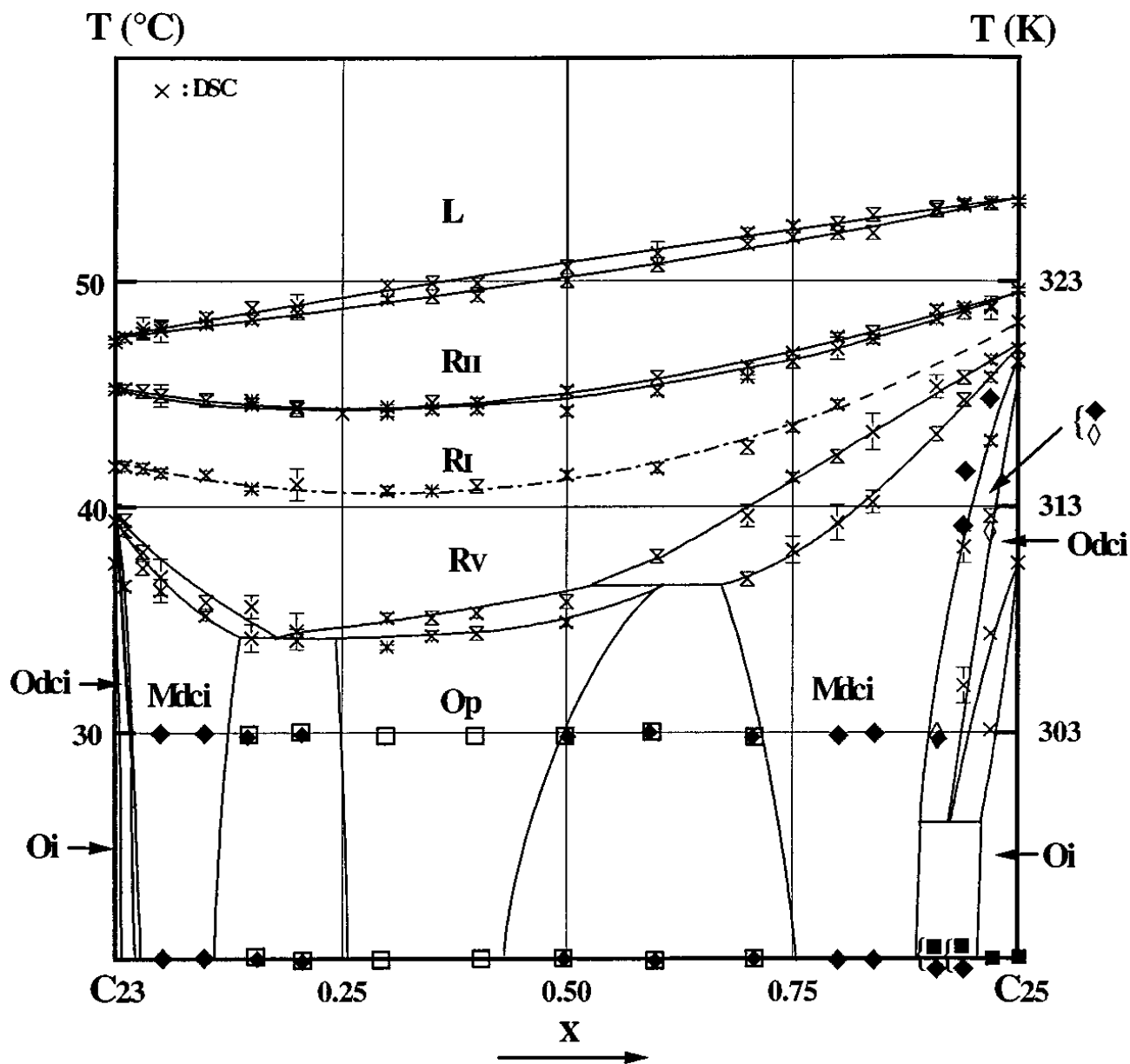


Figure 2.1 Phase diagram for binary system of C₂₃-C₂₅ proposed by F. Rajabalee's group¹³.

Previous work in our research group studied n-alkane crystals at macroscopic scales, in particular the modifications to their growth habits as a result of the presence of kinetic inhibitors¹⁴. Studies on the few-monolayer scale have been done by Merkel's group who looked at alkane coatings on silicon substrates¹⁵. Very few micrometer and sub-micrometer studies have been performed on bulk n-alkane materials. One SEM study revealed the formation of submicrometer-sized "wrinkles" on the surface of

C_{25} crystals when their temperature was changed¹¹, which was attributed to a mechanical stress due to changes in the crystal dimensions resulting from a solid-solid phase change.

Another characteristic of alkane crystallization, which has been previously reported in the literature for tetracosane ($C_{24}H_{50}$)¹⁶ and hexatriacontane $C_{36}H_{74}$)¹⁷, is the existence of twinned structures. Crystal twinning occurs when two or more crystal domains grow such that each is a reflected image of its neighbour. This happens when the two domains share some of the same crystal lattice points in a symmetrical manner, forming a twin boundary separating the two domains. Twinned crystals are broadly classified as contact twins or penetration twins. In case of contact twins, they share a single twin boundary and crystals often appear as mirror images of each other across the boundary. In penetration twins, the individual crystals have the appearance of passing through each other in a symmetrical manner.

2.1.3 Study plan for solid-solid phase transitions in alkanes

I chose to investigate polymorphs of C_{23} , which has interesting phase diagram with at least five solid phases, three of which are called “rotator phases” characterized by positional order without long-range orientational order. The transitions between solid phases of C_{23} can be clearly seen by optical microscopy. While observing the sample using slow temperature ramps, we observed an interesting pattern of twinned domains of tricosane in one of the rotator phases consisting of stripes with a spacing of $\sim 1 \mu\text{m}$ organized into domains with sizes of tens of micrometers. These patterns appear to result from a phase transition involving a local rearrangement of molecules, producing ridges with a triangular profile. Structural analysis of these patterns was performed with optical microscopy. Further, atomic force microscopy was used to study the molecular-scale features of these ridges. Investigations with microbeam X-ray diffraction were carried out to determine the structure of the phases observed.

2.2 Calcium oxalate

2.2.1 Biominerals

The field originally known as calcification¹⁸ is now known by the term “biomineralization.” In this process, living creatures produce inorganic crystals or minerals. The most commonly found calcium based minerals are primarily accompanied by an anionic partner such as phosphate, oxalate, and carbonate¹⁹. A very important example — hydroxyapatite (HA) ($\text{Ca}_5(\text{PO}_4)_3(\text{OH})$), which is the primary mineral in teeth and bones of vertebrates — is one of the best studied²⁰. Magnetite is another type of biomineral extensively studied; it is an iron based biomineral²¹. Amorphous solids are another type of mineralized phase in biological organism²².

2.2.2 Calcium oxalate crystal structures

Calcium Oxalate

Calcium oxalate (CaOx) can be found in plants and fossils, and is a primary constituent in the majority of kidney stones.

Kidney stones are the most common disorder of the urinary tract. Approximately 12% of men and 5% of women will develop a kidney stone during their lifetime²³. Kidney stones are typically made up of inorganic crystal materials surrounded by an organic matrix. Calcium stones, typically combination of calcium oxalate monohydrate and calcium phosphate, are the most common type of kidney stones²⁴.

Stones form when dissolved salts in solution precipitate and crystallize into a solid phase. It has been demonstrated that the composition of stones formed correlates with supersaturation measured in the urine of the stone-forming patient²⁵. A general perception that increasing urine volume would reduce stone formation was proven false when patients examined were found to have an increased rate when their urine volume was increased by an average of 0.3 L per day²⁶.

Calcium oxalate is commonly found as one of three hydrated mineral types: whewellite (calcium oxalate monohydrate, or COM), weddellite (calcium oxalate dihydrate, or COD) and trihydrate (calcium oxalate trihydrate, or COT). COM, the most frequently found form of CaOx, is the most thermodynamically stable phase, with a solubility product of 1.66×10^{-9} and $2.20 \times 10^{-9} \text{ mol}^2/\text{L}^2$ at 25

°C and 35 °C respectively²⁷. In kidney stones, the occurrence of COT is rarely reported, while COM is reported over COD at a ratio around 2:1²⁵. Prien²⁸, in his 23-year survey of kidney stone analysis reports COM as the stone formation basis of all samples. In vitro studies using macromolecules isolated from human urine showed that they were able to inhibit COM growth and favor formation of COD over COM²⁵. Due to lower adhesion to renal epithelial cells, COD are more likely to pass through the urinary track²⁵. These findings suggest a significant role of COM in stone formation.

COM crystal structure

Both of the first two papers on the crystal structure of COM indicate a monoclinic crystal system at room temperature, but differ in space group. Tazzoli and Domenghetti²⁹ reported a $P2_1/c$ space group with unit cell dimensions as $a = 6.290 \text{ \AA}$, $b = 14.583 \text{ \AA}$, $c = 10.116 \text{ \AA}$, and $\beta = 109.46^\circ$. Deganello and Piro³⁰ report COM as space group $P2_1/n$ and a double unit-cell with dimensions as $a = 9.9763 \text{ \AA}$, $b = 14.5884 \text{ \AA}$, $c = 6.2913 \text{ \AA}$ and $\beta = 107.05^\circ$. We have used the Tazzoli scheme to identify crystal faces and directions in this work.

Although Webb³¹ suggested several potential morphologies for synthetic COM crystals, the most common forms are single crystals, contact twins and penetration twins³². Milan indexed the relevant faces as per the most widely used notations by William Miller, known as Miller index system³³. The most commonly studied faces in synthetic and mineral COM crystals are³⁴ $\{010\}$ and $\{121\}$ ³², as indicated in the schematic in Fig. 2.2.

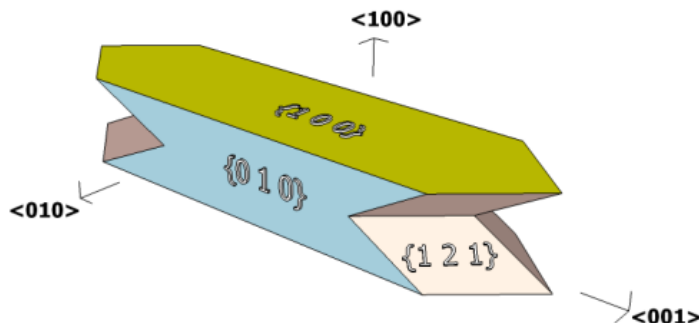


Figure 2.2 Typical growth habit of a calcium oxalate monohydrate crystal with faces and crystallographic directions indicated.

2.2.3 Previous work

The atomic force microscope (AFM) permits near-atomic resolution of a variety of surface features, and can be used to directly observe and probe COM crystals. The AFM can also be used for *in situ* studies to obtain real-time surface scans³⁵, thus permitting observation of crystal growth in a controlled aqueous solution, and to compare growth from pure solution relative to growth in presence of modifiers. AFM studies in pure solution show that {010} and {100} faces of COM grow by advancing steps typically arising from dislocations³⁵. Triangular hillocks initiated at the intersecting {121} faces can be seen on {100} faces³⁶. These steps advance in the <001> direction and are themselves aligned along the {021} direction³⁵. Quadrangle-shaped hillocks bound by {021} and {121} step faces are typically seen on {010} faces³⁶.

A number of elements present in urine can play a preventive role in the formation of COM stones. Urinary citrate can attach to COM surfaces effectively inhibiting the growth of COM crystals³⁷. Macromolecules such as osteopontin(OPN)³⁸, Tamm Horsfall glycoprotein (THP)³⁹, calgranulin⁴⁰, albumin⁴¹ and pro-thrombin F1 fragment⁴² have all been identified as inhibitors of stones. Some of these have anionic rich domains, particularly including aspartic acid and glutamic acid. Some studies

suggest that these proteins may also participate in controlling the morphology of COM stones⁴³, preventing the aggregation of smaller crystals⁴⁴ and adhesion to tubular cells⁴⁵. However, the mechanism by which these molecules effect COM growth is still under investigation.

Studies of urinary OPN, *in vitro*⁴⁶ and by compositional analysis⁴⁷, have shown inhibition of COM crystals. In solution, OPN is disordered protein⁴⁸ with an aspartic acid-rich sequence and glutamic acid rich regions⁴⁹. OPN can be post-translationally (chemical alteration of protein after its translation) modified by phosphorylation⁵⁰, glycosylation⁵¹ and sulfation⁵². The sites of these post-translational modifications have been elucidated for human urinary OPN⁵³. The effect of phosphorylation in modulating COM growth has previously studied by one of our group members²⁴. Furthermore, peptides derived from OPN are able to inhibit COM crystallization, with noticeably superior inhibition upon phosphorylation⁵⁴. OPN also inhibits nucleation⁵⁵ and attachment of COM to renal cells⁵⁶ albeit at concentrations significantly exceeding the levels normally found in urine⁵⁷. Synthetic anionic macromolecules synthesized from amino acids, such as polyaspartate (poy-ASP) and polyglutamate (polyE), demonstrate different effects on COM growth: poly-ASP binds preferentially to {100} faces, while polyE binds mainly to {010}²⁵.

It has been demonstrated that growth of COM crystals in the presence of poly-ASP⁵⁸ or OPN⁵⁹ favors COD formation. Unabridged OPN adsorbs to all the faces of the penetrating-twin COM crystal, particularly to the edges between the {121} and {100} faces, resulting in dumbbell shape morphology with concave {100} faces⁶⁰. OPN produces major morphological modifications and slower step speeds due to pinning by an order of magnitude on {010} faces⁶¹. There was no observed effect on step kinetics of {100} faces, despite adsorption directly on the {100} terraces. Rat-bone OPN favoured adsorption to the edges between {010} and {100} faces of COM penetration-twin crystals⁶⁰.

Recently, our research group has been investigating the interaction between synthetic peptides and COM crystals. Synthetic peptides corresponding to the 220–235 region of rat OPN, a phosphorylated aspartic/glutamic acid-rich sequence possessing 0,1 or 3 phosphorylations (P0, P1 and P3 respectively), all adsorb preferentially to the faces of COM crystal⁶². This claim was further supported by molecular dynamics simulations (MD-simulations) which explain that the phosphorylations play a key role for the increased protein-crystal interaction on COM {100} faces²⁴.

2.2.4 Study plan for calcium oxalate crystallization

Wesson's group⁶³ has shown an effective decrease in in vivo COM crystallization after abdominal injection of 5.1 kDa polyacrylic acid in rats, suggesting that acidic polymers can potentially be used as therapeutic agents in the prevention of kidney stones. Using AFM, Qiu and co-workers showed that human kidney OPN decreased the growth velocity of steps on {010} faces, but despite apparent adsorption had little or no effect on {100} faces⁶¹. Taller and coworkers showed adsorption of rat-bone OPN to entire penetration-twin COM crystals, with preferential adsorption to the edges between the {100} and {010} faces⁶⁰. Our previous group member found a similar adsorption profile for OPN expressed from normal rat kidney cells²⁴. COM {100} crystal surfaces are sufficiently rough that direct AFM imaging of terrace growth and step motion is not feasible. Guo and coworkers⁶⁴ used the AFM to study the growth of etch-pits on COM (100) surfaces, which were created by partially dissolving the COM crystal in pure water, in the presence of a supersaturated solution of calcium oxalate and polymeric additive.

The main objective of this work is to understand the physics of the modification of growth dynamics of COM crystals due to synthetic peptides derived from OPN using atomic force microscopy. A sequence corresponding to the 65–80 residue of OPN (pOPAR), one of the phosphorylated aspartic acid-rich domains in the protein, has shown strong adsorption to COM {100} and {010} faces⁶⁵. The sequence corresponding to the 220–235 residue of OPN contains 3 of the 29 identified phosphorylation sites⁵⁰. This sequence is one of several multi-phosphorylated, aspartic/glutamic acid-rich domains in the protein, and the peptide was synthesized to contain 0 or 3 phosphorylations (P0 and P3)²⁴.

These additives were then used to study the COM (010) surface, which has distinct growth features such as growth hillocks. Supersaturated calcium oxalate solution was used to observe the growth of the hillocks on (010) surfaces in real time using the AFM. The change in the growth velocity due to various macromolecular additives was compared to better understand the nature of the interaction between COM crystals and synthetic additives. These findings are important as they highlight the importance of crystal growth modulation by macromolecular additives, which may lead to the development of inhibitors for the clinical prevention of kidney stones.

We chose to study COM {100} surfaces, which are rough with no observable growth features such as terraces or steps, using the etch-pit regrowth method. Partially dissolved COM (100) crystals with etch-pits will be examined in supersaturated solutions of calcium oxalate. The regrowth rate of the etch-pits will be examined in the presence of OPN peptides at different concentrations to provide a nanoscale picture of the peptide-mineral interaction. We attempt to address the issue related to deficiencies in previously-published analyses of etch-pit growth rate calculations.

2.3 Atomic force microscopy

The first atomic force microscope (AFM) was invented by Binnig, Quate and Gerber⁶⁶ in 1986. In 1989, first commercially available atomic force microscope was introduced. The AFM is now one of the leading tools for imaging and measuring materials at the nanoscale. It belongs to the family of microscopes typically known as scanning probe microscopes, in which a sharp tip is placed close to the surface of the sample and is moved vertically and laterally with sub-nanometer precision as it measures maps some tip-sample interaction. Fig 2.3 shows the schematic diagram for an AFM.

The sample is mounted on a piezoelectric tube scanner. A mechanical probe, typically described as an AFM tip, gathers information by ‘feeling’ the surface. As the AFM tip approaches the sample, the weak cantilever spring on which the tip is mounted deflects due to interactions with the sample surface.

Typically, the AFM senses this deflection by mean of the optical lever technique⁶⁷, wherein laser light is reflected from the back of the cantilever onto position-sensitive photodiodes whose output signal is collected by a differential amplifier. Expressing photodiode output in terms of their labels in Fig. 2.3, the deflection signal is $[(A+B) - (C+D)] / (A+B+C+D)$ and is commonly designated $A-B$. This output signal is proportional to the deflection of the cantilever and amplified by the length of the beam path.

For my thesis, most of the data are collected using contact-mode imaging (in air and fluid), in which the cantilever deflection (due to both short-ranged repulsive forces and attractive forces) is used to generate a topographical image of the sample. In contact mode, the $A-B$ signal is compared to a preselected setpoint voltage and used to adjust the vertical positioning of the piezo tube scanner so that the cantilever deflection remains constant. As the tip is scanned over the sample, a record of the change in

vertical sample position required to compensate for the changing sample heights is used to generate a topographical image of the sample.

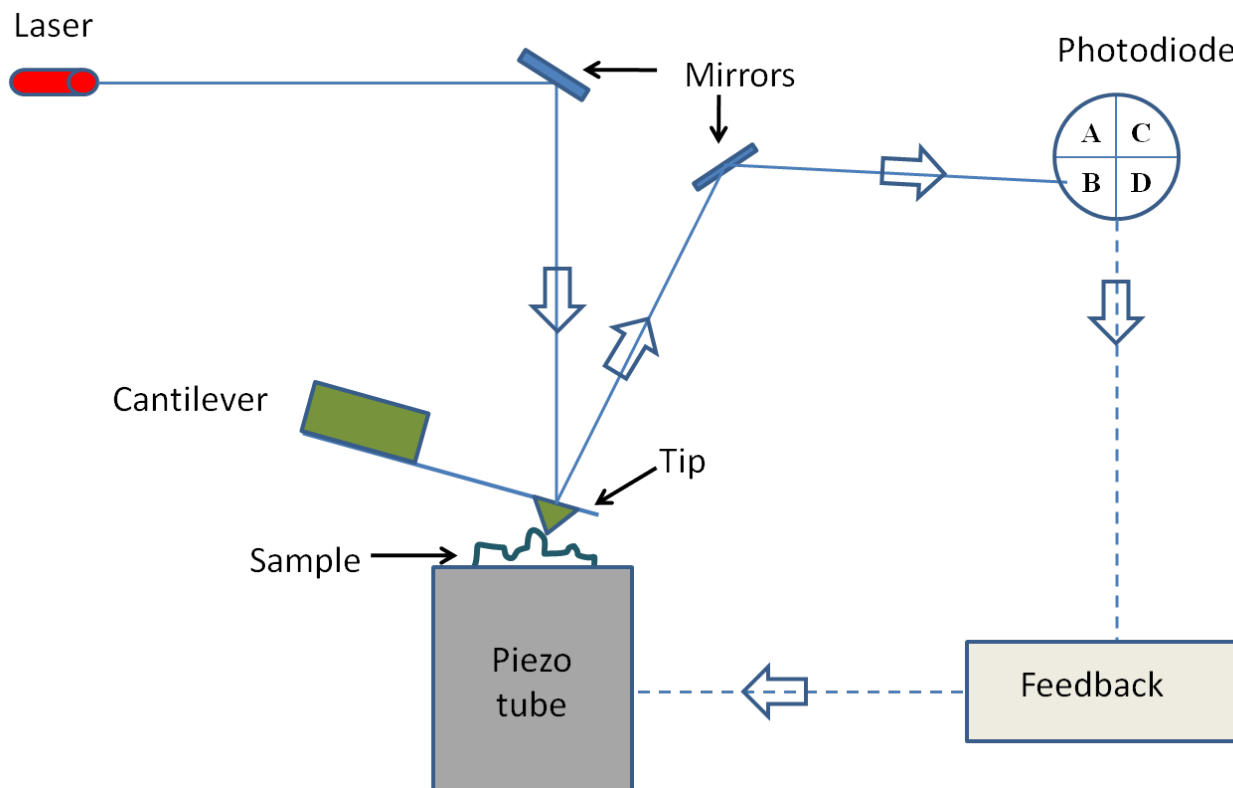


Figure 2.3 A schematic of the parts of an atomic force microscope.

2.4 Bibliography for Chapter 2

- 1 M. Silberberg, *Chemistry: the molecular nature of matter and change* (McGraw-Hill, New York, 2004).
- 2 G. A. Holder and J. Winkler, "Crystal-Growth Poisoning of n-Paraffin Wax By Polymeric Additives and its Relevance to Polymer Crystallization Mechanisms," *Nature* **207** (4998), 719-721 (1965).
- 3 S. R. Reddy, "Increasing the Responsiveness of No. 2-D Diesel Fuels to Flow Improvers by Blending with Low Wax Diluents", Society of Automotive Engineers Technical Paper **841351**, 5922 (1985).

- 4 A. E. Smith, "The Crystal Structure of the Normal Paraffin Hydrocarbons," *Journal of Chemical Physics* **21** (12), 2229-2231 (1953).
- 5 G. Ungar, "Structure of Rotator Phases in Normal-Alkanes," *Journal of Physical Chemistry* **87** (4), 689-695 (1983).
- 6 B. M. Craven, Y. Lange, G. G. Shipley, and J. Steiner, *Handbook of Lipid Research*, Vol. 4, D. M. Small (Ed.), (Plenum Press, New York, 1986).
- 7 A. Muller, "An X-Ray Investigation of Normal Paraffins Near Their Melting Points," *Proceedings of the Royal Society of London, Series A* **138** (836), 514-530 (1932).
- 8 E. B. Sirota, H. E. King, D. M. Singer, and H. H. Shao, "Rotator Phases of the Normal Alkanes - an X-Ray-Scattering Study," *Journal of Chemical Physics* **98** (7), 5809-5824 (1993).
- 9 H. Nouar, D. Petitjean, M. Bouroukba, and M. Dirand, "Binary phase diagram of the system: n-docosane-n-tricosane," *Journal of Molecular Structure* **443** (1-3), 197-204 (1998).
- 10 L. Robles, D. Mondieig, Y. Haget, and M. A. Cuevas-Diarte, "Review on the energetic and crystallographic behaviour of n-alkanes. II. Series from C₂₂H₄₆ to C₂₇H₅₆," *Journal De Chimie Physique Et De Physico-Chimie Biologique* **95** (1), 92-111 (1998).
- 11 K. Nozaki and M. Hikosaka, "Mechanism of primary nucleation and origin of hysteresis in the rotator phase transition of an odd n-alkane," *Journal of Materials Science* **35** (5), 1239-1252 (2000).
- 12 F. Rajabalee, V. Metivaud, D. Mondieig, Y. Haget, and M. A. Cuevas-Diarte, "New insights on the crystalline forms in binary systems of n-alkanes: Characterization of the solid ordered phases in the phase diagram tricosane plus pentacosane," *Journal of Materials Research* **14** (6), 2644-2654 (1999).
- 13 F. Rajabalee, V. Metivaud, D. Mondieig, Y. Haget, and H. A. J. Oonk, "Thermodynamic analysis of solid-solid and solid-liquid equilibria in binary systems composed of n-alkanes: Application to the system tricosane (C₂₃H₄₈) plus pentacosane (C₂₅H₅₂)," *Chemistry of Materials* **11** (10), 2788-2795 (1999).
- 14 J. L. Hutter, S. Hudson, C. Smith, A. Tetervak, and J. Zhang, "Banded crystallization of tricosane in the presence of kinetic inhibitors during directional solidification," *Journal of Crystal Growth* **273** (1-2), 292-302 (2004).

- 15 C. Merkl, T. Pfohl, and H. Riegler, "Influence of the Molecular Ordering on the Wetting of SiO₂/Air Interfaces by Alkanes," *Physical Review Letters* **79** (23), 4625 (1997).
- 16 A. R. Gerson and S. C. Nyburg, "A twinned structure for n-tetracosane," *Acta Crystallographica Section B* **48** (5), 737-741 (1992).
- 17 T. Asano, M. F. Mina, and I. Hatta, "Twin formation mechanism in the solid-solid phase transition of normal hexatriacontane (n-C₃₆H₇₄)," *Journal of the Physical Society of Japan* **65** (6), 1699-1704 (1996).
- 18 W. J. Schmidt, *Die Bausteine des Tierkörpers in polarisiertem Lichte* (F. Cohen, Bonn, 1924).
- 19 S. Weiner, P. M. Dove, "An overview of biomineralization processes and the problem of the vital effect," *Biomineralization* **54**, 1-29 (2003).
- 20 H. A. Goldberg, K. J. Warner, M. J. Stillman, and G. K. Hunter, "Determination of the hydroxyapatite-nucleating region of bone sialoprotein," *Connective Tissue Research* **35** (1-4), 385-392 (1996).
- 21 H. A. Lowenstam and S. Weiner, *On biomineralization* (Oxford University Press, 1989).
- 22 C. C. Perry, "Silicification: The processes by which organisms capture and mineralize silica," *Biomineralization*, **54**, 291-327 (2003).
- 23 F. L. Coe, A. Evan, and E. Worcester, "Kidney stone disease," *Journal of Clinical Investigation* **115** (10), 2598-2608 (2005).
- 24 J. O'Young, *Molecular dynamics and FRAP analysis of protein-crystal interactions* (Schulich School of Medicine & Dentistry, The University of Western Ontario, 2008).
- 25 X. Sheng, *Face-specific Molecular Adhesion and Binding to calcium oxalate monohydrate: Implication for kidney stone formation* (Department of Chemical Engineering, University of Minnesota, 2004).
- 26 J. H. Parks, E. R. Goldfischer, and F. L. Coe, "Changes in urine volume accomplished by physicians treating nephrolithiasis," *Journal of Urology* **169** (3), 863-866 (2003).
- 27 W. J. Zachowicz, *Physical Chemical Studies of the Kinetics and Energetics of the Nucleation and Growth of Calcium-containing Biominerals* (State University of New York at Buffalo, 2005).
- 28 E. L. Prien, "Crystallographic Analysis Of Urinary Calculi - A 23-Year Survey Study," *Journal of Urology* **89** (6), 917- 924 (1963).

- 29 V. Tazzoli and C. Domeneghetti, "The Crystal-Structures of Whewellite and Weddellite - Reexamination and Comparison," *American Mineralogist* **65** (3-4), 327-334 (1980).
- 30 S. Deganello and O. E. Piro, "The Crystal-Structure of Calcium-Oxalate Monohydrate (Whewellite)," *Neues Jahrbuch Fur Mineralogie-Monatshefte* (2), 81-88 (1981).
- 31 M. A. Webb, "Cell-mediated crystallization of calcium oxalate in plants," *Plant Cell* **11** (4), 751-761 (1999).
- 32 A. Millan, "Crystal growth shape of whewellite polymorphs: Influence of structure distortions on crystal shape," *Crystal Growth & Design* **1** (3), 245-254 (2001).
- 33 W. H. Miller, *A Treatise on Crystallography* (Cambridge, 1939).
- 34 A. A. Abrosimov, Z. M. Pishchaeva, V. A. Vinokurov, S. T. Bashkatova, and T. P. Vishnyakova, "Daks-D depressant additive for diesel fuels," *Chemistry and Technology of Fuels and Oils* **35** (5), 300-301 (1999).
- 35 T. Jung, X. X. Sheng, C. K. Choi, W. S. Kim, J. A. Wesson, and M. D. Ward, "Probing crystallization of calcium oxalate monohydrate and the role of macromolecule additives with in situ atomic force microscopy," *Langmuir* **20** (20), 8587-8596 (2004).
- 36 S. R. Qiu, A. Wierzbicki, E. A. Salter, S. Zepeda, C. A. Orme, J. R. Hoyer, G. H. Nancollas, A. M. Cody, and J. J. De Yoreo, "Modulation of calcium oxalate monohydrate crystallization by citrate through selective binding to atomic steps," *Journal of the American Chemical Society* **127** (25), 9036-9044 (2005).
- 37 F. L. Coe, J. H. Parks, and Y. Nakagawa, *Inhibitors and promoters of calcium oxalate crystallization* (Raven Press Ltd., New York, 1992).
- 38 J. R. Asplin, D. Arsenault, J. H. Parks, F. L. Coe, and J. R. Hoyer, "Contribution of human uropontin to inhibition of calcium oxalate crystallization," *Kidney International* **53** (1), 194-199 (1998).
- 39 B. Hess, Y. Nakagawa, J. H. Parks, and F. L. Coe, "Molecular Abnormality Of Tamm-Horsfall Glycoprotein In Calcium-Oxalate Nephrolithiasis," *American Journal of Physiology* **260** (4), F569-F578 (1991).
- 40 S. N. Pillay, J. R. Asplin, and F. L. Coe, "Evidence that calgranulin is produced by kidney cells and is an inhibitor of calcium oxalate crystallization," *American Journal of Physiology-Renal Physiology* **275** (2), F255-F261 (1998).

- 41 F. L. Coe and J. H. Park, "Pathogenesis and treatment of nephrolithiasis", in *The Kidney*, edited by D. Seldin and G. Giebisch, (Lippincott Williams & Wilkins, 2000, pp. 1841-1867).
- 42 A. M. F. Stapleton and R. L. Ryall, "Blood-Coagulation Proteins And Urolithiasis Are Linked - Crystal Matrix Protein Is The F1 Activation Peptide Of Human Prothrombin," *British Journal of Urology* **75** (6), 712-719 (1995).
- 43 A. Okada, S. Nomura, Y. Saeki, Y. Higashibata, S. Hamamoto, M. Hirose, Y. Itoh, T. Yasui, K. Tozawa, and K. Kohri, "Morphological Conversion of Calcium Oxalate Crystals Into Stones Is Regulated by Osteopontin in Mouse Kidney," *Journal of Bone and Mineral Research* **23** (10), 1629-1637 (2008).
- 44 J. A. Wesson, V. Ganne, A. M. Beshensky, and J. G. Kleinman, "Regulation by macromolecules of calcium oxalate crystal aggregation in stone formers," *Urological Research* **33** (3), 206-212 (2005).
- 45 T. Yasui, K. Fujita, K. Asai, and K. Kohri, "Osteopontin regulates adhesion of calcium oxalate crystals to renal epithelial cells," *International Journal of Urology* **9** (2), 100-108 (2002).
- 46 H. Shiraga, W. Min, W. J. Vandusen, M. D. Clayman, D. Miner, C. H. Terrell, J. R. Sherbotie, J. W. Foreman, C. Przywiecki, E. G. Neilson, and J. R. Hoyer, "Inhibition of Calcium-Oxalate Crystal-Growth In vitro by Uropontin - Another Member of the Aspartic Acid-Rich Protein Superfamily," *Proceedings of the National Academy of Sciences of the United States of America* **89** (1), 426-430 (1992).
- 47 M. D. McKee, A. Nanci, and S. R. Khan, "Ultrastructural Immunodetection of Osteopontin and Osteocalcin as Major Matrix Components of Renal Calculi," *Journal of Bone and Mineral Research* **10** (12), 1913-1929 (1995).
- 48 L. W. Fisher, D. A. Torchia, B. Fohr, M. F. Young, and N. S. Fedarko, "Flexible structures of SIBLING proteins, bone sialoprotein, and osteopontin," *Biochemical and Biophysical Research Communications* **280** (2), 460-465 (2001).
- 49 A. Oldberg, A. Franzen, and D. Heinegard, "Cloning and Sequence-Analysis of Rat Bone Sialoprotein (Osteopontin) Cdna Reveals an Arg-Gly-Asp Cell-Binding Sequence," *Proceedings of the National Academy of Sciences of the United States of America* **83** (23), 8819-8823 (1986).

- 50 M. Keykhosravani, A. Doherty-Kirby, C. J. Zhang, D. Brewer, H. A. Goldberg, G. K. Hunter, and G. Lajoie, "Comprehensive identification of post-translational modifications of rat bone osteopontin by mass spectrometry," *Biochemistry* **44** (18), 6990-7003 (2005).
- 51 K. Singh, M. W. Devouge, and B. B. Mukherjee, "Physiological Properties and Differential Glycosylation of Phosphorylated and Nonphosphorylated Forms of Osteopontin Secreted by Normal Rat-Kidney Cells," *Journal of Biological Chemistry* **265** (30), 18696-18701 (1990).
- 52 S. Kasugai, R. Todescan, T. Nagata, K. L. Yao, W. T. Butler, and J. Sodek, "Expression of Bone-Matrix Proteins Associated with Mineralized Tissue Formation by Adult-Rat Bone-Marrow Cells-Invitro - Inductive Effects of Dexamethasone on the Osteoblastic Phenotype," *Journal of Cellular Physiology* **147** (1), 111-120 (1991).
- 53 B. Christensen, C. C. Kazanecki, T. E. Petersen, S. R. Rittling, D. T. Denhardt, and E. S. Sorensen, "Cell type-specific post-translational modifications of mouse osteopontin are associated with different adhesive properties," *Journal of Biological Chemistry* **282** (27), 19463-19472 (2007).
- 54 J. R. Hoyer, J. R. Asplin, and L. Otvos, "Phosphorylated osteopontin peptides suppress crystallization by inhibiting the growth of calcium oxalate crystals," *Kidney International* **60** (1), 77-82 (2001).
- 55 E. M. Worcester, C. Snyder, and A. M. Beshensky, "Osteopontin Inhibits Heterogeneous Nucleation of Calcium-Oxalate," *Journal of the American Society of Nephrology* **6** (3), 956-956 (1995).
- 56 J. C. Lieske, R. Leonard, and F. G. Toback, "Adhesion of Calcium-Oxalate Monohydrate Crystals to Renal Epithelial-Cells Is Inhibited by Specific Anions," *American Journal of Physiology-Renal Physiology* **268** (4), F604-F612 (1995).
- 57 W. Min, H. Shiraga, C. Chalko, S. Goldfarb, G. G. Krishna, and J. R. Hoyer, "Quantitative studies of human urinary excretion of uropontin," *Kidney International* **53** (1), 189-193 (1998).
- 58 J. A. Wesson and E. Worcester, "Formation of hydrated calcium oxalates in the presence of poly-L-aspartic acid," *Scanning Microscopy* **10** (2), 415-424 (1996).
- 59 J. A. Wesson, E. M. Worcester, J. H. Wiessner, N. S. Mandel, and J. G. Kleinman, "Control of calcium oxalate crystal structure and cell adherence by urinary macromolecules," *Kidney International* **53** (4), 952-957 (1998).

- 60 A. Taller, B. Grohe, K. A. Rogers, H. A. Goldberg, and G. K. Hunter, "Specific adsorption of osteopontin and synthetic polypeptides to calcium oxalate monohydrate crystals," *Biophysical Journal* **93** (5), 1768-1777 (2007).
- 61 S. R. Qiu, A. Wierzbicki, C. A. Orme, A. M. Cody, J. R. Hoyer, G. H. Nancollas, S. Zepeda, and J. J. De Yoreo, "Molecular modulation of calcium oxalate crystallization by osteopontin and citrate," *Proceedings of the National Academy of Sciences of the United States of America* **101** (7), 1811-1815 (2004).
- 62 B. Grohe, J. O'Young, D. A. Ionescu, G. Lajoie, K. A. Rogers, M. Karttunen, H. A. Goldberg, and G. K. Hunter, "Control of calcium oxalate crystal growth by face-specific adsorption of an osteopontin phosphopeptide," *Journal of the American Chemical Society* **129** (48), 14946-14951 (2007).
- 63 J. G. Kleinman, L. J. Alatalo, A. M. Beshensky, and J. A. Wesson, "Acidic polyanion poly(acrylic acid) prevents calcium oxalate crystal deposition," *Kidney International* **74** (7), 919-924 (2008).
- 64 S. W. Guo, M. D. Ward, and J. A. Wesson, "Direct visualization of calcium oxalate monohydrate crystallization and dissolution with atomic force microscopy and the role of polymeric additives," *Langmuir* **18** (11), 4284-4291 (2002).
- 65 S. Hug, B. Grohe, J. Jalkanen, B. Chan, B. Galarreta, K. Vincent, F. Lagugne-Labarthet, G. Lajoie, H. A. Goldberg, M. Karttunen, and G. K. Hunter, "Mechanism of inhibition of calcium oxalate crystal growth by an osteopontin phosphopeptide," *Soft Matter* **8** (4), 1226-1233 (2012).
- 66 G. Binnig, C. F. Quate, and C. Gerber, "Atomic Force Microscope," *Physical Review Letters* **56** (9), 930-933 (1986).
- 67 G. Meyer and N. M. Amer, "Novel optical approach to atomic force microscopy," *Applied Physics Letters* **53** (12), 1045-1047 (1988).

Chapter 3: Diffusionless Transition in Tricosane

3.1 Introduction

The normal alkanes (n-alkanes, with chemical formula C_nH_{2n+2}) are the simplest of all organic molecules, consisting of a single saturated hydrocarbon chain. These compounds are particularly important in the petroleum industry, where short hydrocarbon chains comprise the bulk of fuel products, and longer chains are often undesirable due to their ability to precipitate from solution to form a weak crystalline network that greatly increases fuel viscosity^{1,2}. Longer chains are also a major component of paraffin waxes, and can be thought of as the short-chain limit of polyethylene, the simplest of all polymers.

In addition to their commercial value, n-alkanes are interesting for their phase behavior. Most n-alkanes crystallize with an orthorhombic structure at low temperatures³, but pass through a sequence of other solid phases prior to melting as their temperature is raised^{4,5}. Several of these higher temperature phases—known generically as “rotator phases”—are characterized by a loss of rotational order about their long axis (i.e., along the hydrocarbon chain), while maintaining a crystalline long-range positional order. This liquid-crystalline-like behavior has been the subject of numerous investigations⁶ and is believed to play a major role in the crystallization kinetics of these materials⁷.

In this Chapter, we describe a curious pattern of twinned domains that occurs in the phase sequence of a particular n-alkane, tricosane ($C_{23}H_{48}$, hereafter referred to as C_{23}). Phase transitions between this twinned regime and one of its neighboring phases preserve atomic-scale features such as growth steps, indicating that the regime is entered via a diffusionless (martensitic-like) transition. We examine this structure by optical microscopy, which shows a pattern of stripes with a spacing of $\sim 1 \mu\text{m}$ organized into domains with sizes of tens of micrometers, as shown in Fig. 3.1. Characterization by atomic-force microscopy reveals that the stripes consist of ridges with a triangular cross-section. Microbeam X-ray diffraction allows us to determine the structure of the phases observed.

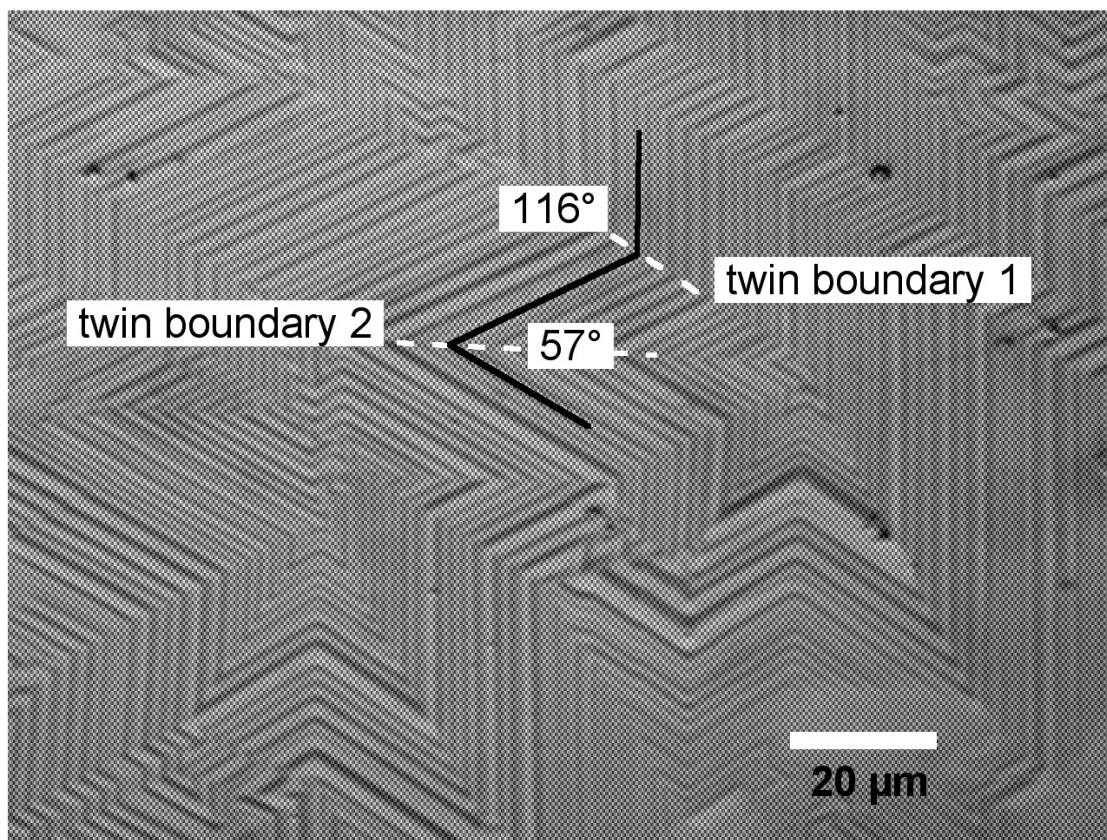


Figure 3.1 Optical micrograph of a pattern of stripes in C_{23} at a temperature of 315.6 K. Stripes are separated into domains separated by two types of twin boundaries, as discussed in the text.

3.2 Background

Studies of the phase behavior of tricosane (and other n-alkanes of similar length) have focused on the intriguing polymorphs these materials exhibit, which have been known since at least the 1930s⁸. A number of different authors have proposed slightly different sequences, but the general scheme is that C_{23} crystallizes into an orthorhombic crystalline structure at temperatures below 38 °C and exhibits a variety of solid structures at higher temperatures up to its melting point of 47 °C as shown in Table II, where the phases are identified as orthorhombic (O), rotator (R), and liquid (L). Two orthorhombic crystalline phases, O_i (space group $Pcam$) and O_{dc} (space group $Pnam$) have been identified at lower

temperatures, while three rotator phases— R_V (monoclinic), R_I (orthorhombic), and R_{II} (hexagonal)—are seen prior to melting⁹.

Table II Phase behavior of tricosane. The precision of our observed transition temperature is approximately ± 0.2 K.

Robles et al. ⁹ (1998)	$O_i \xrightarrow{37.7^\circ C} O_{dci} \xrightarrow{39.6^\circ C} R_V \xrightarrow{42^\circ C} R_I \xrightarrow{45.1^\circ C} R_{II} \xrightarrow{47.5^\circ C} Liquid$
This work	$O_i \xrightarrow{37.8^\circ C} O_{dci} \xrightarrow{39.8^\circ C} R_V \xrightarrow{42.4^\circ C} R_I \xrightarrow{44.7^\circ C} R_{II} \xrightarrow{47.5^\circ C} Liquid$

The phase behavior of related n-alkanes, such as n-eicosane (C_{21})⁴ and n-pentacosane (C_{25})¹⁰, as well as binary alloys, such as C_{23}/C_{25} ¹¹ have also been studied. In the latter case, we note that even very low concentrations of C_{25} in C_{23} can have a qualitative effect on the sequence of phases observed, suggesting that one reason for the differing schemes (e.g., those of Refs. [4,12]) that have been proposed is differing levels of purity.

Although there have been a number of studies of n-alkane crystals at macroscopic scales (in particular on the modifications to their growth habits as a result of the presence of kinetic inhibitors¹³), and at the scale of a few monolayers (for instance as coatings on silicon substrates¹⁴), very few micrometer and sub-micrometer studies have been performed on bulk n-alkane materials. One SEM study revealed the formation of sub-micrometer-sized “wrinkles” on the surface of C_{25} crystals¹⁰, which the authors ascribed to a mechanical stress due to changes in the crystal dimensions resulting from crystallization.

3.3 Experimental

n-tricosane ($C_{23}H_{48}$) with a purity of 99% was obtained from Alfa Aesar. Crystalline samples were prepared by melting a small quantity of C_{23} on heated glass or silicon substrates and covering with a second substrate to form a thin solid film on freezing. In some cases, large crystals (as much as 80 μm across) were produced by repeated freeze/thaw cycles at slow ramp rates or by annealing just below the melting point (e.g., for microbeam X-ray diffraction studies of a single domain).

Optical microscopy was performed using an Olympus BX60 microscope equipped with a temperature controlled stage (Instec STC200), with active heating (via a resistive heater) and cooling (via vapor extracted from a dewar containing liquid nitrogen). Image and video data was acquired using a CCD camera (Sony DXC-390) and frame-grabber card (Scion CG7). Optical data was analyzed using Scion Image, a version of NIH Image (National Institutes of Health, Bethesda, MD).

Samples were also studied by atomic force microscopy using a Multimode AFM with a Nanoscope IIIa controller (Veeco Instruments, Santa Barbara, CA). In this case, temperature control was achieved with a heating stage capable of attaining temperatures in the range of ambient to 60 °C, but without active cooling.

The crystalline structures of the resulting C₂₃ samples were determined using microbeam X-ray diffraction (μ XRD). The μ XRD data were collected using a Bruker-AXS D8 Discover micro X-ray diffractometer having theta-theta geometry. Cu $K\alpha$ radiation (wavelength 1.5418 Å) was produced in a sealed Cu tube at 40 kV and 40 mA. The X-ray beam was parallelized using a Göbel mirror parallel optics system and collimated to produce a 500 μ m beam diameter. The sample was placed on the XYZ stage and analyzed using either omega scan mode or coupled scan mode: In omega scan mode, both source (θ_1) and detector (θ_2) are scanned through a range of angles maintaining a constant observed angle in 2θ (where $\theta_1 + \theta_2 = 2\theta$). This enables a range of crystal lattice orientations to satisfy the Bragg's Law diffraction condition, although the sample remains stationary. In coupled scan mode, the source and detector are scanned together such that the angle of incidence (θ_1) equals the angle of reflection (θ_2) (i.e., $\theta_1 = \theta_2$ and $\theta_1 + \theta_2 = 2\theta$), while the sample remains stationary. The X-ray diffraction data were collected using a two-dimensional general area detector diffraction system (GADDS), which enabled determination of intensity as both a function of scattering angle and orientation of individual crystals. For a more detailed description of instrument geometry see Flemming (2007)¹⁵.

In order to control sample temperature, the Instec stage was installed inside the X-ray enclosure. Some care was necessary to position the stage and sample so as not to interfere with the incident and diffracted X-ray beams.

3.4 Results & Discussion

3.4.1 Phase behavior

Transitions between the solid phases of C_{23} are readily seen by optical microscopy. By observing the samples during slow temperature ramps we observed phase transitions at temperatures indicated in the bottom row of Table I. Using X-ray diffraction at controlled temperatures, we were able to acquire structural data corresponding to each of the observed phases. In most cases, we could use the phase diagram proposed by Mondieig⁹ to aid in the structure determination. This allowed us to estimate the lattice parameters, which could then be refined based on the expected structure and our diffraction data using LSUCRIPC (Least Squares Unit Cell Refinement with Indexing on Personal Computer, implementation by Roy Garvey)¹⁶.

For example, observed peaks and assigned Miller indices for the low temperature orthorhombic phase O_i (measured at a temperature of 307.2 K) are shown in Fig. 3.2 and Table III. This diffraction pattern clearly shows a series of peaks corresponding to $0\ 0\ 2n$ reflections from which we determine a unit cell height of $62.02 \pm 0.04\ \text{\AA}$, which is approximately twice the length of a fully extended $C_{23}H_{48}$ molecule. The fact that the $0\ 0\ 2n$ peaks are clearly seen while certain others that might be expected, e.g., peaks corresponding to $2\ 0\ 2$ and $2\ 1\ 0$ reflections, are systematically absent may be a consequence of crystal orientation. Because alkanes tend to form plate-like crystals whose c -axis is perpendicular to the plates, preparing samples in a thin film preferentially produces horizontal plates ideally oriented to meet the Bragg condition for $(0\ 0\ 2n)$ planes during a diffraction scan. Two other strong peaks due to $1\ 1\ 0$ and $0\ 2\ 0$ reflections allow the a and b parameters to also be measured, yielding a unit cell of dimensions $a = 7.472 \pm 0.008\ \text{\AA}$, $b = 4.945 \pm 0.008\ \text{\AA}$, and $c = 62.02 \pm 0.04\ \text{\AA}$, which are in very close agreement with values of $7.467 \pm 0.008\ \text{\AA}$, $4.983 \pm 0.007\ \text{\AA}$, and $62.19 \pm 0.04\ \text{\AA}$, respectively, determined by Rajabalee, et al. at a temperature of 291 K¹¹. Our parameters indicate a unit cell with a volume of $2292 \pm 5\ \text{\AA}^3$. Given $Z = 4$ molecules per unit cell and a molecular weight for $C_{23}H_{48}$ of 324.6 g/mol, we can calculate a density of $0.941 \pm 0.002\ \text{g/cm}^3$.

The orthorhombic phase observed at 311 K produces an XRD pattern virtually identical to that seen at 307 K (see Fig. 3.2 and Tables III and IV). Nevertheless, a clear transformation was observed optically at 310.8 K, even in the low-power microscope present in the X-ray diffractometer, convincing us that

the tricosane sample is in a different phase at this temperature. The unit cell parameters for this phase were $a = 7.419 \pm 0.015 \text{ \AA}$, $b = 4.980 \pm 0.010 \text{ \AA}$, and $c = 62.05 \pm 0.11 \text{ \AA}$, in fair agreement with the values of $7.546 \pm 0.008 \text{ \AA}$, $4.989 \pm 0.007 \text{ \AA}$, and $62.26 \pm 0.04 \text{ \AA}$ found by Rajabalee, et al.¹¹ These parameters also indicate a unit cell volume of $2292 \pm 8 \text{ \AA}^3$ and sample density of $0.940 \pm 0.003 \text{ g/cm}^3$.

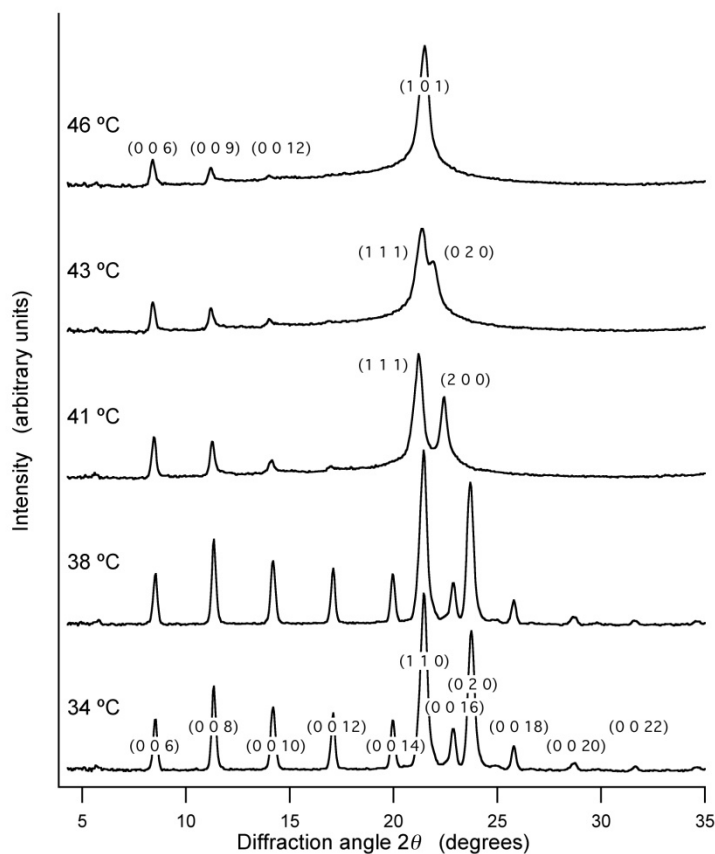


Figure 3.2 X-ray diffraction patterns for the five polymorphs of tricosane observed, with principal peaks labeled according to their Miller indices. In addition to the changes in structure, the sequence is characterized by a progressive loss of higher-order Bragg peaks, possibly due to the lack of rotational order in the high-temperature rotator phases.

At temperatures between approximately 313 K and 315 K, Fig. 3.2 shows a structure that is clearly different from those at lower temperatures. The principal Bragg peaks are inconsistent with an orthorhombic structure. Some authors^{4,9} have proposed a monoclinic structure at this temperature.

However, aside from the obvious $0\ 0\ 2n$ series, we observe only two additional peaks (see Table V), rendering it impossible to determine the four lattice constants (the cell dimensions a , b , c , and an angle β) needed to characterize the structure. In Section 3.4.3 below, we identify these as $1\ 1\ 1$ and $2\ 0\ 0$ reflections.

When the temperature is increased still further to 316 K, a new polymorph is seen (see Fig. 3.2 and Table VI). This phase has been previously identified as an orthorhombic rotator phase⁹, but with a different space group ($Fmmm$, space group 69) than the ones observed at lower temperatures.

Refinement based on this structure identifies the Bragg peaks as corresponding to the familiar $0\ 0\ 2n$ series, as well as to $(1\ 1\ 1)$ and $(0\ 2\ 0)$ planes. The latter two peaks are somewhat broad, suggesting the presence of additional overlapping peaks, though the lack of molecular orientational order likely also plays a role. Refined unit cell parameters for this structure are $a = 8.074 \pm 0.008\ \text{\AA}$, $b = 4.843 \pm 0.007\ \text{\AA}$, and $c = 62.63 \pm 0.05\ \text{\AA}$. The volume of $2449 \pm 5\ \text{\AA}^3$ calculated for this structure implies a sample density of $0.880 \pm 0.002\ \text{g/cm}^3$.

Fig. 3.2 reveals that the final structure observed below the melting point is again different, this time dominated by a single peak aside from the $0\ 0\ l$ reflections. These data are explained well by the hexagonal R_{II} rotator phase described in the literature, the $0\ 0\ l$ reflections then having the form $0\ 0\ 3n$, and the single large peak due to reflections from $(1\ 0\ 1)$ planes (see Table A.V for a listing of reflections). Refinement reveals lattice parameters of $a = 4.769 \pm 0.007\ \text{\AA}$, $c = 94.14 \pm 0.16\ \text{\AA}$, in close agreement with the values found by Ungar⁵, a unit cell volume of $1854 \pm 4\ \text{\AA}^3$, and a density (with $Z = 3$) of $0.872 \pm 0.002\ \text{g/cm}^3$.

3.4.2 Domain Structure

In all of its polymorphs, tricosane forms plate-like crystals that tend to lie horizontally, with the c -axis vertical, due to the thin geometry of our samples. The monoclinic phase invariably forms patterns consisting of domains of stripes of width 0.5–2.5 μm , as shown in the optical micrograph of Fig. 3.1. Because the stripes consistently meet at one of two angles, 116° or 57° , it is clear that they are crystallographic in origin. Because the domain boundaries always bisect the angle formed by stripes on either side of the boundary, we believe that these boundaries separate twinned regions. The existence of twinned structures in alkane crystallization has been previously reported, e.g., for tetracosane ($\text{C}_{24}\text{H}_{50}$)¹⁷ and hexatriacontane ($\text{C}_{36}\text{H}_{74}$)¹⁸.

Fig. 3.3 shows atomic force microscope (AFM) images of a twinned region. The topographical image (Fig. 3.3a) reveals that the stripes consist of ridges of height ~ 50 nm. The “deflection image” of Fig. 3.3b shows particularly good contrast for the stripes. This is due to the contrast mechanism for deflection images. In contact-mode AFM imaging, a sharp microfabricated tip attached to a weak cantilever spring is brought into contact with the sample, which is then moved laterally in a raster scan. A feedback loop responds to topological features by moving the sample vertically during the scan so as to maintain a constant force, as sensed by the cantilever. Two images are typically recorded: a topographical image, which is a map of the required vertical motion as a function of sample position, and a deflection image, which is a record of the error in the feedback loop. Thus, the alternating bands of constant intensity in Fig. 3.3b indicate an error in the feedback loop that alternates between two constant values. This shows that the ridges have planar surfaces (i.e., a triangular profile), so that the feedback loop reaches a steady-state error during ascent and descent of the ridges. The differing contrasts for different domains are due to differing ridge orientations. For instance, the central triangular domain shows weak contrast because the ridges are nearly parallel to the scan direction (horizontal in the figure) so that the sample height changes relatively slowly in the scan direction, whereas the region in the upper-right portion of the figure shows strong contrast because the sample height changes relatively rapidly as the tip traverses ridges perpendicular to the scan direction.

The triangular profile of the ridges is seen more clearly in Fig. 3.3c, which shows a cross-section of the topographical image along the dashed line indicated in Fig. 3.3a. This profile shows that the ridges are symmetric, with sides inclined at an 8° angle to the horizontal.

We propose that the striped pattern in the monoclinic domain is the result of a highly-twinned crystalline structure with three distinct twin-planes, each of which is parallel to the c -axis. The stripes themselves are polysynthetic twins, as evidenced by their symmetric shape. Domains of stripes are bounded by two types of twin planes (identified as twin plane 1 and twin plane 2 in Fig. 3.1). Thus, contact twins of the stripe patterns are seen upon crossing the twin plane or domain boundary. Twinned individuals are observed in the GADDS images as two spots having the same 2θ , but with different orientations (see Fig. 3.4). However, due to an insufficient number of Bragg peaks, X-ray diffraction alone does not allow us to identify the particular twin planes involved.

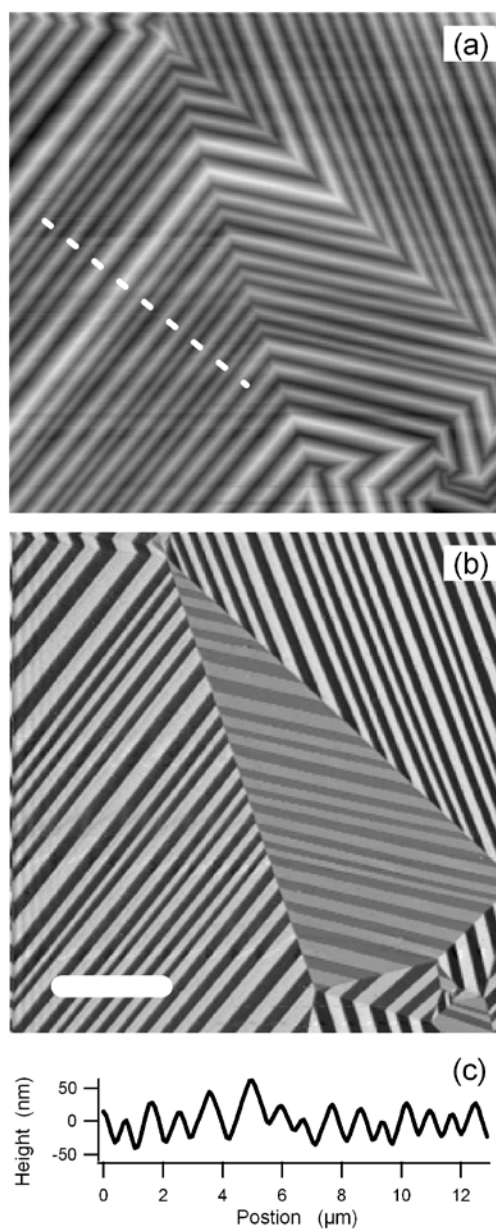


Figure 3.3 AFM study of the twinning pattern observed for C_{23} in the R_V phase at 41°C . (a) AFM height image, shown with a gray scale spanning 150 nm. (b) Deflection image (arbitrary gray scale). The uniform contrast of individual portions of each stripe indicated in (a). Note that the ridges have a triangular profile (c) with typical heights ~ 50 nm and sides with an inclination of 8° .

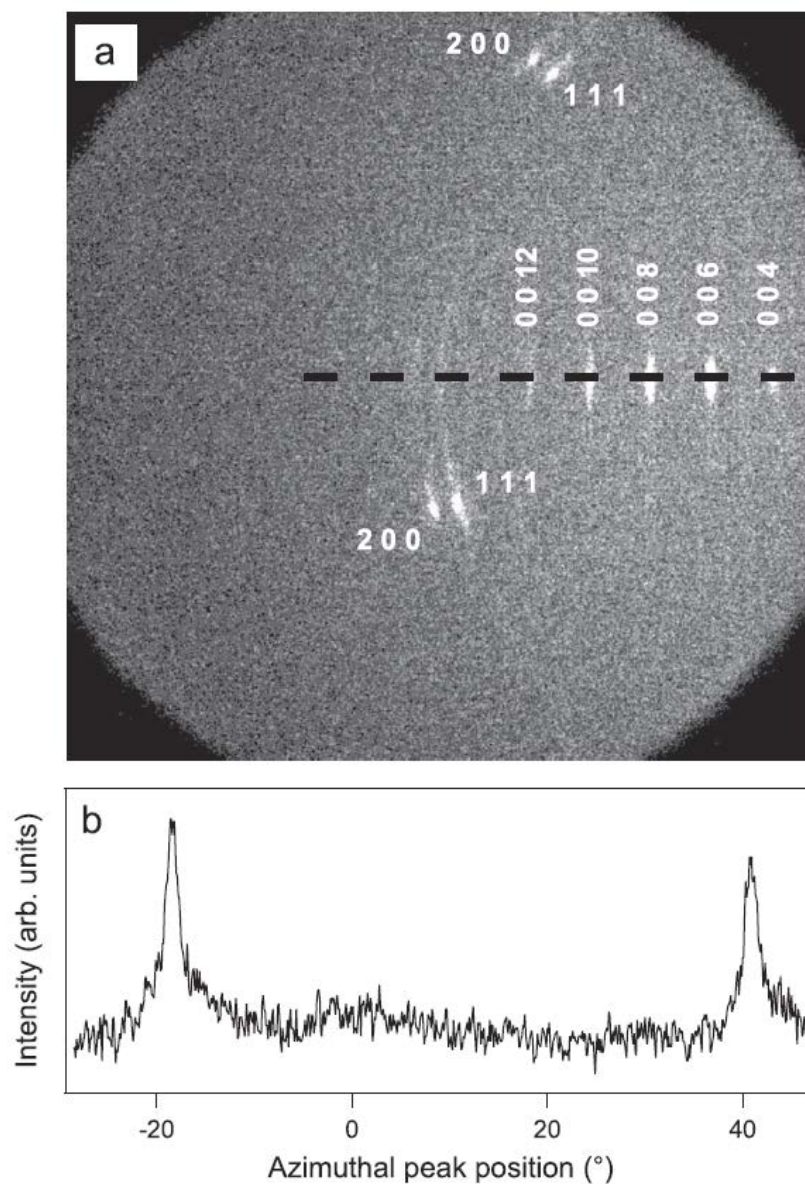


Figure 3.4 2D X-ray diffraction result in twinned phase (a) Peaks observed on area detector. Note the horizontal series of peaks corresponding to $002n$ reflections and the pairs of spots corresponding to peaks at values of 2θ between 20° and 25° (see Fig. 3.2) (b) Integrated intensity for 2θ between 20° and 25° as a function of azimuthal angle ϕ . The two peaks correspond to spots below and above the horizontal axis ($\phi = 0$), respectively. Note that the peaks labelled 111 and 200 are likely due to mixture of reflections as explained in the text.

3.4.3 Crystal Structure of the Monoclinic R_V Phase

Although the micro X-ray diffraction data for the monoclinic phase does not allow us to completely determine its structure, the optical (and AFM) data of the twin domains provides important auxiliary data that allow us to complete the structural determination.

We begin our structural determination with the general formula for interplanar spacing d_{hkl} in a monoclinic structure, given the edge lengths a , b , c of the unit cell and the angle β between the edges of length a and c :

$$\frac{\sin^2 \beta}{d_{hkl}^2} = \frac{h^2}{a^2} + \frac{k^2 \sin^2 \beta}{b^2} + \frac{l^2}{c^2} - \frac{2hl \cos \beta}{ac}. \quad (1)$$

Because we measure three independent diffraction peaks, Eq. (1) provides three equations in the four unknown lattice parameters (a , b , c , and β), provided that the Miller indices for each peak are known. For the special case of $(0\ 0\ 2n)$ planes, the spacings are given by

$$\frac{\sin^2 \beta}{d_{002n}^2} = \frac{(2n)^2}{c^2}. \quad (2)$$

For the remaining two peaks, there are a number of possible sets of indices.

Given the assumptions that the structure at 315 K is monoclinic and that each stripe is bounded by a twin plane, as are domains of stripes, and that the c -axis is oriented vertically, the optical data provide an independent measure of angles between sets of twin planes. We can use either of the measured angles, assumed to be between the $[p\ q\ 0]$ and $[r\ s\ 0]$ directions *projected onto the horizontal focal plane* of the microscope (i.e., a plane perpendicular to the c axis), as a fourth equation. Explicitly, the measured angle θ should satisfy

$$\left(p^2 a^2 \sin^2 \beta + q^2 b^2\right)^{1/2} \left(r^2 a^2 \sin^2 \beta + s^2 b^2\right)^{1/2} \cos \theta = pr a^2 \sin^2 \beta + qs b^2. \quad (3)$$

Although the $0\ 0\ 2n$ peaks are readily identified by comparison with the diffraction patterns at lower temperatures, the indices h_1 , k_1 , l_1 , h_2 , k_2 , and l_2 for the other two peaks, and the direction indices p , q , r , and s of the stripes and twin boundaries are *a priori* unknown. If we assume that the structure is similar

to those of the O_{dci} structure at lower temperatures and the R_I structure at higher temperatures, we can guess that the two peaks correspond to 1 1 1 and 2 0 0 reflections and that the angle $\theta = 116^\circ/2$ corresponding to twin boundary 1 is between the horizontal projections of the [1 1 0] and [0 1 0] directions. Nevertheless, we tested every possible index with values ranging from 0 to 4 for self-consistency before accepting these numbers. With this indexing of the X-ray and optical data, we algebraically determine the lattice parameters of the R_V structure to be $a = 7.93 \pm 0.37 \text{ \AA}$, $b = 4.94 \pm 0.11 \text{ \AA}$, $c = 62.6 \pm 1.5 \text{ \AA}$, and $\beta = 86 \pm 14^\circ$, where the uncertainties are estimated from the peak widths of the diffraction data and the uncertainty in stripe angles.

As a consistency check, we note that the second observed twin angle of $57^\circ/2 = 28.5^\circ$ between the stripes and twin boundary 2 matches very closely the angle between the directions [0 1 0] and [1 3 0] (again projected onto a horizontal plane), which is predicted to be 29.9° , given our lattice parameters. Since this angle was not used in our structural determination, the fact that it corresponds to a crystallographic angle between two small-index directions provides good evidence that the Bragg peaks and direction of twin boundary 1 were indexed correctly.

Because the [0 1 0] direction is common to the crystallographic angles that both twin boundaries 1 and 2 make with the stripes (see Fig. 3.1), we identify [0 1 0] as the stripe direction. The stripes then have a very simple interpretation as ridges aligned along the [0 1 0] directions and terminated on their top surfaces by (0 0 1) planes, with (1 0 0) twin planes occurring at the center of each peak and valley. The inclination of the ridges is then simply the inclination of the monoclinic unit cell (provided that the lattice is unstrained, at least for the free surface). For the lattice parameters determined above, one would expect the slopes to then have an angle of 4° , which is close to the measured angle of $\sim 8^\circ$. In this picture, twin boundaries 1 and 2 are identified as (1 1 0) and (1 3 0) twin planes, respectively.

It is noteworthy that since β is close to 90° , Bragg peaks from $(h k l)$ planes will lie very close to peaks from $(h k \bar{l})$ planes. Moreover, the large value of c relative to a and b results in only small differences in plane spacing for variations in l . Thus the peak identified as 1 1 1 in Fig. 3.2 is probably a combination of several Bragg reflections including 1 1 1, $1 1 \bar{1}$, 1 1 3, and $1 1 \bar{3}$, all of which are expected to be detected at values of 2θ over a range of 0.5° (using the lattice parameters estimated above). Similarly, the peak nominally labeled 2 0 0 likely also contains $1 1 5$, $\bar{1} 1 1$, 2 0 2, and $\bar{2} 0 2$ reflections,

which are expected to span a 0.6° range. We did not take this into account in our analysis, but it is expected to result in only small differences.

With the structure of the R_V phase solved, the lattice parameters for each of the tricosane polymorphs studied can be compiled in Table VIII, along with the lattice structures, unit-cell volumes, and calculated densities.

The predicted unit-cell volume for the monoclinic R_V phase is $V_{RV} = abc \sin\beta = 2450 \pm 140 \text{ \AA}^3$, which implies a density of $0.88 \pm 0.05 \text{ g/cm}^3$. This density is the same as that of the R_{II} phase lying at slightly higher temperatures. We will see in the next section that the similarity between the structures and the small volume change have important consequences to the transition dynamics.

3.4.4 Phase Transition Dynamics

All of the transitions between polymorphs are easily visible via optical microscopy. In the case of large crystals prepared via slow cooling, a front can usually be seen sweeping across the sample during the phase transition, which in most cases results in a change in the shape and position of crystalline domains. The transition between the R_V and R_I rotator phases differs in this regard: no change in the overall domain structure is seen. The difference between the polymorphs is then signaled optically only by the presence or absence of stripes.

A closer look at the striped pattern reveals that their details are preserved through repeated cycles between the R_V and R_I phases. Figure 3.5 shows a series of images of a single region of a sample as it is cycled twice between temperatures of 314 K and 316 K (parts a–e). The *same* stripe pattern is seen in all three occurrences of the R_V phase. In Fig. 3.5f, a larger temperature excursion has brought the sample into the R_{II} phase. It is immediately evident that the domain structure has changed. Upon cooling back to the R_V phase (Fig. 3.5g), stripes again appear, but in an entirely new arrangement.

Moreover, AFM imaging during the R_V – R_I transitions reveal that atomic-scale features, such as monomolecular steps, are preserved throughout the transition. Figure 3.6 shows AFM tapping mode phase images of a small region of the crystal in the (a) the R_V and (b) R_I phases. In this case, several steps with heights comparable to that of the unit cell are visible with virtually the same arrangement with and without, respectively, a superimposed stripe pattern.

The reproducibility of molecular-scale features during the R_V – R_I transitions is indicative of a diffusionless transition, which occurs by local rearrangement of molecules rather than large scale motion (recall the nearly identical densities of the two phases). The interesting properties of this transition have been previously suggested by Sirota et al.¹⁹, who referred to it as essentially second-order and observed no sharp change in lattice parameters, and by Mondieig et al.²⁰, who proposed that it was a martensitic-like, diffusionless transition. To our knowledge, ours is the first imaging study of tricosane transitions to verify the martensitic nature of the R_V – R_I transition, though Nozaki and Hikosaka previously reported a wrinkled morphology for C_{25} ¹⁰. We have also performed preliminary optical imaging of C_{25} crystals (appendix A), and observe a twinned pattern similar to that seen for C_{23} . Although the domains are typically smaller and less organized, the same motifs—striped domains separated by two varieties of twin boundary—are clearly seen.

Naturally, raising the temperature above that of the orthorhombic R_I phase to reach the hexagonal R_{II} phase breaks the crystal symmetry, forcing a marked molecular reorganization that does not preserve microscopic features (see Fig. 3.5f–g). Cooling from the R_V phase to the O_{dci} orthorhombic phase does not change the basic symmetry of the crystalline lattice. However, this is *not* a diffusionless transition: there is a relatively large density change and a clear front is seen, and heating back to the R_V phase again results in a new pattern of stripes.

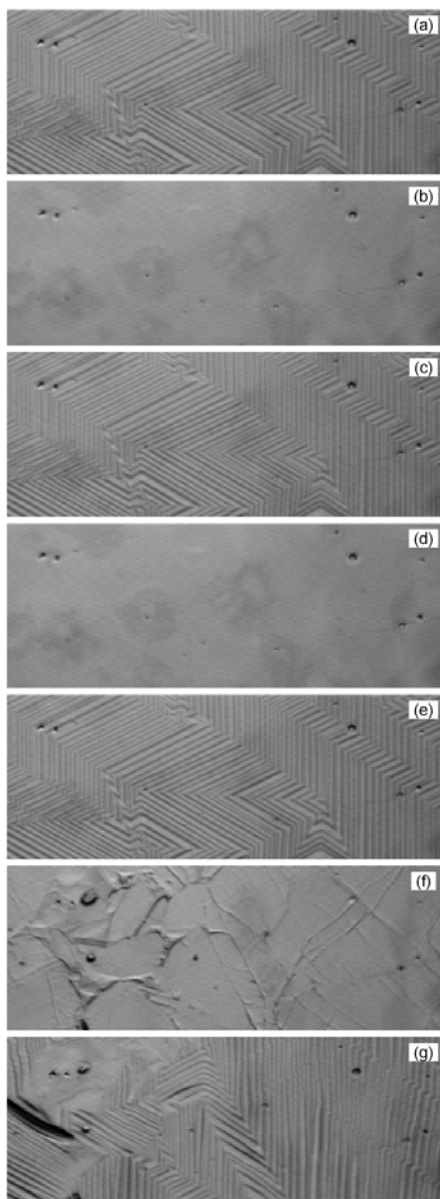


Figure 3.5 Sequence of optical microscopy images of a single region of a tricosane sample as the temperature is varied. Cycling from the monoclinic R_V phase (a) to the orthorhombic R_I phase (b) and back to the R_V phase (c) results in only minor changes to the striped pattern, as does an additional cycle (d,e). Raising the temperature further to enter the hexagonal R_{II} phase (f) results in a change in the domain structure, as evidenced by the significantly altered pattern of stripes upon return to the R_V phase (g). Each image spans a horizontal width of 170 μm .

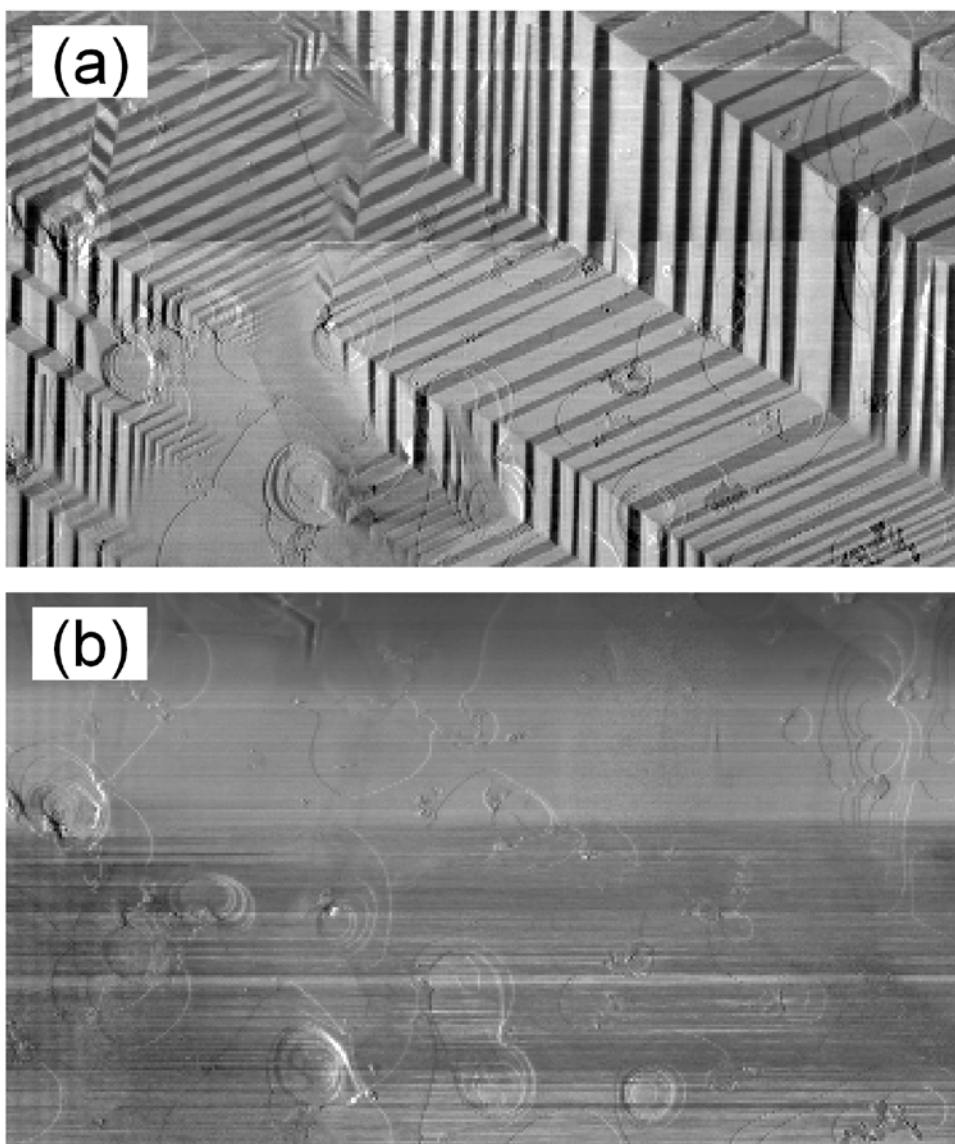


Figure 3.6 AFM tapping mode images during transition from R_V – R_I phase, showing no change in the molecular features. Each images spans a $20 \times 30 \mu\text{m}^2$ area. (Image courtesy of Eric Karhu.)

3.4.5 Conceptual Model for the Twinned Phase

The phenomenon of twinning has been well studied for many materials and crystallographic systems. In most cases of alternating twin “stripes,” it is experimentally observed that the twin-boundary spacing is somewhat constant for a particular system, though it may vary with the size of the twinned grain (see, e.g.,²¹ for examples). This behavior is typically modeled as resulting from a competition between the interfacial energy of the twin boundaries and elastic energy, which favor wide and narrow stripes, respectively. A common case in the martensite literature is the formation of a twinned phase in an untwinned parent phase. Modeling the elastic energy in the parent phase yields the prediction that the stripe spacing λ should scale as the square root of the size of the twinned domain²².

In our case, with a single-component system, only one phase is thermodynamically stable, and the entire sample is twinned (aside from occasional small regions). We propose that mechanical strain in this case accommodates a free (0 0 1) surface at an inclination determined by the monoclinic unit cell while the bottom of the crystal, which also inherits a (0 0 1) orientation from its origins in the orthorhombic R_f phase, is constrained by the substrate to lie perpendicular to the vertical c axis, as shown in Fig. 3.7. The strain then varies linearly across the ridge (i.e., along the x direction in Fig. 3.7), so that the elastic energy density varies quadratically. The integrated elastic energy of each trapezoidal domain is then proportional to $E\lambda^3/h$, where E is the Young’s modulus along the c axis and h is the average thickness of the domains:

$$E_{trap} = E \frac{v}{h} \int_{-\lambda/4}^{\lambda/4} \left(\int_0^{x \tan \alpha} y dy \right) dx = \frac{1}{192} E \frac{v \tan^2 \alpha}{h} \lambda^3, \quad (4)$$

where v is the length of the ridge in the z direction and $\alpha = 90^\circ - \beta \approx 7^\circ$ is the inclination of the ridge. Note that each trapezoid corresponds to half of a ridge, and that strain energy is minimized if the center of a trapezoid is unstrained, with a maximum strain of $\lambda \tan \alpha / 4h$ at either end. As a result, the total elastic energy for a region of extent w along the x axis (and extent v along the z direction), which contains $2w/\lambda$ trapezoidal domains, scales as $Ew\lambda^2/h$. Explicitly,

$$E_{strain} = \frac{1}{96} E \frac{w v \tan^2 \alpha}{h} \lambda^2. \quad (5)$$

If each twin boundary has an interfacial energy (per area) of γ , the energy per unit length along the z axis of $2w/\lambda$ boundaries is $2\gamma wh/\lambda$. Energy minimization then suggests that

$$\lambda^3 = \frac{96h^2 \gamma}{\tan^2 \alpha E}. \quad (6)$$

For our crystals, with typical values of $h \approx 20 \mu\text{m}$ and $\lambda \approx 1 \mu\text{m}$, we predict $\gamma/E \approx 4 \times 10^{-13} \text{ m}$. Lack of data on both the twin-plane energy and elastic moduli of the R_V phase of tricosane makes verification of Eq. 5 difficult, but we note that the energy cost of a twin boundary is likely to be rather small (i.e., on the order of 1 mN/m) for these van der Waals solids, while the stiffness along the axis of the alkane molecules would be expected to be quite large (i.e., $> 1 \text{ GPa}$). (Detailed calculations are presented in Appendix B.)

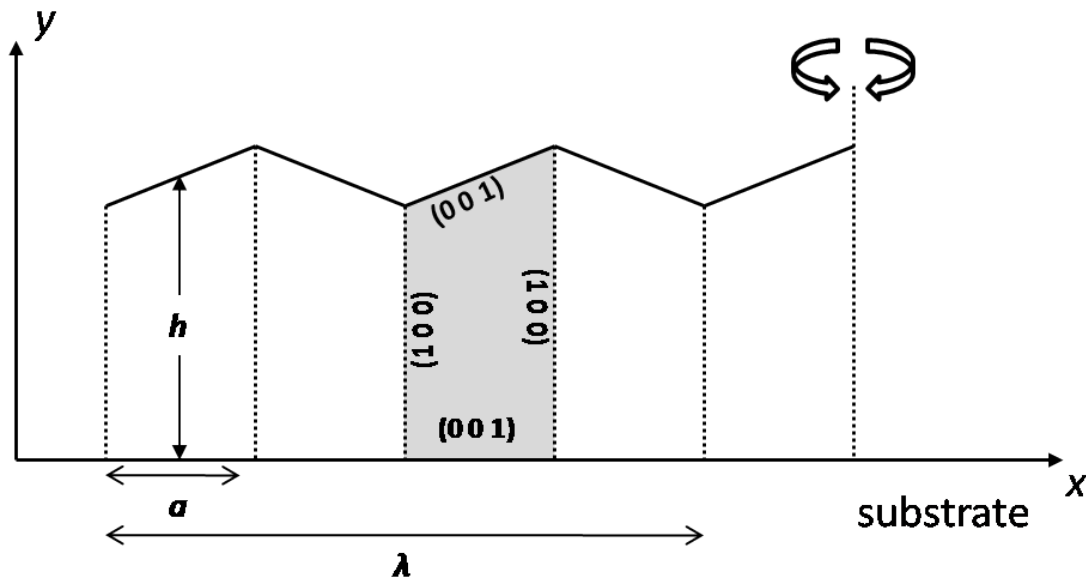


Figure 3.7 Illustration showing a cross-section of a twinned region perpendicular to the ridges, with twin axes (dotted lines) and crystal surfaces (solid lines) identified for a single domain (shaded region).

3.5 Conclusion

We have performed a study of the polymorphs exhibited by tricosane, $C_{23}H_{48}$, which has a rich phase diagram containing at least five solid phases, three of which are so-called “rotator phases” characterized by positional order without long-range orientational order. Our particular interest is in the solid-solid transitions between the polymorphs, which are identified by X-ray diffraction but can be observed via optical microscopy. Most of the transitions are clear first-order transitions, which proceed with a growth front and result in significant changes in the crystalline lattice and unit-cell volume.

One of the transitions, that between the monoclinic R_V and orthorhombic R_I rotator phases, is diffusionless. Optical and atomic-force microscope imaging reveals that the R_V structure is highly twinned, exhibiting a striking arrangement of ridges arranged in domains bounded by two types of twin planes. We have shown that the transition from the R_V phase to and from the R_I phase preserves both the macroscopic domain structure on length scales of 10s of μm , and microscopic molecular features on nm scales, made possible by the very similar densities of the two phases. We propose that the twinning is the result of a monoclinic structure constrained such that it is bounded below by a flat substrate and is oriented with a vertical c -axis due to the presence of surrounding domains. The mechanical strain caused by the constraints is relieved by quasi-periodic twin boundaries that allow the free top surface to be approximately horizontal.

The features of the R_V polymorph and its transitions are reminiscent of martensitic transformations, which are more familiar in metal alloys. The tricosane system may thus be a convenient model for martensitic transitions: Because tricosane is a weakly-bound van der Waals solid, the transition occurs at convenient temperatures, and because the tricosane molecules are large relative to metal atoms, the transitions are slow enough to be easily studied.

Table III Principal Bragg peaks observed for the orthorhombic phase at 34 °C. The planes are indexed for consistency with the phase sequence for tricosane proposed in Ref. 9.

Peak location (2θ)	Planar separation, d (Å)	Miller indices ($h k l$)
8.59	10.29	(0 0 6)
11.39	7.76	(0 0 8)
14.24	6.21	(0 0 10)
17.13	5.17	(0 0 12)
20.03	4.43	(0 0 14)
21.53	4.12	(1 1 0)
22.93	3.87	(0 0 16)
23.80	3.74	(0 2 0)

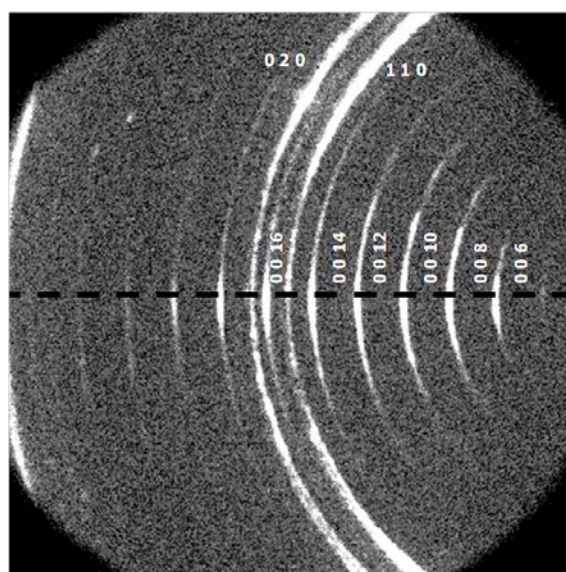


Figure 3.8 Principal Bragg peaks observed for the orthorhombic phase at 34 °C.

Table IV Principal Bragg peaks observed for the orthorhombic phase at 38 °C. The planes are indexed for consistency with the phase sequence for tricosane proposed in Ref. 9.

Peak location (2θ)	Planar separation, d (Å)	Miller indices ($h k l$)
8.59	10.28	(0 0 6)
11.40	7.76	(0 0 8)
14.25	6.21	(0 0 10)
17.12	5.17	(0 0 12)
21.47	4.13	(1 1 1)
21.95	4.04	(1 1 3)
22.70	3.91	(1 1 5)
24.40	3.65	(2 0 3)

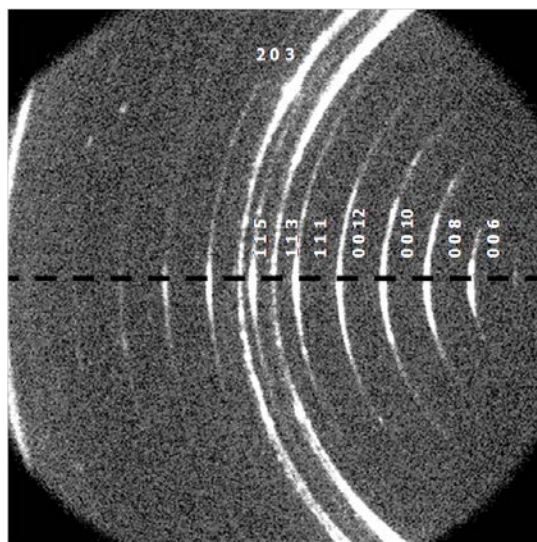


Figure 3.9 Principal Bragg peaks observed for the orthorhombic phase at 38 °C.

Table V Principal Bragg peaks observed for the monoclinic rotator phase at 41 °C. The planes are indexed for consistency with the phase sequence for tricosane proposed in Ref. 9.

Peak location (2θ)	Planar separation, d (Å)	Miller indices ($h k l$)
8.51	10.37	(0 0 6)
11.35	7.79	(0 0 8)
14.18	6.24	(0 0 10)
17.03	5.20	(0 0 12)
21.28	4.17	(1 1 1)
22.46	3.96	(2 0 0)

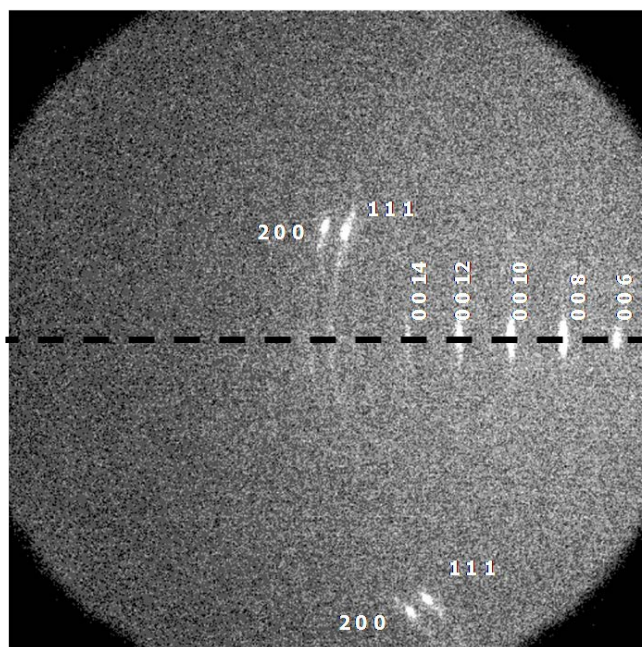


Figure 3.10 Principal Bragg peaks observed for the monoclinic rotator phase at 41 °C.

Table VI Principal Bragg peaks observed for the orthorhombic rotator phase at 43 °C. The planes are indexed for consistency with the phase sequence for tricosane proposed in Ref. 9.

Peak location (2θ)	Planar separation, d (Å)	Miller indices ($h k l$)
8.49	10.40	(0 0 6)
11.27	7.78	(0 0 8)
14.12	6.27	(0 0 10)
21.42	4.17	(1 1 1)
22.00	3.96	(0 2 0)

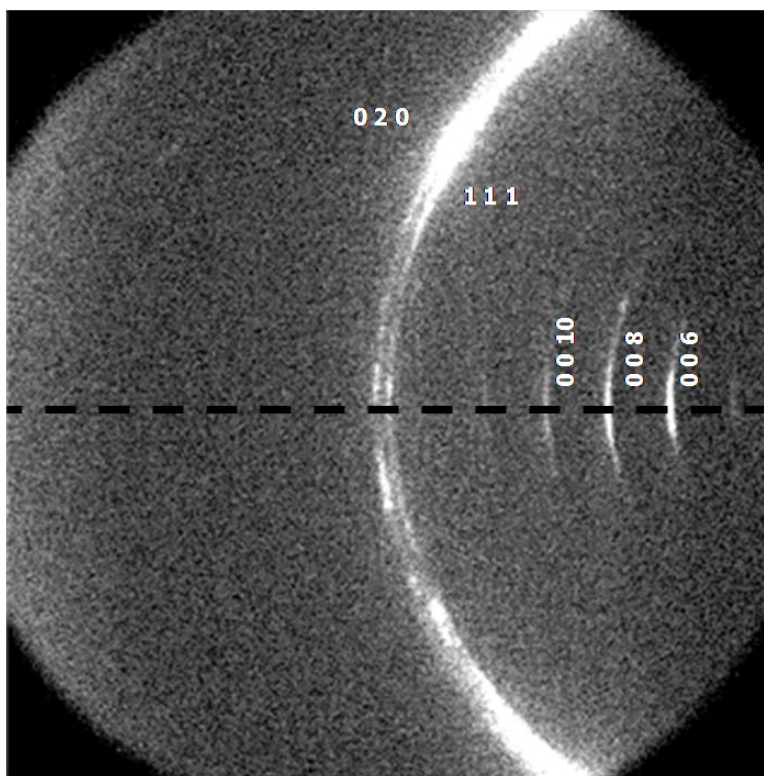


Figure 3.11 Principal Bragg peaks observed for the orthorhombic rotator phase at 43 °C.

Table VII Principal Bragg peaks observed for the hexagonal rotator phase at 46 °C. The planes are indexed for consistency with the phase sequence for tricosane proposed in Ref. 9.

Peak location (2θ)	Planar separation, d (Å)	Miller indices ($h k l$)
8.47	10.43	(0 0 9)
11.29	7.83	(0 0 12)
14.06	6.29	(0 0 15)
21.51	4.13	(1 0 1)

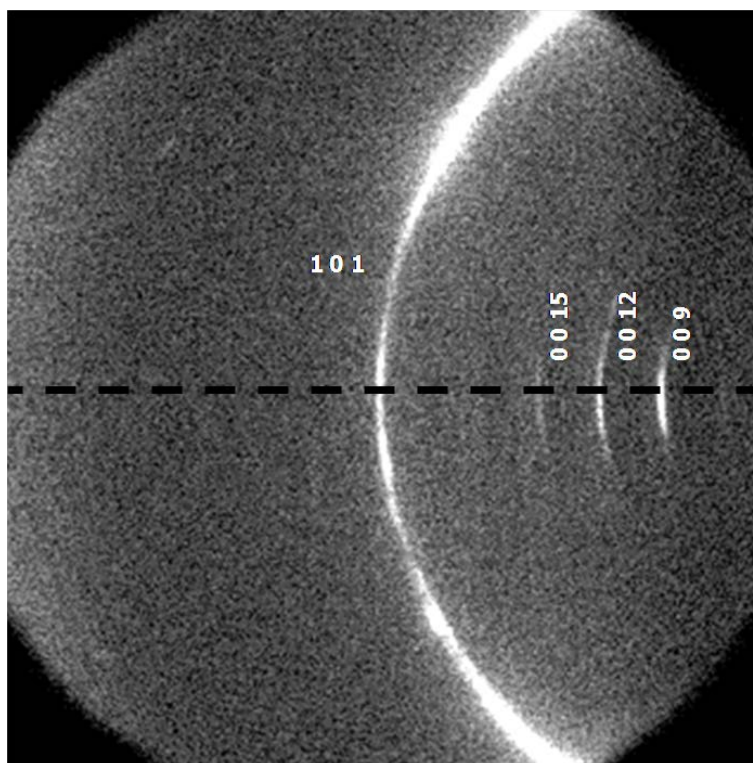


Figure 3.12 Principal Bragg peaks observed for the hexagonal rotator phase at 46 °C.

Table VIII Lattice parameters and properties for the five polymorphs of tricosane studied in this work (estimated standard deviations are indicated in parentheses).

Phase	Structure	Space group (number)	a (Å)	b (Å)	c (Å)	β (°)	Volume (Å ³)	Z (#/cell)	Density (g/cm ³)
O_i	orthorhombic	$Pcam$ (57)	7.472(8)	4.945(8)	62.02(4)	—	2292(5)	4	0.941(2)
O_{dc}	orthorhombic	$Pnam$ (62)	7.419(15)	4.980(10)	62.05(11)	—	2292(8)	4	0.940(3)
R_V	monoclinic	Aa (9)	7.93(49)	4.94(11)	62.6(15)	86(14)	2450(140)	4	0.88(5)
R_I	orthorhombic	$Fmmm$ (69)	8.074(8)	4.843(7)	62.63(5)	—	2449(5)	4	0.880(2)
R_{II}	hexagonal	$R3m$ (166)	4.769(7)	—	94.14(16)	—	1854(4)	3	0.872(2)

3.6 Bibliography for Chapter 3

- 1 G. A. Holder and J. Winkler, "Crystal-Growth Poisoning of n-Paraffin Wax By Polymeric Additives and its Relevance to Polymer Crystallization Mechanisms," *Nature* **207** (4998), 719-721 (1965).
- 2 S. R. Reddy, "Increasing the Responsiveness of No. 2-D Diesel Fuels to Flow Improvers by Blending with Low Wax Diluents," *Society of Automotive Engineers Technical Paper* **841351**, 5922 (1985).
- 3 A. E. Smith, "The Crystal Structure of the Normal Paraffin Hydrocarbons," *Journal of Chemical Physics* **21** (12), 2229-2231 (1953).
- 4 E. B. Sirota, H. E. King, D. M. Singer, and H. H. Shao, "Rotator Phases of the Normal Alkanes - an X-Ray-Scattering Study," *Journal of Chemical Physics* **98** (7), 5809-5824 (1993).
- 5 G. Ungar, "Structure of Rotator Phases in Normal-Alkanes," *Journal of Physical Chemistry* **87** (4), 689-695 (1983).

- 6 B. M. Craven, Y. Lange, G. G. Shipley, and J. Steiner, *Handbook of Lipid Research*, Vol. 4, D. M. Small (Ed.), (Plenum Press, New York, 1986).
- 7 E. B. Sirota, "Supercooling and transient phase induced nucleation in n-alkane solutions," *Journal of Chemical Physics* **112** (1), 492-500 (2000).
- 8 A. Muller, "An X-Ray Investigation of Normal Paraffins Near Their Melting Points," *Proceedings of the Royal Society of London. Series A* **138** (836), 514-530 (1932).
- 9 L. Robles, D. Mondieig, Y. Haget, and M. A. Cuevas-Diarte, "Review on the energetic and crystallographic behaviour of n-alkanes. II. Series from C₂₂H₄₆ to C₂₇H₅₆," *Journal De Chimie Physique Et De Physico-Chimie Biologique* **95** (1), 92-111 (1998).
- 10 K. Nozaki and M. Hikosaka, "Mechanism of primary nucleation and origin of hysteresis in the rotator phase transition of an odd n-alkane," *Journal of Materials Science* **35** (5), 1239-1252 (2000).
- 11 F. Rajabalee, V. Metivaud, D. Mondieig, Y. Haget, and M. A. Cuevas-Diarte, "New insights on the crystalline forms in binary systems of n-alkanes: Characterization of the solid ordered phases in the phase diagram tricosane plus pentacosane," *Journal of Materials Research* **14** (6), 2644-2654 (1999).
- 12 H. Nouar, D. Petitjean, M. Bouroukba, and M. Dirand, "Binary phase diagram of the system: n-docosane-n-tricosane," *Journal of Molecular Structure* **443** (1-3), 197-204 (1998).
- 13 J. L. Hutter, S. Hudson, C. Smith, A. Tetervak, and J. Zhang, "Banded crystallization of tricosane in the presence of kinetic inhibitors during directional solidification," *Journal of Crystal Growth* **273** (1-2), 292-302 (2004).
- 14 C. Merkl, T. Pfohl, and H. Riegler, "Influence of the Molecular Ordering on the Wetting of SiO₂/Air Interfaces by Alkanes," *Physical Review Letters* **79** (23), 4625 (1997).
- 15 R. L. Flemming, "Micro X-ray diffraction (μXRD): a versatile technique for characterization of earth and planetary materials," *Canadian Journal of Earth Sciences* **44** (9), 1333-1346 (2007).
- 16 D. E. Appleman and H. T. Evans, Jr., "Indexing and least-squares refinement of powder diffraction data," in *US Nat. Tech. Information Service, Doc. PB 216* (NTIS, 1973).
- 17 A. R. Gerson and S. C. Nyburg, "A twinned structure for n-tetracosane," *Acta Crystallographica Section B* **48** (5), 737-741 (1992).

- 18 T. Asano, M. F. Mina, and I. Hatta, "Twin formation mechanism in the solid-solid phase transition of normal hexatriacontane (n-C₃₆H₇₄)," *Journal of the Physical Society of Japan* **65** (6), 1699-1704 (1996).
- 19 E. B. Sirota, H. E. King, Jr., Henry H. Shao, and D. M. Singer, "Rotator Phases in Mixtures of n-Alkanes," *The Journal of Physical Chemistry* **99** (2), 798-804 (1995).
- 20 D. Mondieig, V. Metivaud, H. A. J. Oonk, and M. A. Cuevas-Diarte, "Isothermal Transformations in Alkane Alloys," *Chemistry of Materials* **15** (13), 2552-2560 (2003).
- 21 K. Bhattacharya, *Microstructure of Martensite* (Oxford University Press, 2003)
- 22 G. R. Barsch, B. Horovitz, and J. A. Krumhansl, "Dynamics of twin boundaries in martensites," *Physical Review Letters* **59** (11), 1251 (1987).

Chapter 4: Reversible Inhibition of Calcium Oxalate Monohydrate Growth by an Osteopontin Phosphopeptide

4.1 Introduction

Calcium oxalate monohydrate ($\text{CaC}_2\text{O}_4 \cdot \text{H}_2\text{O}$, hereafter referred to as COM) is the majority component of kidney stones, which afflict more than 10% of the population at some point in their lives¹. It has long been known that certain natural proteins, e.g., osteopontin (OPN), alter the morphology of COM crystals and decrease their growth rate^{2,3,4}. More recently, it has been found that certain synthetic polypeptides, e.g., poly(aspartic acid), can also affect COM crystallization^{5,6,7}. The low concentration of such proteins and polypeptides required for effective inhibition suggests a mechanism involving surface modification, as opposed to bulk effects (e.g., the well-known melting-point depression).

One mechanism by which surface effects can influence crystal growth was proposed more than 50 years ago by Cabrera and Vermilyea⁸. In the “C-V model,” Cabrera and Vermilyea argued that a molecule strongly adsorbed to a growth surface can pin advancing growth steps. For growth to continue through a “fence” of such impurities, the steps must curve around the pinning sites, as shown in figure 4.1, reducing the effective supersaturation via the Gibbs-Thomson effect.

This results in two possibilities: either the step can pass around the pinning site, allowing growth to proceed, albeit at a slower rate due to the reduced effective supersaturation, or the curvature required for growth to proceed is enough to reduce the effective supersaturation to zero, arresting growth altogether. The latter will be the case if the spacing between pinning sites is smaller than the critical radius r^* for two-dimensional nucleation on the growth surface. This reduction in growth rate without a change in the thermodynamic phase diagram has led to the term “kinetic inhibition.”

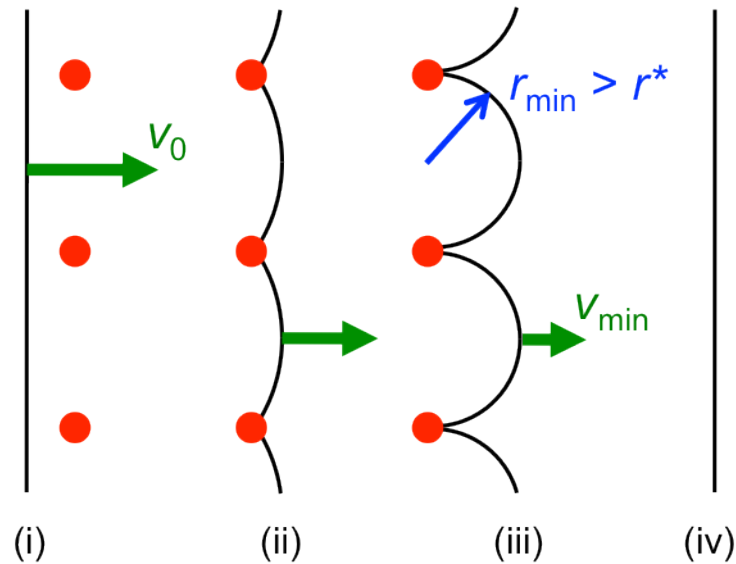


Figure 4.1 Cabrera and Vermilyea’s step-pinning model. Step (i) (vertical black line) propagating at speed v_0 is about to encounter a “fence” of adsorbed impurities (red dots). Step (ii) has been pinned by a fence of impurities, resulting in curvature and a lower propagation speed. A minimum radius of curvature larger than the two-dimensional critical nucleus will allow step (iii) to pass beyond the impurities. Step (iii) has passed through the impurities and has regained its original propagation speed.

The C-V model has been invoked to explain a number of crystallization phenomena in both natural and commercially important systems. For example, the ability of certain species of arctic fish to survive temperatures lower than the melting point of their blood has been ascribed to natural antifreeze glycoproteins that quickly bind to any ice nuclei that form⁹. The petroleum industry has been active in developing polymeric additives to prevent the precipitation of alkanes from diesel fuels¹⁰ and clathrate hydrates in natural-gas production pipelines¹¹. In these cases, a clear hysteresis is observed: the melting (or dissolution) point of the crystals is unaltered, but growth only proceeds above a threshold supersaturation that is dependent on the inhibitor concentration, as would be expected for the C-V mechanism. The range of supersaturations for which no growth is observed despite being thermodynamically favorable has been termed the supersaturation “dead zone.”

Direct microscopic evidence for the C-V model has been demonstrated only recently. A number of atomic force microscopy studies have now shown a transition from relatively straight growth steps to a

cusped form reminiscent of Fig. 4.1. Perhaps the most convincing example is the work by De Yoreo et al., who imaged the progress of a step past a single inhibitor molecule on a COM growth surface¹². A number of groups have been studying this system, both because of its medical significance and because it is well suited to studies of kinetic inhibition in general^{13,14,15}.

Despite the qualitative success of the C-V model, some questions remain. A number of authors have pointed out an apparent contradiction between the requirement of immobile pinning sites and the observed sensitivity of the inhibition to the concentration of inhibitor molecules in solution. One would expect that the strong adsorption required for an inhibitor molecule to block step flow for an appreciable time would result in irreversible adsorption, whereas the dependence of its effectiveness on inhibitor concentration suggests a surface coverage governed by an equilibrium isotherm resulting from a balance between adsorption and desorption to the surface. This shortcoming has been addressed in various ways in the literature.

Anklam et al.¹⁶ proposed an alternative model for crystal-growth inhibition that does not require strong adsorption. In their model, equilibrium coverage of inhibitor molecules lowers the surface energy of crystal faces. For crystallization to proceed, new surface regions must be created, either by nucleation of a new layer or the advance of a growth step to extend a terrace. If adsorption of inhibitor molecules is slow relative to the creation of new surface, a crystal with a temporarily higher surface energy is created, reducing the effective supersaturation and slowing growth. A major weakness of this model is that it implies that an “inhibited” crystal will grow more rapidly than will a crystal with no inhibitor present. Although there are cases where additives promote nucleation or result in seemingly rapid growth, this is a characteristic of neither kinetic inhibitors in general nor of the specific case studied here.

De Yoreo et al. have relaxed the requirement of strong adsorption by modifying the standard C-V model to include a finite lifetime of inhibitor molecules on growth terraces¹⁷. They found that the resulting reversible pinning could still account for observed aspects of inhibition such as a supersaturation dead zone. In this picture, the ratio of the lifetime of an inhibitor molecule on a growth terrace to the time required for an advancing step to cover the terrace is a critical parameter in the inhibition process.

De Yoreo et al. have also pointed out that inhibition via the Gibbs-Thomson effect may not be the dominant mechanism in all cases. In some cases, e.g., crystallization from low-solubility salts such as calcite (calcium carbonate) and potassium dihydrogen phosphate (KDP), the kink-site density on growth steps can be low enough that one-dimensional nucleation on otherwise straight steps is the rate-limiting step for step propagation. In such case, inhibitors that bind to kink sites can have a profound effect on crystallization rates. To support this idea, they offer Monte-Carlo simulation results that show a saturation dead zone similar to that expected by the C-V model, but a dependence on impurity concentration which shows little change for low levels of impurity followed by a rapid decrease to the fully arrested state¹⁸.

Understanding the details of the inhibition mechanism is important to the development of new additives for commercial and medical applications, and to modeling their effectiveness. One way to probe the details of the inhibitor-crystal interaction is to examine the recovery of growth surfaces from an inhibited state. For instance, one can increase the supersaturation during growth in the presence of inhibitors. According to the C-V model, this will decrease the critical radius, allowing steps to squeeze between pinning sites.

Land et al.¹⁹ used in-situ atomic force microscopy to investigate the growth of inhibited KDP {100} surfaces as they emerge from the supersaturation dead zone. They observed that growth resumed by the propagation of macrosteps (i.e., growth steps with a height of several unit cells), suggesting that the C-V model, which considers only elementary steps, is too simplistic. In this case, elementary steps remained pinned until incorporated by advancing macrosteps. In a similar study, Ristic et al.²⁰ found that poisoned steps on {110} faces of the pharmaceutical paracetamol remained immobile when the supersaturation increased, with crystallization eventually resuming by the nucleation of new macrosteps at distant (i.e., unobserved) locations. Both of these studies are consistent with nearly irreversible inhibitor adsorption, with impurities presumably incorporated in the crystal when growth resumes.

We have been studying the effects of synthetic OPN-based peptides on the growth of COM in order to determine the peptide sequences most effective at blocking COM growth. In particular, our study focuses on the phosphorylated peptide sequence pSHDHMDDDDDDDDGD corresponding to amino acids 65–80 of rat-bone OPN, which we term pOPAR. We have used fluorescence microscopy of AlexaFluor-labelled pOPAR (i.e., a fluorescently labelled pOPAR peptide) to demonstrate adsorption

of pOPAR to all growth faces of COM crystals²¹, and scanning electron microscopy (SEM) to image the resulting morphological changes²². Our observations are that pOPAR induces scalloping of the growth steps, as is expected from the C-V mechanism. Measurements of the change in overall crystal aspect ratio suggest that the largest effect is on the $\{100\}$ faces, while the $\{010\}$ faces are least inhibited (see Figure 4.2 for a schematic of the overall crystal morphology and step structures proposed for the three principal growth faces). This observation is corroborated by molecular dynamics simulations that predict a faster adsorption of pOPAR to $\{100\}$ faces than to $\{010\}$ faces²¹.

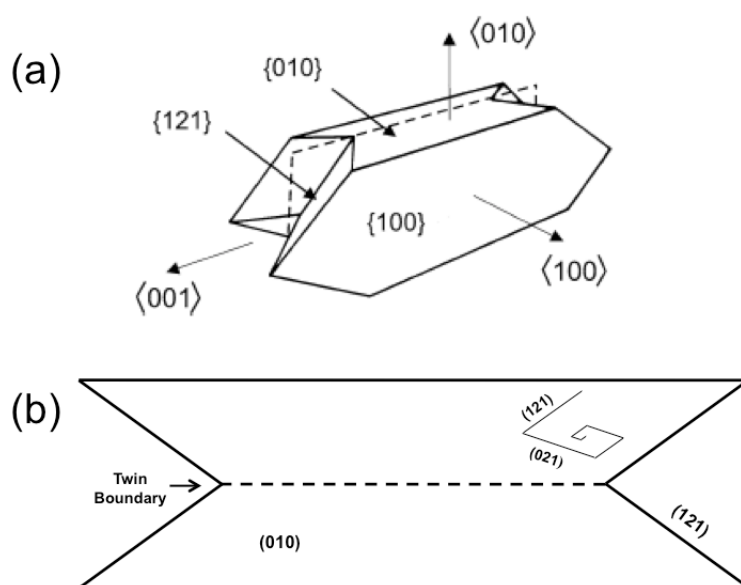


Figure 4.2 Schematic of a typical COM crystal showing (a) the three principal families of growth faces: $\{100\}$, $\{010\}$, and $\{121\}$, and associated growth directions, and (b) the structure of a growth hillock on a (010) growth face (top view). The steps comprising the growth spiral are indicated in terms of the “step risers” indicated

In this chapter, I present an atomic force microscopy study of crystallization on the {010} faces of COM in the presence of pOPAR. We find that pOPAR has a strong effect on both step morphology and propagation speed, even at low concentration. Introduction and subsequent removal of pOPAR during growth provides insight into the inhibitor mechanism and allows us to address the question of the ultimate fate of the inhibitor molecules.

4.2 Materials and Methods

For all experiments, reagent-grade sodium oxalate ($\text{Na}_2\text{C}_2\text{O}_4$), calcium nitrate ($\text{Ca}(\text{NO}_3)_2 \cdot 4\text{H}_2\text{O}$), sodium chloride (NaCl), and sodium acetate (CH_3COONa , anhydrous) were used as purchased from Sigma-Aldrich, with no further purification. pOPAR was synthesized as previously described²³.

Deionized water purified with a Milli-Q water system was used for the preparation of all solutions. Two stock solutions were prepared for further dilution in all crystallization experiments: a calcium stock solution containing 5.88 mM calcium nitrate, and an oxalate stock solution containing 5.88 mM sodium oxalate. In addition, both solutions contained 0.4118 M sodium chloride and 0.0294 M sodium acetate.

Nucleation of COM crystals was carried out on microscope cover glasses (12 mm diameter; Erie Scientific) inserted into tissue culture plate wells (24-well, BD Canada). First, 170 μL oxalate stock was added to the wells, followed by 660 μL water and 170 μL calcium stock to arrive at final volume of 1000 ± 3 μL . This results in final concentrations of 1 mM for calcium and oxalate, 150 mM for sodium chloride, and 10 mM for sodium acetate, at a pH of 7.2 ± 0.2 .

After remaining in the nucleation solution overnight, the cover glasses were scraped with a metal spatula to suspend nucleated crystals in solution. The solutions were filtered through polycarbonate membrane filters with a 0.8 μm pore size (GE Healthcare/Whatman) placed inside a plastic Swinny filter holder (Pall Corp.). After drying in air, the membrane filter was brought into gentle contact with a glass sample substrate coated with a thin (a few μm or less) layer of partially-cured UV-curing adhesive (Norland Optical Adhesive NOA 81, Norland Products, Inc.) to transfer the crystals to the sample substrate. The adhesive was cured for 15 min to firmly affix the crystals for in-situ atomic force microscope (AFM) studies.

AFM height and deflection images were recorded using a Multimode AFM with Nanoscope IIIA controller (Digital Instruments) using a scanner with a maximum lateral motion of $\approx 12 \mu\text{m}$ and silicon nitride cantilevers (DNP-S, Veeco) with nominal spring constant of $\approx 0.06 \text{ N}\cdot\text{m}^{-1}$ and resonant frequency of $\approx 18 \text{ kHz}$. Imaging was performed in contact mode using a glass fluid cell (Digital Instruments) at ambient temperature (approximately $30 \text{ }^\circ\text{C}$ in the fluid cell) at scan rates of 2–27 Hz. Care was taken to use the smallest possible contact forces.

For in-situ crystallization experiments, the previously described calcium and oxalate stock solutions were mixed and diluted with deionized water to prepare growth solutions with calcium oxalate concentrations from 0.2 to 0.3 mM. This results in positive supersaturations, σ , defined as

$$\sigma = \frac{1}{2} \ln \left[\frac{a_{\text{Ca}^{2+}} a_{\text{C}_2\text{O}_4^{2-}}}{K_{\text{sp}}} \right], \quad (1)$$

where $a_{\text{Ca}^{2+}}$ and $a_{\text{C}_2\text{O}_4^{2-}}$ are the activities of calcium and oxalate ions, respectively, and $K_{\text{sp}} = 1.66 \times 10^{-9} \text{ M}^2$ is the solubility product²⁴. Because the growth solutions have moderately high ionic strength, we calculate the activities of the calcium and oxalate ions from their concentrations c_i as $a_i = \gamma_i c_i$ using activity coefficients γ_i estimated from Debye-Hückel theory²⁵. Growth solutions containing pOPAR were prepared in a similar manner, but the volume share of water was reduced in favor of appropriate volumes of pOPAR solution ($50 \mu\text{g}/\text{mL}$) to result in final pOPAR concentrations ranging from 0.05 to $1 \mu\text{g}/\text{mL}$ (26 nM to $0.52 \mu\text{M}$) in this study.

During imaging, the CaOx concentration will deplete due to growth of crystals. To prevent this, some researchers have used a continuous flow design to maintain a constant supersaturation²⁶. However, for our purposes it was necessary to rapidly exchange a pure growth solution with an inhibitor-containing solution, and vice versa. Therefore, we chose to image in static growth solutions, replenishing the solution in the AFM fluid cell every 5 min to maintain a relatively constant supersaturation (as adapted from Guo, et al.²⁷). Due to the low density of crystals in our samples, we estimate that the drop in supersaturation will be negligible in this interval, and observations confirm no noticeable decrease in growth rate. The expected decrease in supersaturation in the five-minute interval before the static growth solution is replenished can be estimated from our observations of the growth rate. Optical micrographs of a typical sample surface show ~ 20 crystals in a typical $200 \mu\text{m} \times 300 \mu\text{m}$ region. Each

crystal has a surface area of roughly $15 \mu\text{m} \times 5 \mu\text{m}$, so our samples present a COM surface area of $\sim 0.025 \mu\text{m}^2$ per μm^2 of substrate (i.e., 2.5% of the sample surface is comprised of crystal surface).

During growth, the typical normal growth rate R can be calculated from the step speed v_s , spacing λ , and height h as $R = v_s h / \lambda$. Using approximate values of $v_s = 1 \text{ nm/s}$, $\lambda = 50 \text{ nm}$, and $h = 0.5 \text{ nm}$, we find $R \approx 0.01 \text{ nm/s}$. Given a density of $\rho = 2.12 \text{ g/cm}^3$ and molecular weight of $W = 146 \text{ g/mol}$, the number of moles of calcium oxalate incorporated in the growing crystals per cm^2 of surface in 5 min is expected to be

$$(0.025 \text{ cm}^2) \left(10^{-9} \frac{\text{cm}}{\text{s}}\right) (300 \text{ s}) \left(2.12 \frac{\text{g}}{\text{cm}^3}\right) \left(\frac{1 \text{ mol}}{146 \text{ g}}\right) = 1.1 \times 10^{-10} \text{ mol.}$$

Assuming no convection, this calcium oxalate is supplied to the crystals by diffusion to the surface. Since the diffusivity of small ions in water is on the order of $10^{-5} \text{ cm}^2/\text{s}$, only ions within a distance

$$\ell = \sqrt{Dt} \approx 0.055 \text{ cm}$$

can reach the surface in 5 min. Given a growth-solution concentration of 0.3 mM, the amount of calcium oxalate within this distance of the surface is

$$(3 \times 10^{-4} \text{ mol/L}) \left(\frac{1 \text{ L}}{1000 \text{ cm}^3}\right) (0.055 \text{ cm}) = 1.6 \times 10^{-8} \text{ mol/cm}^2.$$

Thus, one would expect the solution concentration to drop by less than 1% before the solution is replenished. In practice, we expect additional transport by convection, further decreasing the depletion.

This estimate is consistent with the lack of change seen in step velocity over the 5 min period before the growth solution is replenished as shown in Fig. 4.3.

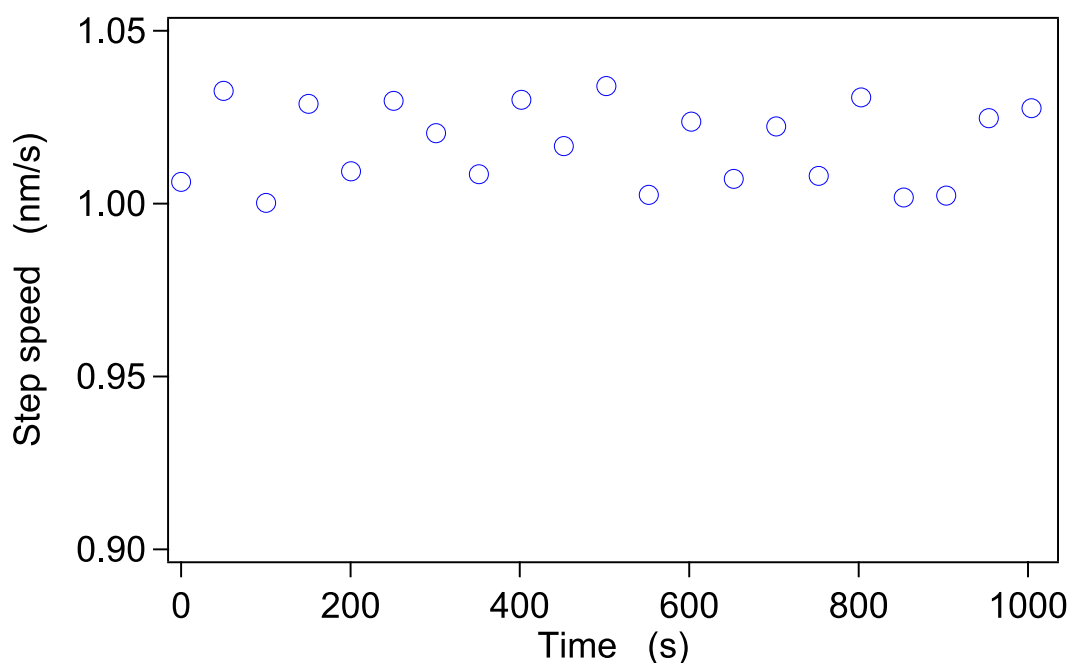


Figure 4.3 Step speed as a function of time during a typical experiment, in which the solution is replenished every 300 s. Note that the speed stays constant to within ~2%. The lack of systematic decrease in step speed before the growth solution is replaced suggests that the supersaturation remains approximately constant over the course of the our experiments.

The motion of growth steps was analyzed with the freeware-image processing software ImageJ (NIH) using a custom macro. We begin by selecting an individual step and drawing a perpendicular line. The ImageJ macro allows us to select the step in successive frames, and calculates its displacement along the perpendicular line. We calculate the step speed from the measured change in position with time. In order to unambiguously track an individual step, it is important to scan at a sufficiently fast rate, typically >20 scan lines per second, in our experiment. It should also be noted that because of step motion during the acquisition of individual AFM frames, the apparent step direction is distorted²⁸. To alleviate this problem, we only use alternate frames to measure step positions (although the intervening frames are used to unambiguously identify the progress of the selected step). This way, the scan direction (up or down) is consistent for each measured point. Figure 4.4 shows a sequence of three alternate frames (over a period of time thus spanning five frames in total) in which a single step can be tracked.

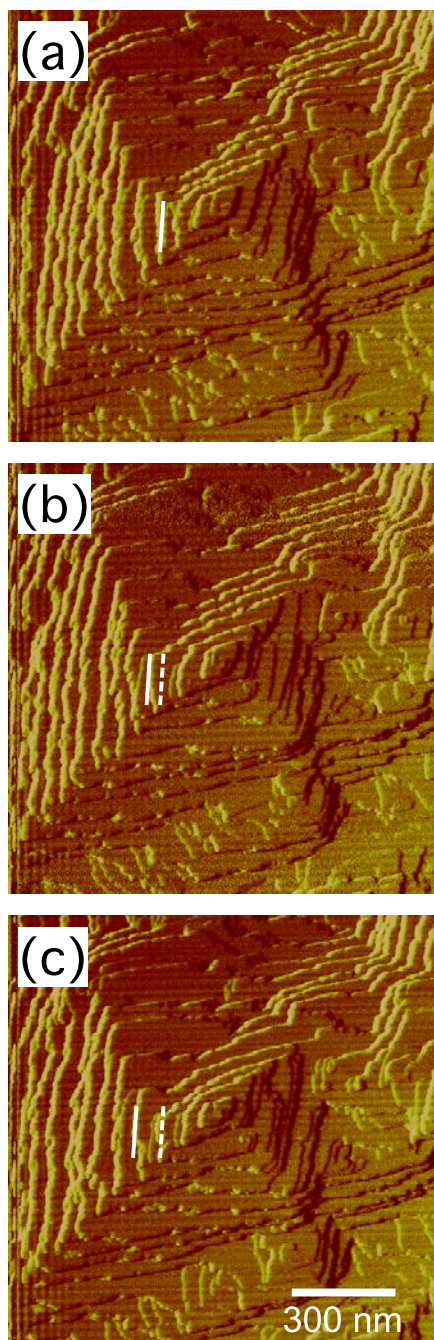


Figure 4.4 Series of AFM images acquired 50.2 s apart of a growth hillock on a (010) COM surface showing the advance of growth steps. The dashed lines in (b) and (c) show the original position, in (a), of the step indicated by the solid line.

4.3 Results

In agreement with previous studies, we found that the {010} faces of COM grow by a step-flow mechanism with steps typically originating from screw dislocations, as shown schematically in Fig. 2(b). The step propagation speed is a monotonically increasing function of supersaturation, as shown in Figure 4.5. Although the steps are not perfectly straight, it is possible to distinguish two main growth directions. We refer to these in terms of the crystallographic planes defining the step risers: $\langle 021 \rangle$ and $\langle 121 \rangle$. We find a slightly higher growth speed in the $\langle 021 \rangle$ directions, consistent with the aspect ratio of the growth hillocks.

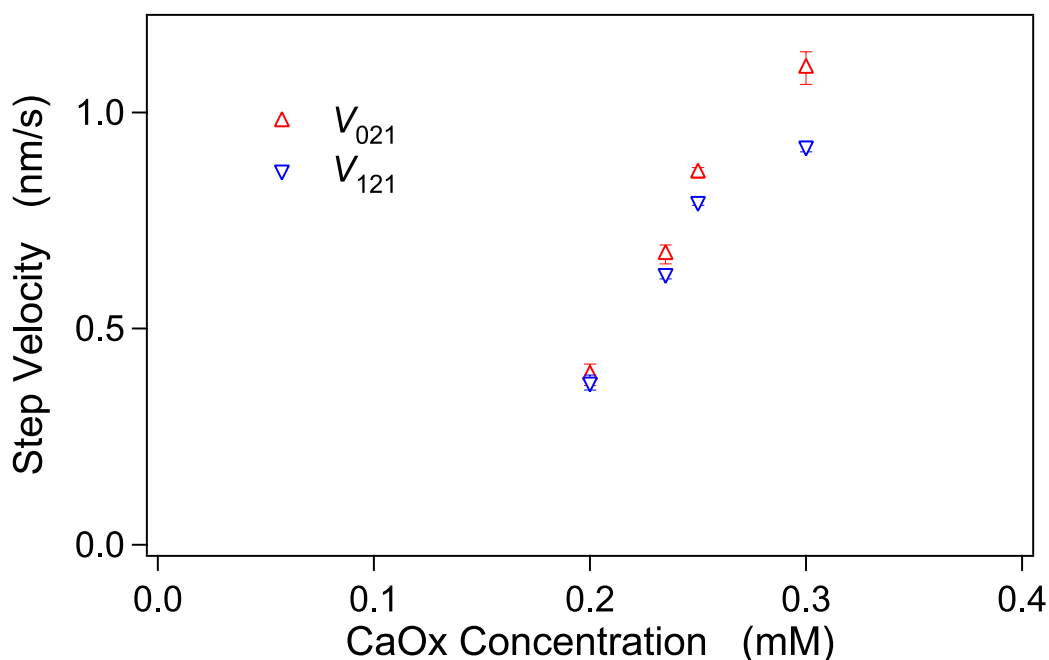


Figure 4.5 Step speeds on (010) COM faces as a function of supersaturation. Extrapolation to zero step speed suggests a saturation limit of approximately 0.15 mM.

Addition of pOPAR during growth, even at low concentrations, rapidly alters the growth steps. Figure 4.6 shows a sequence of AFM images during the poisoning of COM growth by the addition of pOPAR at a concentration of $0.1 \mu\text{g/mL}$ while holding the supersaturation constant at 0.95 ± 0.03 . After 20 min of growth, the steps have become scalloped to the point that they are difficult to distinguish, making the measurement of propagation velocities problematic.

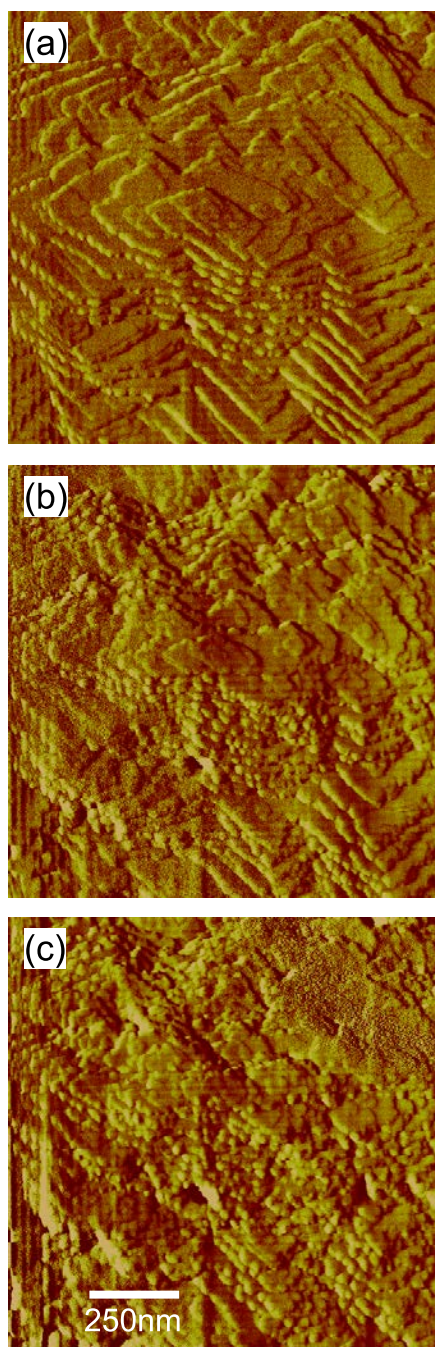


Figure 4.6 Series of AFM images showing the effect of the addition of $0.1 \mu\text{g/mL}$ pOPAR on COM growth at a supersaturation of 0.95 ± 0.03 at times of (a) 0 min, (b) 11.75 min, and (c) 23.5 min after the addition of pOPAR.

At lower pOPAR concentrations it proved possible to track steps as they slowed to a new steady-state velocity, which was typically reached within 20–60 min. Figure 4.7 shows measurements of the growth velocity in the $\langle 021 \rangle$ direction over a period of 91 min (100 frames), in which steps were poisoned by the addition of pOPAR.

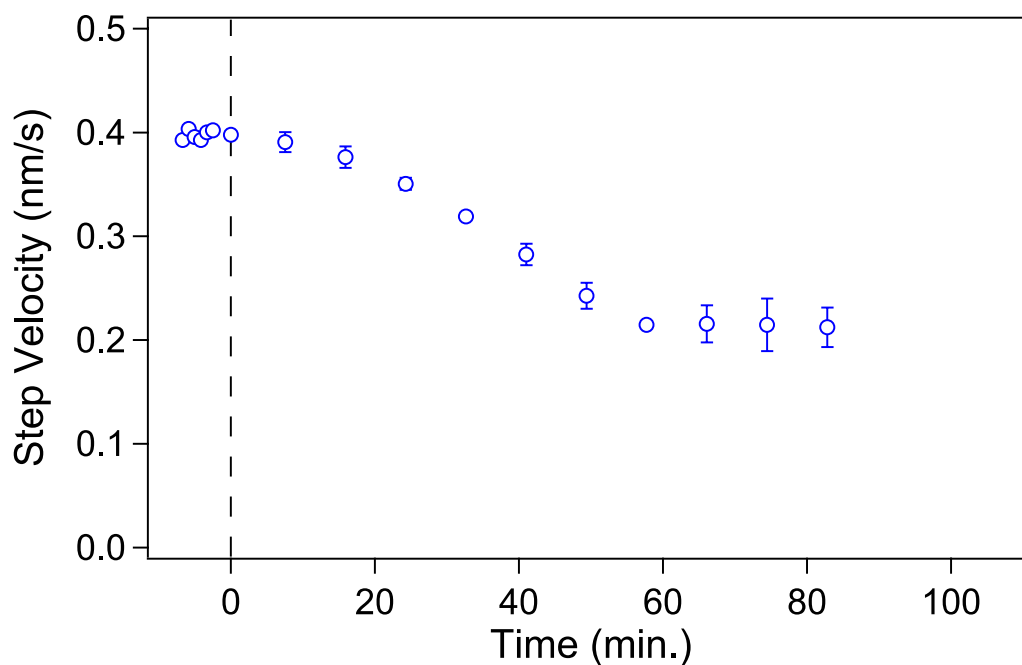


Figure 4.7 Step speed in the $\langle 021 \rangle$ direction as a function of time demonstrating the inhibition of growth steps by a concentration of $0.075 \mu\text{g/mL}$ pOPAR for COM growing at a constant supersaturation of 0.74 ± 0.04 . Time zero has been defined as the time of addition of OPAR. Note that reduced steady state velocity is not achieved until nearly 60 min after addition of the inhibitor.

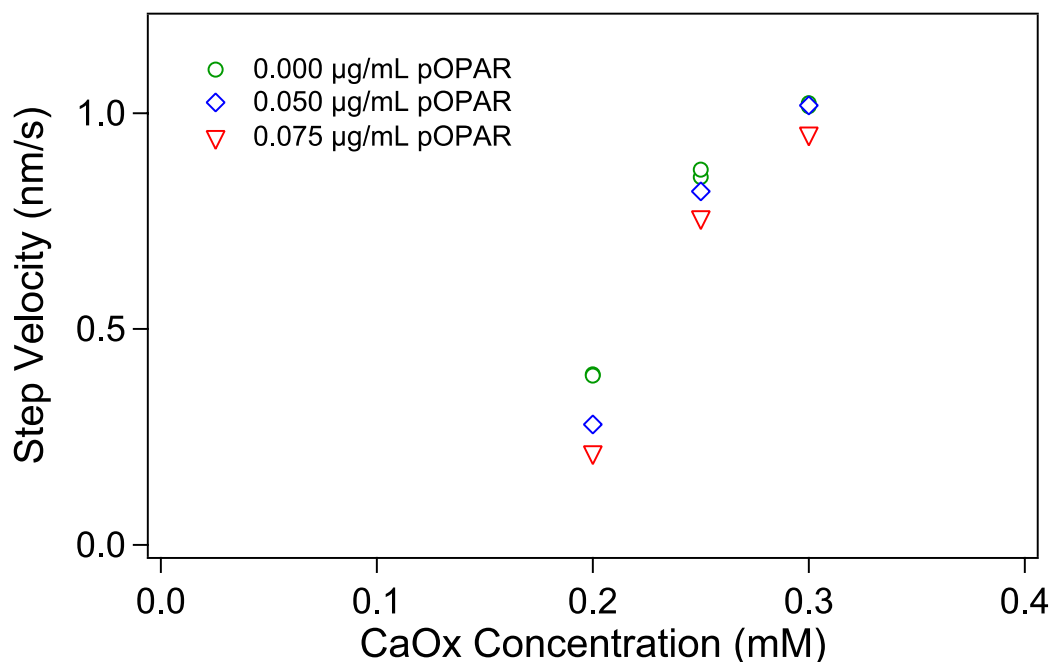


Figure 4.8 Speed of COM steps in the $\langle 021 \rangle$ directions as a function of supersaturation in the presence of varying levels of pOPAR. Note that the effect of pOPAR is more pronounced at low supersaturations, and that extrapolation to zero step velocity suggests a supersaturation “dead zone” that increases with the increasing pOPAR concentration in qualitative agreement with the Cabrera-Vermilyea model.

Fig. 4.8 compiles measurements of steady-state velocities of steps propagating in the $\langle 021 \rangle$ direction for a variety of supersaturation/inhibitor concentration combinations. It is evident that pOPAR decreases step velocities, with the largest effects at higher pOPAR concentration and lower calcium oxalate supersaturation. It is also apparent that pOPAR creates a supersaturation dead zone, as would be expected of the C-V mechanism. Although we have measured the effects of pOPAR at only three supersaturations, extrapolation of the growth curves for a given inhibitor concentration (0, 0.05, or 0.075 $\mu\text{g/mL}$) suggests that zero growth velocity—and hence an effective supersaturation of zero—will be achieved at a supersaturation that increases with increasing inhibitor concentration.

To investigate recovery from an inhibited state at the microscopic level, we imaged COM growing in alternately pure and pOPAR-containing solutions at a constant supersaturation. For this study, we chose relatively high concentrations of pOPAR, ranging from 1 to 5 $\mu\text{g/mL}$, to ensure rapid inhibition.

Figure 4.9 shows a series of AFM images from one such experiment. Here we see that the surface recovers to a pre-poisoned morphology after each poisoning cycle. As shown in Figure 4.10, the step velocity shows a rapid decrease during the inhibition phase, followed by a slower recovery to the initial velocity after the inhibitor has been flushed from solution. Although the difficulty in achieving complete replacement of the solution in the AFM fluid cell precludes quantitative interpretation, it is clear that surface poisoning is rapid compared to the recovery process. Since diffusion of pOPAR to the growth surface (e.g., through a boundary layer of unmixed growth solution) is expected to have a time scale similar to that away from the surface when the solution is exchanged, this asymmetry is likely due to non-diffusive processes at the surface.

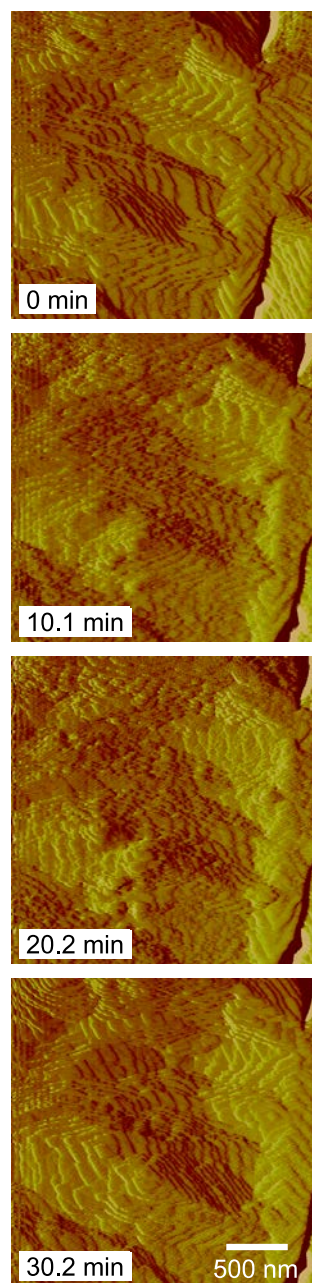


Figure 4.9 Series of AFM images acquired during growth/inhibition/recovery cycling of COM crystallization at a supersaturation of 0.95 ± 0.03 . A pOPAR concentration of $1 \mu\text{g/mL}$ was employed during the inhibition phases. Times indicated on the individual frames correspond to Fig. 4.10.

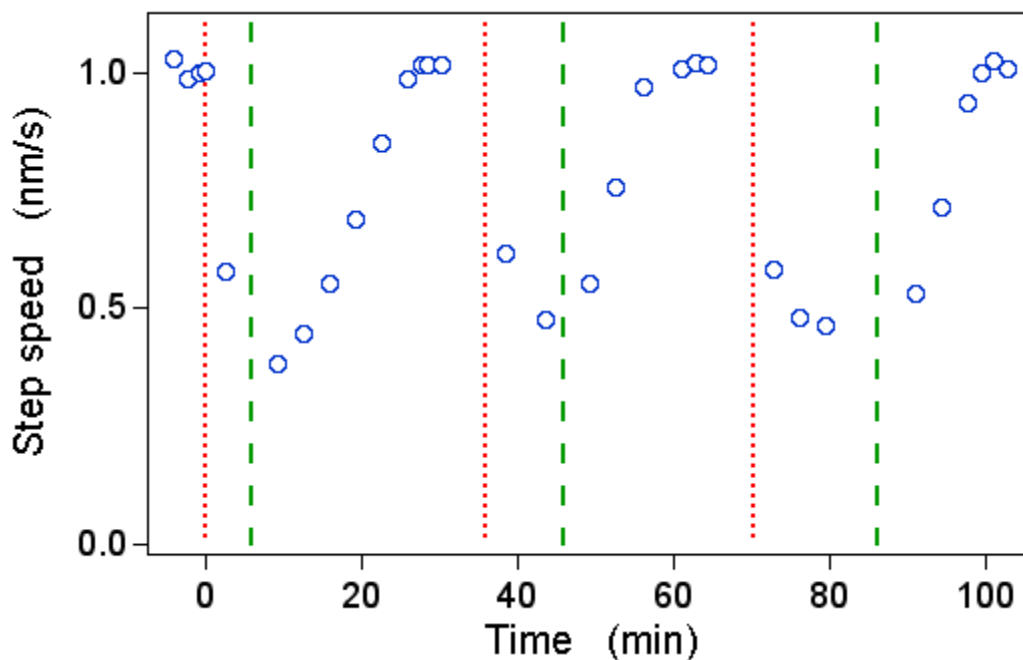


Figure 4.10 Step velocity as a function of time during growth-inhibition-recovery cycling of COM crystallization at a supersaturation of 0.95 ± 0.03 . The vertical lines indicate times at which pOPAR at a concentration of $1 \mu\text{g/mL}$ was added to (dotted lines) and removed from (dashed lines) the growth solution.

4.4 Discussion

Our observations of the change in step morphology on $\{010\}$ growth faces due to the presence of pOPAR are in qualitative agreement with the effects previously observed for OPN³. The transition from relatively straight steps to a scalloped form seen in Fig. 4.6 provides evidence for step pinning, as would be expected for the C-V model and its extensions. We have seen similar effects due to the addition of $1.01 \mu\text{M}$ ($2 \mu\text{g/mL}$) of another OPN phosphopeptide termed P3 (corresponding to amino acids 220-235 of rat bone OPN) as well as for 4.55 nM ($0.05 \mu\text{g/mL}$) poly-L-aspartic acid (data not shown). These results, along with the suggestion of a supersaturation dead zone in Fig. 4.5, provide strong evidence of inhibition due to step-pinning, rather than a more general alteration of the surface energy (e.g., the Anklam model Ref.16) or the poisoning of kink sites (as proposed by de Yoreo for the crystallization of low-solubility salts Ref. 18) for this system.

Recent molecular dynamics simulations by our group²¹ have measured the interaction between pOPAR and COM growth steps and terraces. These results show that pOPAR binds more strongly to step risers than to {010} surfaces. Our observation here of little change in the overall shape of the growth hillocks suggests an approximately equal interaction with both principal step directions. Interestingly, these simulations also predict a weaker adsorption than to the other principal growth faces, {100} and {121}. Preliminary studies of the effects of pOPAR on {100} faces are in agreement with this prediction; these will be reported at a later time.

The observation of continued growth for low concentrations of pOPAR raises the question of the ultimate fate of these adsorbates. For instance, at a supersaturation of 0.74 ± 0.04 and pOPAR concentration of $0.05 \mu\text{g/mL}$, we observe a steady-state step velocity of 0.28 nm/s and average step spacing of 60 nm , requiring that any point on the surface is covered by an advancing step within 210 s . There are three logical possibilities: the pOPAR must either desorb from the surface, move along the surface, or be incorporated in the growing crystal.

We have no evidence to support the motion of pOPAR molecules along the COM surface. For this process to occur, one would expect a migration of pOPAR molecules in the direction of step propagation, away from the centers of growth hillocks. Our observation that the centers of growth hillocks do not recover their initial morphology before points distant from the center after removal of pOPAR from the growth solution suggests that little migration along the COM surface occurs.

Desorption of pOPAR from COM surfaces would account for the recovery to an uninhibited state, albeit at the cost of the premise of step-pinning due to irreversible adsorption. In this case, one would expect the rate of decrease in the surface density of pOPAR to be proportional to the number of remaining molecules: i.e., an initially rapid decrease followed by an asymptotic approach to an unpoisoned surface. This predicted recovery is not apparent in Fig. 4.10, though confounding effects such as our ability to *completely* exchange the growth solution make definitive conclusions impossible.

Incorporation of pOPAR by the growing surface is supported by previous work from our group, which showed the incorporation of fluorescently labeled OPN and OPN peptides into COM crystals.^{15,29} More recently, incorporation of an OPN peptide into calcium oxalate dihydrate crystals was demonstrated using the same method³⁰. We therefore propose an alternative to the hypothesis proposed by De Yoreo

et al. of a finite lifetime of inhibitor molecules on growth faces¹⁷. In our picture, pOPAR molecules bind nearly irreversibly to step-risers on {010} COM faces, accounting for the pinning seen by atomic force microscopy. The step curvature resulting from this pinning results in a decreased growth velocity via the Gibbs-Thomson effect, in accordance with the C-V model. A new steady-state density of pinning sites (and therefore a constant reduced growth velocity) is achieved by a balance between incorporation of pOPAR molecules by propagating steps, resulting in their removal from the growth surface, and the adsorption of additional pOPAR molecules onto newly created surfaces.

Future experiments over a range of inhibitor concentrations and calcium oxalate supersaturations, and involving a variety of inhibitors, will test the validity of our model.

4.5 Conclusions

The Cabrera-Vermilyea has been successful in explaining the inhibition of crystallization in many systems in terms of the pinning of growth steps by strongly adsorbed impurities. However, the irreversible adsorption required to pin steps is in seeming contradiction with the observation that the degree of inhibition is proportional to the concentration of inhibitor available in solution. By examining the recovery of calcium oxalate surfaces from poisoning by pOPAR, a phosphopeptide of osteopontin, we are able to gain insight into the inhibition mechanism. To our knowledge, this is the first quantitative study of the recovery of growth steps from impurity-pinning. Specifically, we find that poisoning by added pOPAR is rapid relative to the time required for recovery to an uninhibited state after pOPAR is removed, but full recovery does occur. Moreover, after removal of pOPAR from the growth solution, the acceleration of step speeds is initially low, and increases over time. These results are consistent with a model³¹ in which the degree of inhibition is dependent on the density of inhibitor molecules adsorbed on the surface, in accordance with the C-V model, but in which the steady-state density results from a balance between the rate of adsorption and rate of incorporation into the growing crystal, rather than a balance between adsorption and desorption, as is often assumed.

This work will provide an improved understanding of the mechanism of crystallization inhibition in this system and may have applications to a wider variety of commercially and biologically important growth processes. In addition, our increased understanding of the role of osteopontin and derived peptides may be useful for the design of therapeutic agents for the treatment of kidney stones.

4.6 Bibliography for Chapter 4

- 1 D. A. Bushinsky, "Kidney stones," *Adv Intern Med* **47**, 219-238 (2001).
- 2 H. Shiraga, W. Min, W. J. Vandusen, M. D. Clayman, D. Miner, C. H. Terrell, J. R. Sherbotie, J. W. Foreman, C. Przysiecki, E. G. Neilson, and J. R. Hoyer, "Inhibition of Calcium-Oxalate Crystal-Growth Invitro by Uropontin - Another Member of the Aspartic Acid-Rich Protein Superfamily," *Proc Natl Acad Sci U S A* **89** (1), 426-430 (1992).
- 3 S. R. Qiu, A. Wierzbicki, C. A. Orme, A. M. Cody, J. R. Hoyer, G. H. Nancollas, S. Zepeda, and J. J. De Yoreo, "Molecular modulation of calcium oxalate crystallization by osteopontin and citrate," *Proc Natl Acad Sci U S A* **101** (7), 1811-1815 (2004).
- 4 A. Taller, B. Grohe, K. A. Rogers, H. A. Goldberg, and G. K. Hunter, "Specific adsorption of osteopontin and synthetic polypeptides to calcium oxalate monohydrate crystals," *Biophys J* **93** (5), 1768-1777 (2007).
- 5 J. A. Wesson, E. M. Worcester, and J. G. Kleinman, "Role of anionic proteins in kidney stone formation: Interaction between model anionic polypeptides and calcium oxalate crystals," *J Urology* **163** (4), 1343-1348 (2000).
- 6 B. Grohe, K. A. Rogers, H. A. Goldberg, and G. K. Hunter, "Crystallization kinetics of calcium oxalate hydrates studied by scanning confocal interference microscopy," *J Cryst Growth* **295** (2), 148-157 (2006).
- 7 M. Weaver, S. Qiu, J. Hoyer, W. Casey, G. H. Nancollas, and J. J. De Yoreo, "Surface Aggregation of Urinary Proteins and Aspartic Acid-Rich Peptides on the Faces of Calcium Oxalate Monohydrate Investigated by In Situ Force Microscopy," *Calcified Tissue Int* **84** (6), pg. 462-473 (2009).
- 8 N. Cabrera, and D. A. Vermilyea, "Growth of crystals from solution", in *Growth and Perfection of Crystals: Proceedings*, edited by R. H. Doremus, B. W. Roberts and D. Turnbull, (Wiley, New York, 1958), pp. 393-410.
- 9 J. A. Raymond, Y. Lin, and A. L. Devries, "Glycoprotein And Protein Antifreezes In 2 Alaskan Fishes," *J Exp Zool* **193** (1), 125-130 (1975).
- 10 A. A. Abrosimov, Z. M. Pishchaeva, V. A. Vinokurov, S. T. Bashkatova, and T. P. Vishnyakova, "Daks-D depressant additive for diesel fuels," *Chem Tech Fuels Oils* **35** (5), 300-301 (1999).

- 11 H. Quar, S. B. Cha, T. R. Wildeman, and E. D. Sloan, "The Formation of Natural-Gas Hydrates In Water-Based Drilling-Fluids," *Chem Eng Res Des* **70** (1), 48-54 (1992).
- 12 R. W. Friddle, M. L. Weaver, S. R. Qiu, A. Wierzbicki, W. H. Casey, and J. J. De Yoreo, "Subnanometer atomic force microscopy of peptide-mineral interactions links clustering and competition to acceleration and catastrophe," *Proc Natl Acad Sci U S A* **107** (1), 11-15 (2010).
- 13 J. A. Wesson, V. Ganne, A. M. Beshensky, and J. G. Kleinman, "Regulation by macromolecules of calcium oxalate crystal aggregation in stone formers," *Urol Res* **33** (3), 206-212 (2005).
- 14 M. L. Weaver, S. R. Qiu, J. R. Hoyer, W. H. Casey, G. H. Nancollas, and J. J. De Yoreo, "Inhibition of calcium oxalate monohydrate growth by citrate and the effect of the background electrolyte," *J Cryst Growth* **306** (1), 135-145 (2007).
- 15 G. K. Hunter, B. Grohe, S. Jeffrey, J. O'Young, E. S. Sorensen, and H. A. Goldberg, "Role of Phosphate Groups in Inhibition of Calcium Oxalate Crystal Growth by Osteopontin," *Cells Tissues Organs* **189** (1-4), 44-50 (2009).
- 16 M. R. Anklam and A. Firoozabadi, "An interfacial energy mechanism for the complete inhibition of crystal growth by inhibitor adsorption," *J Chem Phys* **123** (14) (2005).
- 17 M. L. Weaver, S. R. Qiu, R. W. Friddle, W. H. Casey, and J. J. De Yoreo, "How the Overlapping Time Scales for Peptide Binding and Terrace Exposure Lead to Nonlinear Step Dynamics during Growth of Calcium Oxalate Monohydrate," *Crystal Growth & Design* **10** (7), 2954-2959 (2010).
- 18 J. J. De Yoreo, L. A. Zepeda-Ruiz, R. W. Friddle, S. R. Qiu, L. E. Wasylenki, A. A. Chernov, G. H. Gilmer, and P. M. Dove, "Rethinking Classical Crystal Growth Models through Molecular Scale Insights: Consequences of Kink-Limited Kinetics," *Crystal Growth & Design* **9** (12), 5135-5144 (2009).
- 19 T. A. Land, T. L. Martin, S. Potapenko, G. T. Palmore, and J. J. De Yoreo, "Recovery of surfaces from impurity poisoning during crystal growth," *Nature* **399** (6735), 442-445 (1999).
- 20 R. I. Ristic, J. J. DeYoreo, and C. M. Chew, "Does impurity-induced step-bunching invalidate key assumptions of the Cabrera - Vermilyea model?," *Crystal Growth & Design* **8** (4), 1119-1122 (2008).

- 21 S. Hug, B. Grohe, J. Jalkanen, B. Chan, B. Galarreta, K. Vincent, F. Lagugne-Labarthe, G. Lajoie, H. A. Goldberg, M. Karttunen, and G. K. Hunter, "Mechanism of inhibition of calcium oxalate crystal growth by an osteopontin phosphopeptide," *Soft Matter* **8** (4), 1226-1233 (2012).
- 22 B. Grohe, B. P. Chan, E. S. Sorensen, G. Lajoie, H. A. Goldberg, and G. K. Hunter, "Cooperation of phosphates and carboxylates controls calcium oxalate crystallization in ultrafiltered urine," *Urol Res* **39**, 327–338 (2011).
- 23 P. V. Azzopardi, J. O'Young, G. Lajoie, M. Karttunen, H. A. Goldberg, and G. K. Hunter, "Roles of charge and conformation in protein-crystal interactions," *Plos One* **5** (e9330), 1-11 (2010).
- 24 B. B. Tomazic and G. H. Nancollas, "A study of the phase transformation of calcium oxalate trihydrate-monohydrate," *Invest Urol* (16), 329-335 (1979).
- 25 C. H. Hamann, A. Hamnett, and W. Vielstich, *Electrochemistry*, (Wiley-VCH, New York, 1998).
- 26 T. Jung, X. X. Sheng, C. K. Choi, W. S. Kim, J. A. Wesson, and M. D. Ward, "Probing crystallization of calcium oxalate monohydrate and the role of macromolecule additives with in situ atomic force microscopy," *Langmuir* **20** (20), 8587-8596 (2004).
- 27 S. W. Guo, M. D. Ward, and J. A. Wesson, "Direct visualization of calcium oxalate monohydrate crystallization and dissolution with atomic force microscopy and the role of polymeric additives," *Langmuir* **18** (11), 4284-4291 (2002).
- 28 V. Y. Yurov and A. N. Klimov, "Scanning Tunneling Microscope Calibration and Reconstruction Of Real Image - Drift And Slope Elimination," *Rev. Sci. Instrum.* **65** (5), 1551-1557 (1994).
- 29 J. O'Young, S. Chirico, N. Al Tarhuni, B. Grohe, M. Karttunen, H. A. Goldberg, and G. K. Hunter, "Phosphorylation of Osteopontin Peptides Mediates Adsorption to and Incorporation into Calcium Oxalate Crystals," *Cells Tissues Organs* **189** (1-4), 51-55 (2009).
- 30 Y. C. Chien, D. L. Masica, J. J. Gray, S. Nguyen, H. Vali, and M. D. McKee, "Modulation of Calcium Oxalate Dihydrate Growth by Selective Crystal-face Binding of Phosphorylated Osteopontin and Polyaspartate Peptide Showing Occlusion by Sectoral (Compositional) Zoning," *J. Biol. Chem.* **284** (35), 23491-23501 (2009).

- 31 S. S. Nene, G. K. Hunter, H. A. Goldberg, and J. L. Hutter, "Reversible Inhibition of Calcium Oxalate Monohydrate Growth by an Osteopontin Phosphopeptide," *Langmuir* **29** (21), 6287-6295 (2013).

Chapter 5: Regrowth of calcium oxalate etch-pit on {100} faces

5.1 Background

Calcium oxalate monohydrate ($\text{CaC}_2\text{O}_4 \cdot \text{H}_2\text{O}$, hereafter referred to as COM) is major component of kidney stones. Understanding the interactions between COM crystal surfaces and macromolecular inhibitors that are known to control kidney stone formation may lead to the design of therapeutic agents for the prevention of kidney stones. Various studies have been performed to characterize COM crystals formed in the presence of a range of natural and synthetic macromolecular inhibitors to achieve insight into the molecular mechanisms of the important impurity-crystal interactions^{1,2,3}. A number of elements present in urine can play a preventive role in the formation of COM stones. Osteopontin (OPN), a urinary protein, has been shown to inhibit the *in vitro* crystallization of COM^{1,4}. In kidneys it is said to control the urinary calcium oxalate deposits by preventing the formation of kidney stones⁵. Significantly modified growth habits of COM crystals grown in the presence of OPN have been demonstrated³. In the case of COM, OPN preferentially binds to the edge between {100} and {121} faces³. Post-translational modifications which increase the acidity of a protein, e.g., phosphorylation in the case of OPN⁶, have been shown to increase the growth-inhibiting effect^{4,6,7}. In order to get more information about which parts of OPN play a significant role in the COM-growth-inhibiting mechanism, peptides corresponding to different sequences of rat OPN have been created and studied in our laboratory.

In order to study the effect of inhibitors on COM growth, we would ideally image step flow on all individual faces expressed during growth. For {100} faces of COM the high surface density of calcium ions on these faces is thought to result in a net positive charge and a strong interaction with anionic macromolecules.⁸ Previous studies in our laboratory have used confocal microscopy⁹ and molecular dynamics (MD) simulations¹⁰ to show that increased peptide phosphorylation results in more effective growth inhibition. However, although the presence of growth hillocks of COM {100} surfaces have been observed in air and supersaturated CaOx^{11} , we typically do not see clear examples of these features in our studies. This prevents us from directly imaging step motion on {100} faces using the atomic force microscope (AFM).

Guo et al.¹² demonstrated a method in which they dissolved COM surfaces with water or undersaturated solution to form elongated hexagonal pits with perimeters typically defined by $\{121\}$ and $\{010\}$ planes oriented along the $[001]$ direction as shown in Fig. 5.1. When an etched surface is placed in supersaturated calcium oxalate (CaOx) solution, the pits gradually disappear due to growth of the bounding surfaces.

In this study, we used the same method to investigate the re-growth of etch-pits on COM $\{100\}$ faces in the presence of poly(aspartic acid) (poly-ASP) and a peptide based formed from residues of rat bone OPN with different degrees of phosphorylation (P0 [SHESTEQSDAIDSAEK], P3 [pSHEpSTEQSDAIDpSAEK] and pOPAR[pSHDHMDDDDDDDDGD]) at two different concentrations (5 $\mu\text{g/ml}$ and 10 $\mu\text{g/ml}$) in supersaturated CaOx solutions. This method permitted real-time observations of pit-filling using the atomic force microscope (AFM). Along with changes in the ratio of inhibition in the two main directions of the etch pits, this also gives us information on the interaction of these peptides with $\{121\}$ faces, which we could not study otherwise, as these faces are not typically expressed in an orientation accessible to atomic force microscopy.

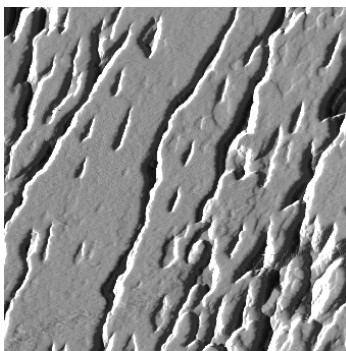


Figure 5.1 AFM deflection image ($2\ \mu\text{m} \times 2\ \mu\text{m}$) of etch pits on a COM (100) surface. The pits were formed by immersion in pure water for about 20 minutes. The etch pits have a typical length of $\sim 150\ \text{nm}$ along the $[001]$ direction and $\sim 50\ \text{nm}$ along the $[010]$ direction.

5.2 Method

5.2.1 Sample Preparation

COM crystals grown on glass substrates as described in Section 4.2 were immersed in deionized water for 20 minutes to create etch-pits. The crystals were then separated with a plastic spatula from the substrate. The crystals were removed from solution by filtration through polycarbonate membrane filters with 13 mm diameter and 0.8 μm pore size (VWR 28158-125) mounted in a 13 mm Swinney plastic filter holder (Pall corp. 4317). After filtration, the membrane was dried for 2 hours at room temperature. A glass substrate was coated with UV-curable optical adhesive (Norland optical Adhesive 81), and partially cured. The membrane with COM crystals was brought into contact with the partially cured substrate surface. After removing the membrane, the substrate was cured for an additional 15 minutes, fixing the crystals firmly, mounted onto an AFM specimen holder.

All experiments were done in our lab using a MultiMode AFM with Nanoscope IIIa controller with CaOx growth solutions of 0.235 mM concentration. Imaging was performed in contact mode using a glass fluid cell (Digital Instruments) at ambient temperature (approximately 30 °C in the fluid cell). The sample was then transferred to the AFM sample stage with fluid cell for in-situ imaging. Freshly-prepared supersaturated CaOx solutions were used for each growth experiment. Soon after the fluid cell was filled with the working solution, contact-mode imaging was performed at scan rates between 2.0 and 2.5 Hz. Using two syringes, one to inject fresh solution and one to withdraw solution, the working solution was refreshed at 5 minute intervals to maintain a relatively constant supersaturation in the fluid cell.

5.2.2 Image Analysis

Fig 5.2 shows an example of etch-pit regrowth due to a supersaturated CaOx solution of 0.235 mM concentration. A clear change in each pit's circumference as a function of time due to a gradual pit filling can be seen in the image sequence from (a) to (d). Measurements of the pit circumference as a function of time can be used to measure the growth rate. In order to measure this accurately, image processing was performed using a set of custom-written macros in ImageJ (NIH).

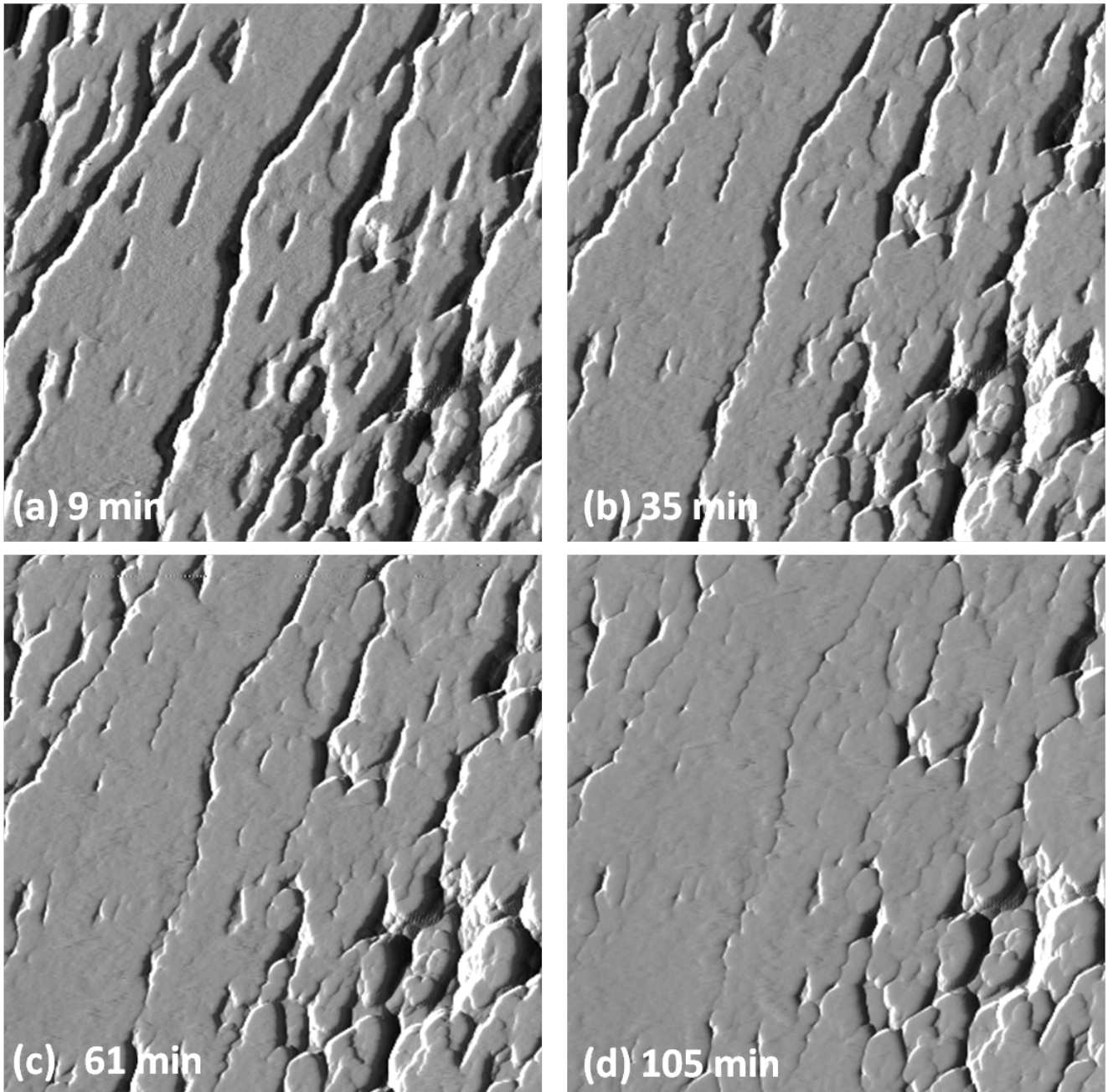


Figure 5.2 Sequence of AFM deflection images ($2\ \mu\text{m} \times 2\ \mu\text{m}$) showing etch-pit regrowth of a (100) COM surface in the presence of 0.235 mM CaOx.

In order to accurately measure the circumference of the pits, it is necessary to clearly define the boundaries of the pits. Because the surfaces of a pit, by definition, lie below the plane of the crystal surface, the region inside the pit can be selected as the set of image pixels whose height lies below that

plane. However, the crystal surface is not necessarily coplanar with the image plane. Therefore, we must first perform a local tilt correction in the region surrounding a pit. We select a “region of interest” (ROI) around an individual pit as shown in Fig. 5.3 (b). The values of the corner pixels are used to determine a best-fit plane, which is subtracted from the values of all pixels within the ROI using a custom macro (and a constant offset added to leave the overall height similar to the original image). We then apply a threshold to the ROI to identify all points below the corrected image plane, which are assumed to be part of the pit. In practice the pit dimensions are relatively insensitive to the precise threshold value used. In Fig. 5.3 (c), all pixels below the chosen threshold are coloured red. To measure the pit, the “magic wand” tool in ImageJ is used, which selects the region at or below the threshold value, and returns the area and circumference of the region. These measurements are repeated on a series of images of a given pit obtained while the sample regrows.

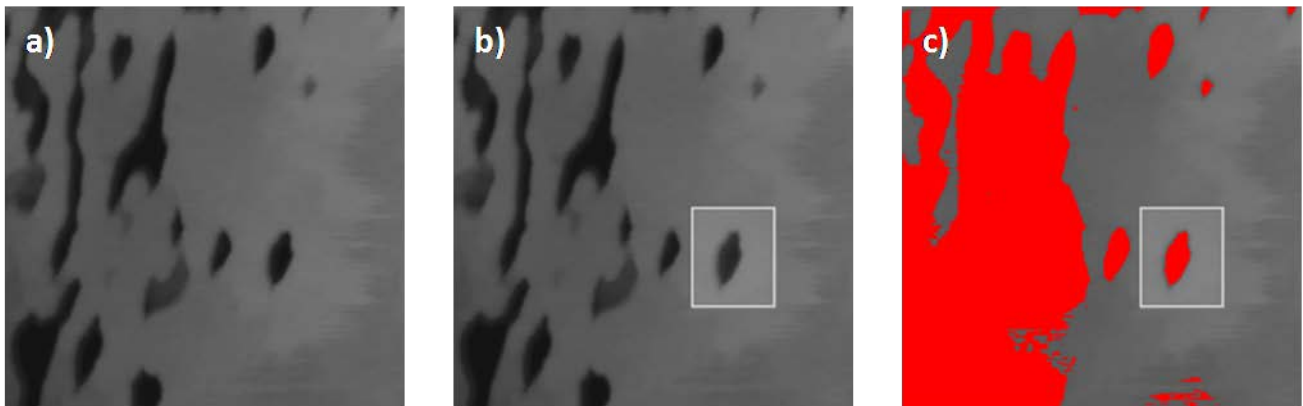


Figure 5.3 Steps in measuring dimensions of etch pits. (a) Raw AFM height image ($1.25 \mu\text{m} \times 1.25 \mu\text{m}$). (b) An ROI defined around a single etch pit. The region within the ROI has been tilt-corrected by a plane fit. (c) Thresholded data used for the measurement of the etch-pit area and circumference.

5.3 Measurements

Measurements of the change in the area of an etch pit as function of time can be used to quantify the regrowth rate. As seen in Fig. 5.2, the pit area clearly decreases throughout the experiment, and pits are eventually filled completely. Fig. 5.4 plots the area of several etch pits as a function of time in the presence of 10 $\mu\text{g/ml}$ of pOPAR.

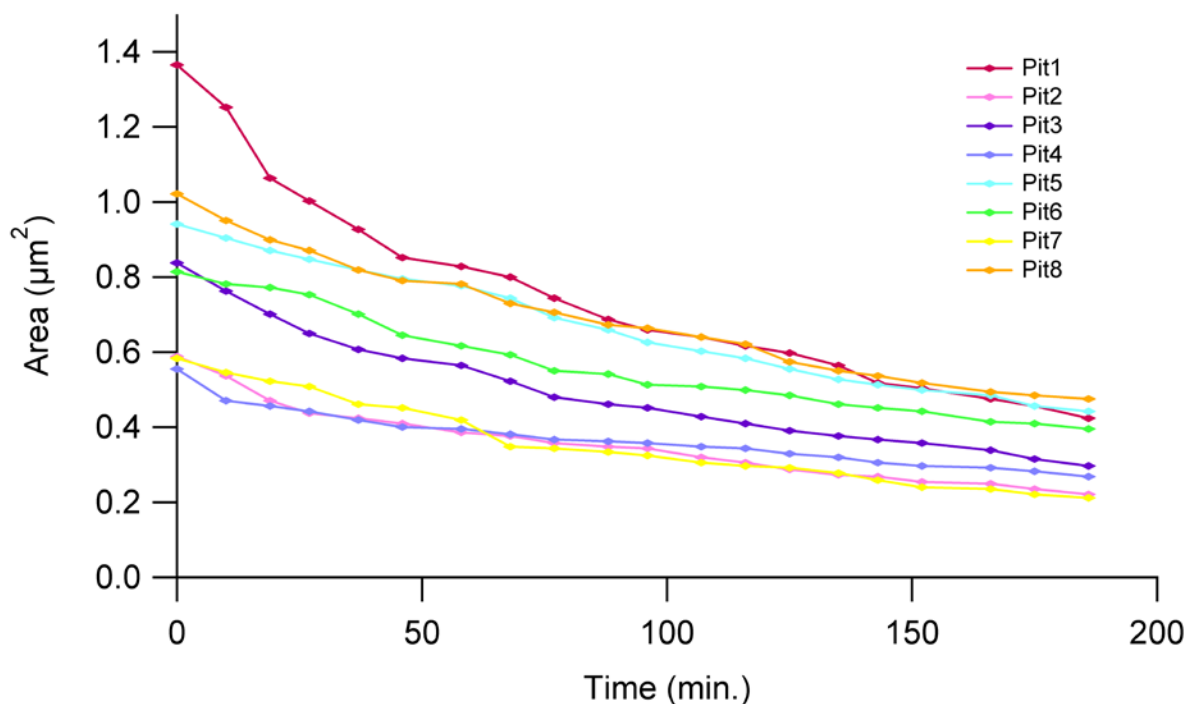


Figure 5.4 Change in pit area as function of time for etch-pit regrowth in the presence of 10 $\mu\text{g/ml}$ of pOPAR at 0.235 mM CaOx concentration.

As seen in Fig 5.3, not all pits have the same area. As a result, smaller pits will be filled in completely before larger pits. In a previous study by Guo et al.¹², the authors chose to analyze etch-pits of similar initial size. As a result it is difficult to compare measurements for different etch pits in the presence of different inhibitors, or even in the presence of the same inhibitor. In this work, we calculate a growth rate that is independent of initial pit area as described below.

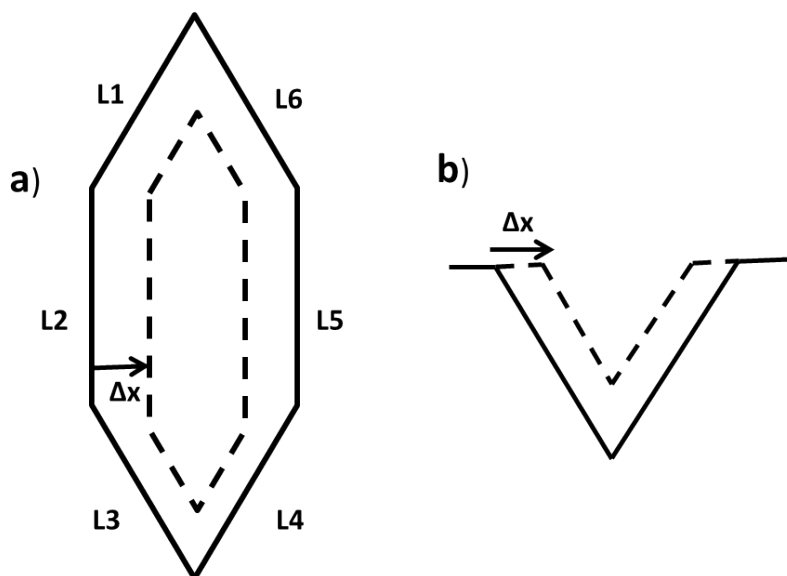


Figure 5.5 Etch-pit filling schematic with (a) indicating the apparent growth Δx and (b) showing a cross-sectional view of a re-growing pit.

We begin by measuring the total perimeter of the pit. Figure 5.5 shows a schematic in which the perimeter of a pit is given by

$$P = L1 + L2 + L3 + L4 + L5 + L6$$

where L_i refers to the different sides. As the pits re-grow, the boundaries move in by an average distance Δx , resulting in an area change

$$\Delta A = -P \Delta x.$$

From this, we can calculate an average growth rate, which is independent of initial pit area, in the plane of the (100) surface as

$$G = \Delta x / \Delta t = (\Delta A / P) / \Delta t$$

The re-growth rate of etch pits in the presence of $10 \mu\text{g/ml}$ pOPAR is plotted as a function of time in Fig 5.6. Aside from initial transient behavior in the first 15–20 minutes, the growth rate was relatively constant. Relative to the case with no additives, we found that the additives tested decrease growth, with relative efficiency pOPAR > poly-ASP > P3 > P0, Table VII summarizes all the growth-rate data from etch-pit re-growth rates for the different concentrations of peptides used for this work.

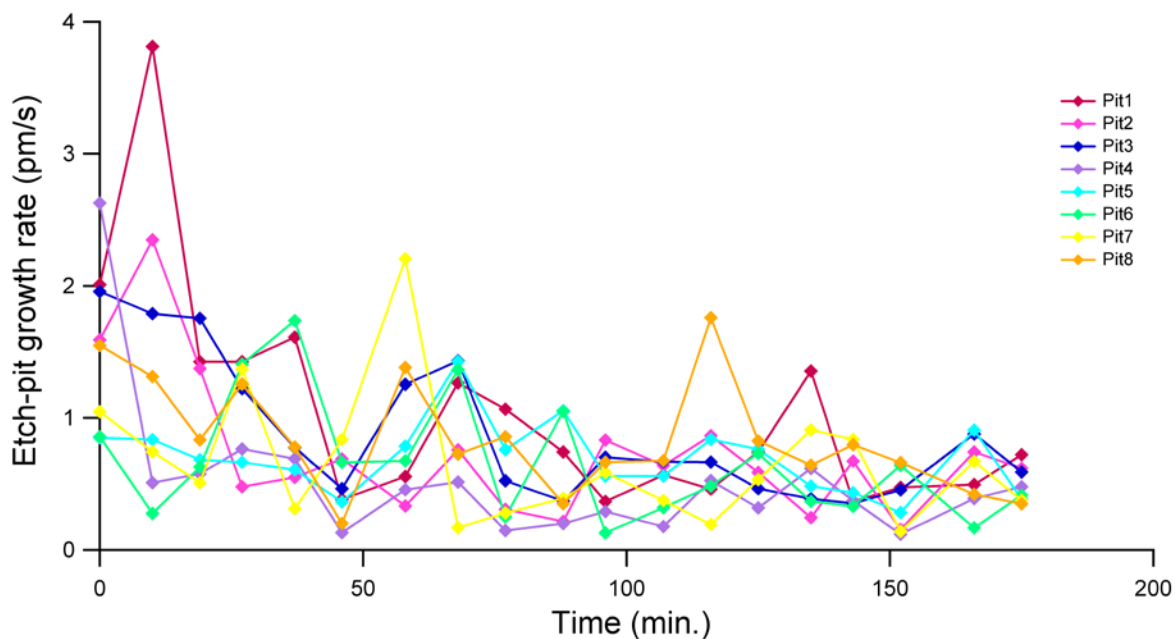


Figure 5.6 Etch pit regrowth rate as a function of time for growth in the presence of 10 $\mu\text{g/mL}$ of pOPAR at a growth concentration of 0.235mM of CaOx.

Table IX Pit filling rate for all the additives in this work.

Peptide	Pit filling rate (pm/s) 5 $\mu\text{g/ml}$	Pit filling rate (pm/s) 10 $\mu\text{g/ml}$
P0	2.23 ± 0.70	1.68 ± 0.54
P3	1.84 ± 0.77	1.29 ± 0.39
Poly-ASP	1.64 ± 0.81	1.02 ± 0.66
pOPAR	1.59 ± 0.57	0.75 ± 0.33

5.4 Discussion

When immersed in deionized water, elongated pits oriented along the $\langle 001 \rangle$ direction are formed on the (100) face of the COM crystal. Their pits are predominantly bounded by {010} and {121} planes, as indicated by a shape and orientation matching those of the bulk crystal. Many of these features contain one angle of 72° , exactly the angle between family of $\langle \bar{1} 2 \bar{1} \rangle$ and $\langle \bar{1} \bar{2} \bar{1} \rangle$ planes intersecting the (100) face, which reflects the symmetry for the bulk crystal.^{11,13}

Guo et. al.¹² studied face-specific growth and dissolution rates on COM (100) surfaces with AFM by observing the evolution of surface pits. They demonstrated that polyaspartate (poly-ASP) is an effective inhibitor of COM crystal growth. The authors further found that the poly-ASP macromolecules exerted a greater influence on growth in the $\langle 001 \rangle$ directions, seemingly due to adsorption to the {021} and {001} surfaces of the COM crystals. Previous studies in our group using fluorescently labeled peptides have shown that P0 and P3 adsorb to the {100} face of COM⁹. Another group member has been investigating the effect of pOPAR on {100}, {010} and {121} faces using classic molecular dynamic simulations combined with confocal microscopy. From these studies, it appears that pOPAR adsorbs most strongly to the {100}, faces, less strongly to {010} faces, and least to {121} faces¹⁰.

In this work, a monotonic decrease in pit area with time was observed in 0.235 mM CaOx solution. The growth rate, independent of initial pit area in the plane of the (100) surface, was found to be 2.50 ± 0.42 pm/s at 0.235 mM CaOx concentration, sufficiently slow to acquire AFM data on etch pit re-growth in a reasonable time frame. With fixed CaOx concentration, the effects of poly(aspartate) and peptides of OPN on pit re-growth on COM (100) surfaces are demonstrated in table IX. A significant decrease in growth rate is seen in all cases, with a larger decrease at higher additive concentrations. Complete inhibition of etch-pit re-growth was not observed within our experimental conditions and time scale.

The growth rate determined here corresponds to the rate of advance of the faces bounding the etch pits. The numerical value of ~ 2.5 pm/s is similar to that expected for {010} growth faces at the same supersaturation, as can be inferred from the data in Chapter 4. There, we measured typical step velocities of ~ 0.6 nm/s (see Fig. 4.8) with a spacing of ~ 75 nm between steps. Given the step height of 1.4 nm (determined from AFM data, and consistent with the COM unit cell), this corresponds to a normal growth rate of ~ 11.2 pm/s. The lower value measured here may be due to the geometry of the

pits (i.e., multiple growth faces in a nearly-enclosed volume, resulting in enhanced depletion within the pits).

In order to determine the peptide sequences responsible for the inhibition of COM by OPN, our group has studied the effects of separate 16-amino acid sequences of the OPN molecule on growth of COM.^{10,14} Molecular dynamics (MD) simulations have been used to predict the adsorption of 19 peptides, each with 16 amino acids, covering the entire OPN molecule onto the {100} face of hydroxyapatite¹⁵. Moreover, the importance of degree of phosphorylation of the OPN 220–235 sequences has been examined. A phosphorylated aspartic/glutamic acid-rich sequence synthesized to contain zero, one or three phosphorylations (P0, P1, P3) has been shown to have an effect on growth of the {100} faces of COM that increases with the degree of phosphorylation.

The OPN 65–80 sequence contains a poly(aspartic acid) sequence of OPN, and is thought to have a strong affinity to anionic COM faces. In this study we examine the effects of these subsequences of OPN in an attempt to better understand the inhibitory mechanism due to OPN. MD simulation suggests that the degree to which each peptide inhibits the growth of {100} faces is dependent on the phosphate content of peptide. Phosphorylated peptides form more stable contacts with the crystal surface.¹⁵ These results indicate greater adsorption of P3 compared to P0, and the results for the present work are in good agreement with this claim: our pit filling data show that P3 has a higher effect on the growth rate than does P0 for COM {100} surfaces. We have demonstrated that of the 16-residue peptides studied, pOPAR shows the maximum effect. Along with being a phosphorylated peptide, it is an aspartic acid rich section of OPN, which is consistent with higher adsorption onto the etch-pit surfaces, consequently reducing the etch-pit filling rate.

5.5 Summary

Previous work in our laboratory^{3,10,14,15} has suggested that a synthetic peptide corresponding to amino acids 220-235 of rat bone OPN adsorbs selectively to {100} faces and preferentially inhibits growth in $\langle 100 \rangle$ directions (perpendicular to {100} faces). Due to lack of visible growth features such as growth hillocks, direct AFM imaging of growth on the COM {100} surfaces was not feasible. Instead, COM crystals were dissolved in pure water for ~20 minutes to form elongated etch pits oriented along the [001] direction and having perimeters defined mostly by {010} and {021} planes, but in addition to

that, the presence of different families of planes such as {021}, {120} cannot be overlooked. Gradual regrowth of these pits was observed in the presence of supersaturated CaOx solution. Guo et al.¹² had previously used this method to study the effect of the polymeric additives poly(aspartate acid) and poly(glutamate acid) on COM (100) faces, but in contrast to their work, in which the rate of change of pit area is quoted, we calculate a growth-rate that is independent of initial pit area.

In this work, we demonstrated the effect of peptides of OPN (P0, P3 and pOPAR) and poly-ASP on etch-pit filling on COM {100} surfaces. Inhibition of overall growth rate by additives altered the pit-filling rate compared to control experiments in the absence of polymer. We have demonstrated that the 16-residue length pOPAR molecule shows the maximum effect on the etch-pit re-growth rate among the selection of additives we studied. Along with being a phosphorylated peptide, it is an aspartic acid rich section of the OPN which is consistent with its higher adsorption to growth surfaces, consequently reducing the etch-pit filling rate. Molecular dynamics simulations have shown a greater adsorption of P3 compared to P0¹⁶, and the results of this work are in good agreement with the claim.

5.6 Bibliography for Chapter 5

- 1 H. Shiraga, W. Min, W. J. Vandusen, M. D. Clayman, D. Miner, C. H. Terrell, J. R. Sherbotie, J. W. Foreman, C. Przysiecki, E. G. Neilson, and J. R. Hoyer, "Inhibition of Calcium-Oxalate Crystal-Growth In vitro by Uropontin - Another Member of the Aspartic Acid-Rich Protein Superfamily," *Proc Natl Acad Sci U S A* **89** (1), 426-430 (1992).
- 2 S. R. Qiu, A. Wierzbicki, C. A. Orme, A. M. Cody, J. R. Hoyer, G. H. Nancollas, S. Zepeda, and J. J. De Yoreo, "Molecular modulation of calcium oxalate crystallization by osteopontin and citrate," *Proc Natl Acad Sci U S A* **101** (7), 1811-1815 (2004).
- 3 A. Taller, B. Grohe, K. A. Rogers, H. A. Goldberg, and G. K. Hunter, "Specific adsorption of osteopontin and synthetic polypeptides to calcium oxalate monohydrate crystals," *Biophys J* **93** (5), 1768-1777 (2007).
- 4 J. R. Hoyer, J. R. Asplin, and L. Otvos, "Phosphorylated osteopontin peptides suppress crystallization by inhibiting the growth of calcium oxalate crystals," *Kidney International* **60** (1), 77-82 (2001).
- 5 J. Sodek, B. Ganss, and M. D. McKee, "Osteopontin," *Crit. Rev. Oral Biol. Med.* **11** (3), 279-303 (2000).

- 6 L. J. Wang, X. Y. Guan, R. K. Tang, J. R. Hoyer, A. Wierzbicki, J. J. De Yoreo, and G. H. Nancollas, "Phosphorylation of osteopontin is required for inhibition of calcium oxalate crystallization," *J. Phys. Chem. B* **112** (30), 9151-9157 (2008).
- 7 G. K. Hunter, C. L. Kyle, and H. A. Goldberg, "Modulation Of Crystal-Formation By Bone Phosphoproteins - Structural Specificity Of The Osteopontin-Mediated Inhibition Of Hydroxyapatite Formation," *Biochem. J.* **300**, 723-728 (1994).
- 8 J. A. Wesson, E. M. Worcester, and J. G. Kleinman, "Role of anionic proteins in kidney stone formation: Interaction between model anionic polypeptides and calcium oxalate crystals," *J Urology* **163** (4), 1343-1348 (2000).
- 9 B. Grohe, J. O'Young, D. A. Ionescu, G. Lajoie, K. A. Rogers, M. Karttunen, H. A. Goldberg, and G. K. Hunter, "Control of calcium oxalate crystal growth by face-specific adsorption of an osteopontin phosphopeptide," *J. Am. Chem. Soc.* **129** (48), 14946-14951 (2007).
- 10 J. O'Young, S. Chirico, N. Al Tarhuni, B. Grohe, M. Karttunen, H. A. Goldberg, and G. K. Hunter, "Phosphorylation of Osteopontin Peptides Mediates Adsorption to and Incorporation into Calcium Oxalate Crystals," *Cells Tissues Organs* **189** (1-4), 51-55 (2009).
- 11 T. Jung, X. X. Sheng, C. K. Choi, W. S. Kim, J. A. Wesson, and M. D. Ward, "Probing crystallization of calcium oxalate monohydrate and the role of macromolecule additives with in situ atomic force microscopy," *Langmuir* **20** (20), 8587-8596 (2004).
- 12 S. W. Guo, M. D. Ward, and J. A. Wesson, "Direct visualization of calcium oxalate monohydrate crystallization and dissolution with atomic force microscopy and the role of polymeric additives," *Langmuir* **18** (11), 4284-4291 (2002).
- 13 A. Millan, "Crystal growth shape of whewellite polymorphs: Influence of structure distortions on crystal shape," *Crystal Growth & Design* **1** (3), 245-254 (2001).
- 14 S. Hug, B. Grohe, J. Jalkanen, B. Chan, B. Galarreta, K. Vincent, F. Lagugne-Labarthe, G. Lajoie, H. A. Goldberg, M. Karttunen, and G. K. Hunter, "Mechanism of inhibition of calcium oxalate crystal growth by an osteopontin phosphopeptide," *Soft Matter* **8** (4), 1226-1233 (2012).
- 15 P. V. Azzopardi, J. O'Young, G. Lajoie, M. Karttunen, H. A. Goldberg, and G. K. Hunter, "Roles of Electrostatics and Conformation in Protein-Crystal Interactions," *PLoS One* **5** (2), 11 (2010).

- 16 Jason O'Young, *Molecular dynamics and FRAP analysis of protein-crystal interactions*, (Schulich School of Medicine & Dentistry, The University of Western Ontario, 2008).

Chaper 6: Conclusion

In my first project I studied solid-solid phase transitions in normal alkanes. The normal alkanes often exhibit complicated phase behavior, with phase diagrams containing multiple solid phases. This work shows the study of a curious pattern of twinned domains seen in one phase of tricosane ($C_{23}H_{48}$): the rotator R_V phase, a monoclinic arrangement of tricosane molecules without orientational order. We studied solid-solid phase transitions involving this phase using X-ray diffraction, as well as by optical and atomic-force microscopy. Transitions between this polymorph and the orthorhombic R_I rotator phase lying at higher temperatures preserve features at the molecular level, and thus represent a diffusionless, martensitic-like transformation, similar to those seen in certain metal alloys. Since the transition occurs at convenient temperatures, and because the tricosane molecules are large relative to metal atoms, the transitions are slow enough to be easily studied. Optical and atomic-force microscopy imaging reveals that the R_V structure is highly twinned, exhibiting a prominent arrangement of ridges arranged in domains bounded by two types of twin planes. Using the information from X-ray diffraction and optical microscopy, the structure of the monoclinic rotator phase was determined. This work has shown that the transition from the R_V phase to and from the R_I phase preserves both the macroscopic domain structure on length scales of 10s of μm , and microscopic molecular features on nm scales, made possible by the very similar densities of the two phases. We also presented a simple mechanical model to explain the length scale of the twinned domains in terms of a competition between mechanical stress and the interfacial energy of the domain boundaries

I performed an initial investigation of this twinning effect in pentacosane ($C_{25}H_{52}$) and found similar results. Future studies might continue this work, or explore the combined C_{23}/C_{25} system.

In my second project, I investigated the effect of certain proteins on the crystallization of calcium oxalate monohydrate (COM), the primary constituent of most kidney stones. Certain proteins, such as osteopontin (OPN), inhibit stone formation, but the molecular-scale details by which they act is poorly known. The inhibition of crystallization due to adsorbed impurities is usually explained in terms of a model proposed in 1958 by Cabrera and Vermilyea. In this model, impurities adsorb to growth faces and pin growth steps, forcing them to curve, thus impeding their progress via the Gibbs-Thomson effect. In order to determine the role of OPN in the biomineralization of kidney stones, crystal growth on the $\{010\}$ face of COM was examined in real time with atomic force microscopy in the presence of a

synthetic peptide referred to as pOPAR, corresponding to amino acids 65–80 of rat bone OPN. We observed clear changes in the morphology of the growth-step structure and a decrease in step velocity upon addition of pOPAR, which suggests adsorption of this molecule on the {010} growth hillocks. Experiments in which pOPAR was flushed from the growth cell by a supersaturated calcium oxalate solution showed that COM hillocks are able to fully recover to their pre-inhibited state. Our results suggest that recovery occurs through incorporation of the peptide into the growing crystal, rather than by desorption from the growth face, as assumed by other researchers. This work provides new insights into the mechanism by which crystal growth is inhibited by adsorbants, with important implications for the design of therapeutic agents for kidney stone disease and other forms of pathological calcification.

Unlike the {010} faces, growth features were not typically observed on {100} surfaces. To study the effect of the polypeptides on the {100} faces, we partially dissolved these faces in pure water to form elongated etch pits. Regrowth of these pits was observed in real time by atomic-force microscopy in the presence of saturated calcium oxalate solution. The effects on the re-growth rate of peptides of OPN (P0, P3 and pOPAR) and poly(aspartate acid) were tested. The 16 residue length pOPAR molecule shows the maximum effect on the etch-pit re-growth rate among the selection of additives we studied. Along with being a phosphorylated peptide, it is an aspartic acid rich section of the OPN, which is consistent with its higher adsorption to growth surfaces, consequently reducing the etch-pit filling rate.

Studies of calcium oxalate crystallization are continuing in our laboratory. Effects of these protein additives on the {100} surface are being extensively studied using atomic force microscopy.

Meanwhile, additional experiments to validate the hypothesis of protein incorporation into the growing crystal are being performed. Using different techniques of crystal growth it is possible to grow crystals in which {121} and {021} surfaces are accessible to the AFM, thus allowing one to examine the growth process on these faces in the presence of inhibitors.

Appendix A: Twinning pattern in C_{25}

We have also performed preliminary optical imaging of C_{25} crystals and observe a twinned pattern similar to that seen for C_{23} . Fig. A.1 show the occurrence of the pattern formed between 47°C to 49°C during slow heating of the C_{25} . The pattern is very similar to the one observed in C_{23} , but not as distinct.

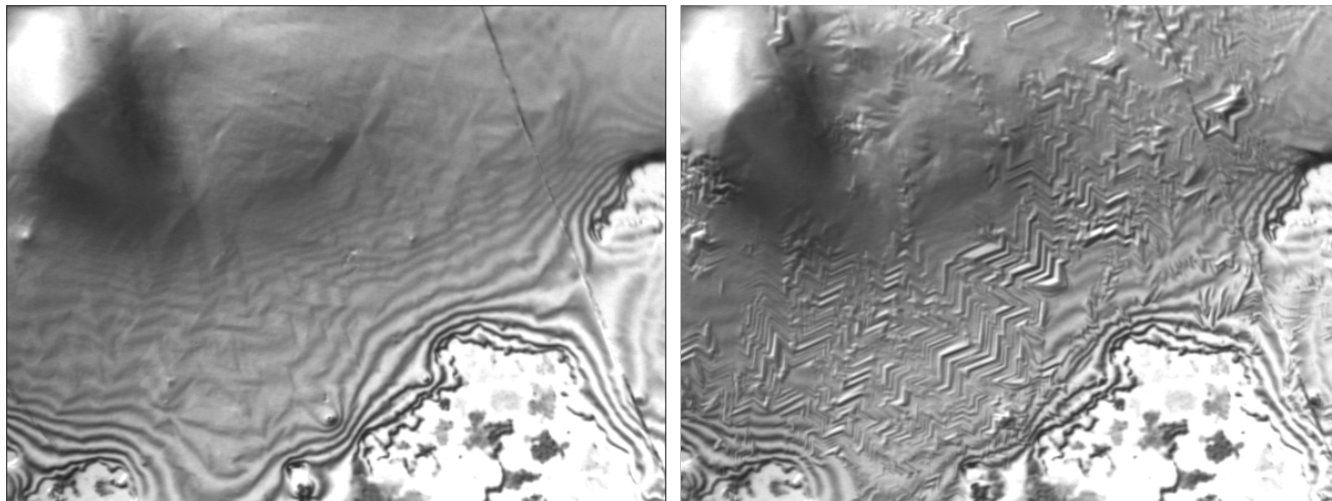


Figure A.1 Optical microscopy images showing the twinning pattern observed in n-pentacosane.

Appendix B: Detailed calculations for the conceptual model for crystal twinning

We observed the entire sample, aside from occasional small regions, twinned in a single thermodynamically stable monoclinic phase. Consider the Fig. B.1 showing a cross-section of a twinned region perpendicular to the ridges, with twin axes (dotted lines) and crystal surfaces (solid lines) identified for a single domain (shaded region).

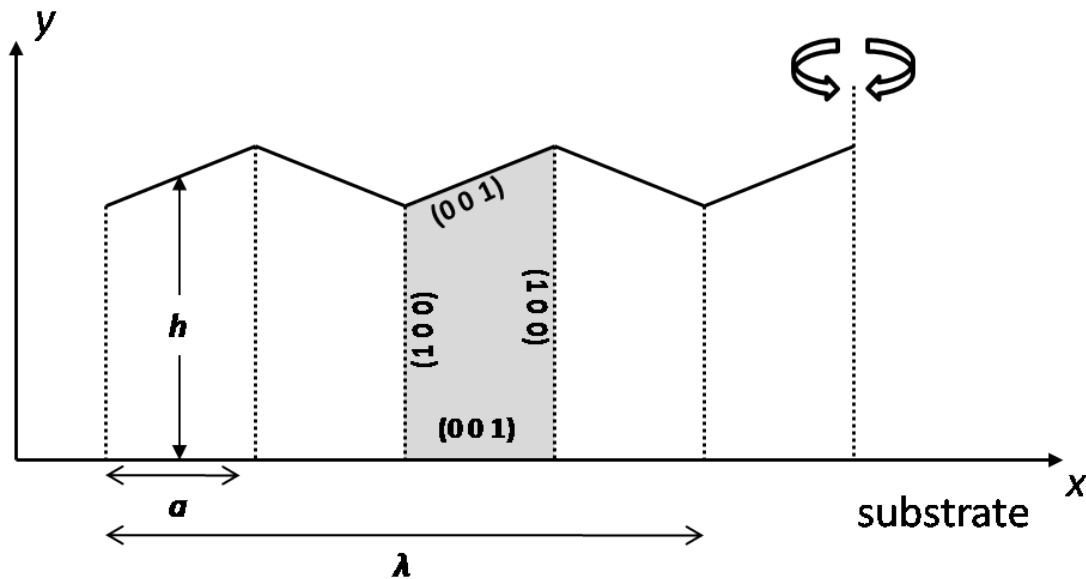


Figure B.1 Illustration showing a cross-section of a twinned region perpendicular to the ridges, with twin axes (dotted lines) and crystal surfaces (solid lines) identified for a single domain (shaded region).

There are two energies of primary importance: the strain energy and twin plane energy. For the strain energy, consider Fig. B.2 (a) for the formation of a single trapezoidal domain.

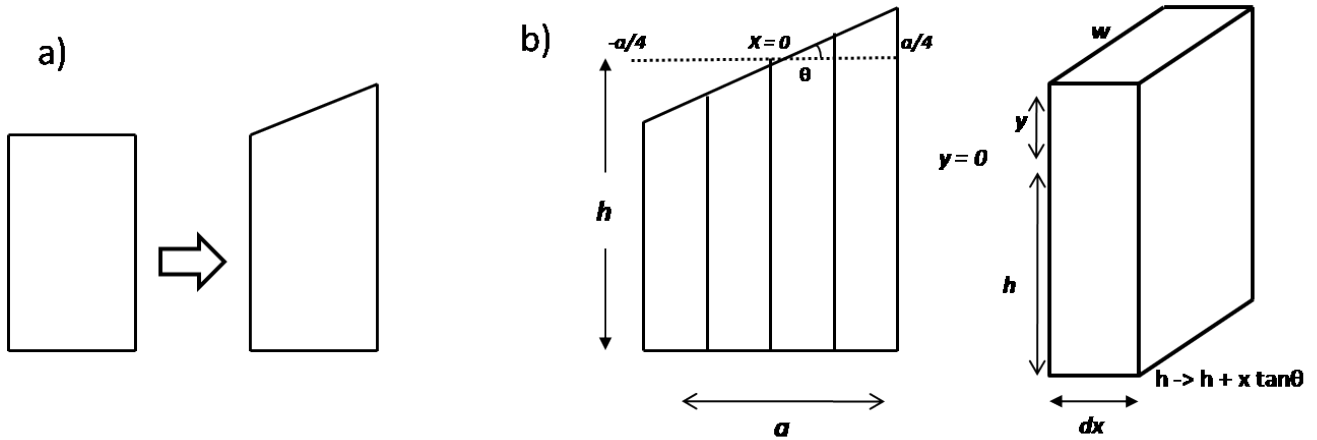


Figure B.2 Illustration showing formation of the single domain of twinned region in C23.

As shown in Fig. B.2 (b), consider each trapezoidal as divided into small slabs, each with vertical length h and thickness dx .

The Young's modulus of a material can be used to calculate the force F it exerts under a specific strain. From the definition of young's modulus, we can write for our case,

$$E = \frac{F/A}{\Delta L/L_0} = \frac{F/wdx}{y/h}, \quad (1)$$

so that

$$F = wdxE \frac{y}{h}, \quad (2)$$

where E is the modulus of elasticity, $A = w dx$ is the original cross-sectional area through which the force is applied with w length of the ridge, $\Delta L = y$ is the amount by which the length of the object changes and $L_0 = h$ is the original length of the object.

So from Fig. B.2 (b), the work W of stretching the slab of thickness dx , is

$$dW = wdx \frac{E}{h} \int_0^{x \tan \theta} y dy = wdx \frac{E}{h} \frac{x^2 \tan^2 \theta}{2}, \quad (3)$$

where, $\theta \sim 90 - \beta$ is the inclination of the ridge. So the total mechanical energy of a single trapezoidal region will be

$$E_{strain} = W = \int_{-a/4}^{a/4} w dx \frac{E}{h} \frac{x^2 \tan^2 \theta}{2} = \frac{1}{192} \frac{w E}{h} \tan^2 \theta a^3. \quad (4)$$

Here, each trapezoid corresponds to half of a ridge, and that strain energy is minimized if the center of a trapezoid is unstrained, with the maximum strain of $l \tan \theta / 4h$ at either end. As a result, the total elastic energy for the region of extent a along the x -axis as well as w along the z -axis, which contains $2l/a$ trapezoidal domains will be

$$E_{strain} = \frac{1}{192} \frac{w E}{h} \tan^2 \theta a^3 \frac{2l}{a} = \frac{1}{96} \frac{w E}{h} \tan^2 \theta a^2 l. \quad (5)$$

Now, if each twin boundary has the interfacial energy of γ per area, the energy per unit length along z -axis of $2l/a$ boundaries has a twin-plane energy of,

$$E_{twin} = 2w h \gamma \frac{l}{a}. \quad (6)$$

Thus total energy will be

$$E = E_{strain} + E_{twin} = \frac{1}{96} \frac{w E}{h} \tan^2 \theta a^2 l + 2w h \gamma \frac{l}{a}. \quad (7)$$

Energy minimization then suggests

$$\frac{dE}{da} = \frac{1}{96} \frac{w E}{h} \tan^2 \theta 2 a l - 2w h \gamma \frac{l}{a^2} = 0 \quad (8)$$

for equilibrium. Thus,

$$a^3 = \frac{96 h^2 \gamma}{E \tan^2 \theta}. \quad (9)$$

The typical values of the wax crystals in our case are $h \approx 20 \mu\text{m}$ and $a = 1 \mu\text{m}$, which allow us to predict $\gamma/E \approx 4 \times 10^{-13}\text{m}$.

*Curriculum Vitae***Shailesh Nene****POST-SECONDARY EDUCATION**

Ph.D. Candidate (Physics) <i>Western University, Canada</i>	2005–present
M.Sc. (Physics) <i>Kent State University, USA</i>	December 2004
M.Sc. (Electronics) <i>Mumbai University, India</i>	May 1999
B.Sc. (Physics & Mathematics) <i>Mumbai University, India</i>	May 1997
Diploma in Software Engineering <i>Aptech Computer Education, India</i>	August 1995

PUBLICATIONS

- **Shailesh S. Nene**, Graeme K. Hunter, Harvey A. Goldberg, and Jeffrey L. Hutter, "Regrowth of calcium oxalate etch-pita on {100} faces", (in preparation).
- **Shailesh S. Nene**, Graeme K. Hunter, Harvey A. Goldberg, and Jeffrey L. Hutter, "Reversible Inhibition of Calcium Oxalate Monohydrate Growth by an Osteopontin Phosphopeptide," *Langmuir* **29** (21), 6287–6295 (2013).
- **S. Nene**, E. Karhu, R. L. Flemming, and J. L. Hutter, "A diffusionless transition in a normal alkane," *Journal of Crystal Growth* **311** (23–24), 4770–4777 (2009).
- B. Ellman, **S. Nene**, R. J. Twieg, and A Semyonov, "High Mobility, Low Dispersion Hole Transport in 1,4-Diiodobenzene," *Adv. Mater.* **18**, 2284–2288 (2006).
- **S. Nene**, *Purification, Growth and Characterization of Organic semiconductors*. Master's thesis, Kent State University, USA (2004).
- R. J. Twieg, B. Ellman, **S. Nene**, Y. Getmanenko, Z. Lu, A. Semyonov, S. Huang, P. He, A. Seed, A. Kiryanov, "Single Crystal, Liquid Crystal and Hybrid Organic Semiconductors," *Proceedings of SPIE*, **4991**, 212 (2002).

RELATED WORK EXPERIENCE

Laboratory Supervisor, First Year Physics Laboratory <i>Western University, London, ON Canada</i>	2010–present
Geophysical Field Data Processor <i>Aeroquest Limited, Mississauga, ON Canada</i>	2008–2009
Research and Teaching Assistant <i>University of Western Ontario, London, ON Canada</i>	2005–2010
Research and Teaching Assistant <i>Kent State University, Kent, OH USA</i>	2001–2004
Corporate trainer (IT) <i>Pragati Software Pvt. Ltd., Mumbai, India (http://www.pragatisoftware.com/)</i>	1998–2000

CONFERENCE PRESENTATIONS

Real-time atomic force microscopy study of the inhibition of calcium oxalate crystallization
Himasha Wijesekara, **Shailesh Nene**, Rafael Schulman, Graeme Hunter, Harvey Goldberg
and Jeff Hutter, Center for Advanced Materials and Biomaterial Research (2012, Poster,
presented by Himasha Wijesekara)

Examining the role of Osteopontin on Calcium Oxalate Crystallization using Atomic Force
Microscopy. **Shailesh Nene**, Graeme Hunter and Jeffrey Hutter. The Canadian Association of
Physicists Congress (2011, talk, presented by Jeffrey Hutter).

Atomic Force Microscopy Study of Inhibition of Calcium Oxalate Crystallization. **Shailesh
Nene**, Bernd Grohe, Harvey Goldberg, Graeme Hunter, Jeffrey Hutter. The Canadian
Association of Physicists Congress (2010, talk, presented by Shailesh Nene).

A martensitic-like transition in a normal alkane. Jeffrey Hutter, **Shailesh Nene**, Eric
Karhu, Roberta Flemming. American Physical Society meeting (2009, talk, presented by
Jeffrey Hutter)

AWARDS AND SCHOLARSHIP

- Western Graduate Thesis Research Award, 2007
- Tuition Scholarship at Mumbai University, India for M.Sc. Program 1998, 1999